# Multi-component injection moulding

*DOI:*
[10.6100/IR435035](10.6100/IR435035)

*Document status and date:*
Published: 01/01/1995

*Document Version:*
Publisher's PDF, also known as Version of Record (includes final page, issue and volume numbers)

*Please check the document version of this publication:*

• A submitted manuscript is the version of the article upon submission and before peer-review. There can be important differences between the submitted version and the official published version of record. People interested in the research are advised to contact the author for the final version of the publication, or visit the DOI to the publisher's website.
• The final author version and the galley proof are versions of the publication after peer review.
• The final published version features the final layout of the paper including the volume, issue and page numbers.
[Link to publication](Link to publication)

Download date: 04. Oct. 2023

# Multi-Component Injection Moulding

**Wim Zoetelief**

# Multi-component Injection Moulding

# Multi-component Injection Moulding

PROEFSCHRIFT

ter verkrijging van de graad van doctor
aan de Technische Universiteit Eindhoven,
op gezag van de Rector Magnificus, prof.dr. J.H. van Lint,
voor een commissie aangewezen door het College van Dekanen
in het openbaar te verdedigen op
vrijdag 7 april 1995 om 14.00 uur

door

WILHELMUS FREDERIKUS ZOETELIEF

geboren te Baarn

Dit proefschrift is goedgekeurd door de promotoren:

**prof.dr.ir.  H.E.H.  Meijer**
**prof.dr.ir.  F.P.T.  Baaijens**

en de copromotor:

**dr.ir.  G.W.M.  Peters**

*Voor Margaret*

# Contents

# Summary

In multi-component injection moulding , two or three polymer materials are sequentially or simultaneously injected into a mould to make products that contain e.g. a layered structure. The distribution of the materials in the product depends on the position of the gate, the geometry of the injection nozzle and the method of injection (simultaneous and/or sequential). Applications of this technology can be found in: shielding against electro-magnetic interference, barrier products, recycling of thermoplastic materials, and in-mould painting of products but even ball-joints could principally be realised inside a product when immiscible materials are co-injected.

The advantage of the injection moulding process with its versatility in geometrical design of the products can be extended to include the ability of combining different materials with their specific properties in one product. In order to reach that target, some limitations of the existing technology should be overcome. First, the number of different materials has to be extended from two to three to be able of combining polar and apolar polymers in one product with the third component typically acting as a compatibilizer. Second, the geometrical design of a product should not be limited by the process. These facts ask for a technique which is capable of predicting the material distribution in a product. In this thesis numerical tools are developed for calculating the positions of material particles during the flow in the mould cavity. With these tools it is possible to solve the inverse problem of predicting the injection sequence in multi-component moulding given a required material distribution in a product.

Starting with the balance equations for mass, momentum, moment of momentum, and energy the fundamental equations are derived. Further simplification is established by assuming that the mould cavities consist of narrow, weakly curved channels which results in the thin-film approximation or $2\frac{1}{2}$D approach. In order to complete the set of equations constitutive relations are chosen. The material behaviour of the molten polymer is considered to follow a generalized Newtonian law and the density as a function of the pressure and temperature is modelled by the Tait equaiton. A particle

tracking method based on the conservation of identity of material particles is added for use in multi-component moulding. The unique particle identity is defined by its entrance position and injection time which is preserved during the flow in the cavity. Special attention is focussed to satisfying the local mass balance at the melt front and at flow splittings.

The modelling is tested by comparing numerical and experimental results for two well defined flow problems: the flow between two pistons advancing in a tube with and without a contraction. Using differently coloured slices of the same or of dissimilar materials combined in one sample, the deformation patterns are visualized. The deformation patterns thus obtained proved to be sensitive to all aspects that influence the flow kinematics. Differences in the fluid behaviour between polystyrene (PS) and acrylontrile-butadiene-styrene (ABS) could be observed easily. The flow through the contraction is modelled using a fixed domain approach. The pistons are modelled with an artificial high viscosity material that slips at the wall. This special case of multi-component flow gives a good approximation of the flow in a time dependent domain.

Several applications of multi-component injection moulding are demonstrated. The colour distribution in a co-injected strip with stiffener ribs is calculated and is validated with experiments. The colour patterns in the midplane and the break-through of the second material through the first showed that all aspects present in the experimental results could be revealed in the numerical simulations. The effect of the presence of a bifurcation of the midsurface, as occuring in flow splittings, is investigated numerically. Finally, two examples are given of the inverse mapping technique. In the first, a relatively complex product is considered for use in multi-colour moulding whereas the application of an iterative technique is demonstrated for the filling of a simple rectangular mould with different materials.

The conclusion can be drawn that the assistance of computer simulations is indispensable to attain the required material distribution in the product. Moreover, it turned out that modelling of multi-component flows, in test problems as well as in injection moulding, proved to be rather complete and thus predictions can be made succesfully regarding all those aspects that can be considered important in practice.

# Notation

## Quantities

| | |
|---|---|
| $A$, $a$ | scalar |
| $\vec{a}$ | vector |
| $\mathbf{A}$ | second order tensor |
| $\underset{\sim}{A}$, $\underset{\sim}{a}$ | column |
| $\underline{A}$ | matrix |
| $\mathbf{I}$ | second order unit tensor |

## Operations and functions

| | |
|---|---|
| $\mathbf{A}^c$ | conjugation |
| $\vec{a} \cdot \vec{b}$, $\mathbf{A} \cdot \mathbf{B}$ | inner product |
| $\mathbf{A} : \mathbf{B}$ | double inner product |
| $\mathbf{A}^{-1}$, $\underline{A}^{-1}$ | inversion |
| $\|\vec{a}\|$, $\|\mathbf{A}\|$ | norm |
| $tr(\mathbf{A})$ | first invariant of a second order tensor, or trace |
| $\mathbf{A}^d = \mathbf{A} - \frac{1}{3} tr(\mathbf{A})\,\mathbf{I}$ | deviatoric part of a second order tensor |
| $\underset{\sim}{a}^T$, $\underline{A}^T$ | transposition |
| $\vec{\nabla}$ | gradient operator |
| $\dot{a}$ | material time derivative |
| $\frac{\partial a}{\partial t}$ | spatial time derivative |

# Chapter 1

# Introduction

## 1.1 The multi-component injection moulding process

In almost all technical products that we know of, parts made of polymers can be found. The main reason for this interesting findings is that polymer materials are easy to process and, moreover, possess a number of advantageous properties compared to other often used materials such as steel and aluminium. Amongst the possible processing techniques for polymer materials, *injection moulding* is one of the most commonly applied. This technique can be used when mass-manufacturing of complexly shaped, highly integrated products is required. Different applications and classes of polymers have led to the development of different injection moulding techniques. Some rather specific examples are:

- gas assisted injection moulding

- foam injection moulding

- thermoset injection moulding

- (structural) reaction injection moulding

- (resin) transfer moulding

- two-shot injection moulding

- multi-component (or sandwich or co-) injection moulding

For the sake of clearness, injection moulding will be explained briefly. Figure 1.1 shows a schematic representation of an injection moulding machine. It mainly consists of two parts: an injection and a clamping unit. The

injection unit contains a screw rotating in a heated barrel plasticizing the granulated polymer feed stock conveyed from the hopper. When sufficient material has been plasticized, the screw acts as a piston and pushes the melt through a nozzle and runner system into the mould cavity. Backflow into the screw channel is generally prevented by a non-return valve. The clamping unit supports the two mould halves and prevents the mould from opening despite of the high pressure that occurs during the process.

An injection moulding cycle can roughly be divided into three different stages: the injection, the packing and holding, and the cooling stage. In the injection stage the molten polymer is injected in the mould. After complete filling of the cavity, extra material will be added to compensate for shrinkage, the so-called packing and holding stage. From the moment the gate is completely frozen, no more material can be injected and the cooling stage starts. When the temperature is dropped below the ejection temperature, the mould is opened and the product can be taken out for further cooling to the ambient temperature.
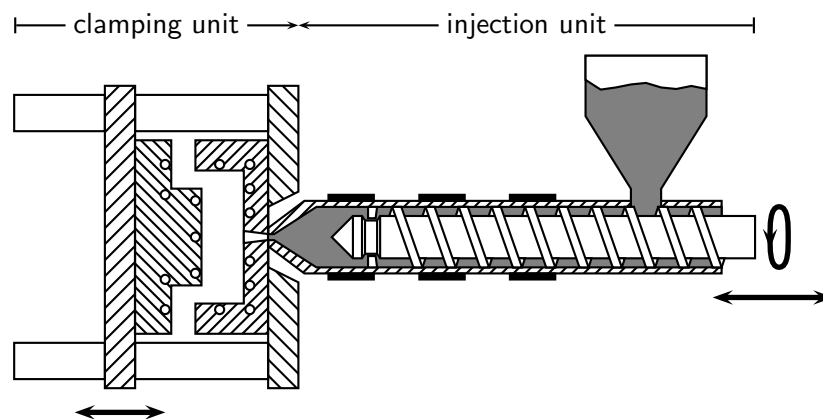


Figure 1.1: Injection moulding machine

In the multi-component injection moulding process, two or three polymer materials are sequentially or simultaneously injected in the mould to make products with e.g. a layered structure. The distribution of the layers in the product depends on the position of the gate, geometry of the injection nozzle and the method of injection (simultaneous and/or sequential). By changing the sequence of injection of two components A and B (A,B; A,B,A; A/B; A,A/B,A; etc.) the thickness and also the place (centric or eccentric) of the layers can be controlled (see figure 1.2). The multi-component injec-
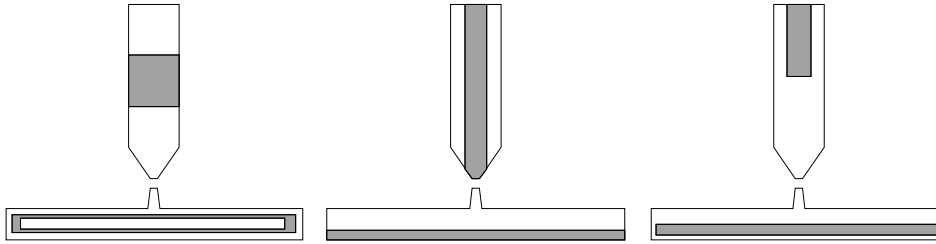
Figure 1.2: Schematic representation of two component injection moulding with sequential (A,B,A), simultaneous (A/B), and combined (A,A/B) injection

tion technology differs from the multi-shot technology, where after complete solidification the first shot is placed into a larger mould-cavity followed by the injection of a second shot against or around the previous shot.

## 1.2    Literature overview

The literature that reflects the current state of research concerning the subject of this thesis covers the following four topics: a history of multi-component injection moulding, modelling aspects, particle tracking options and fountain flow phenomena. From these, particle tracking plays a major role in the modelling of the multi-component injection moulding process, since it is required to know were the material particles end-up in a product even if it possesses a complex shape. A major influence on the final particle distribution throughout the product, especially in the outside layers, is governed by the so-called fountain flow. As a result, material injected later in the injection period may even break-through previously injected material.

### 1.2.1    Multi-component injection moulding

The multi-component injection technique was developed by ICI in 1967 (Garner and Oxley, 1969). The process aimed at the production of large, lightweight, and stiff products. The sequential injection of two components (A,B; A,B,A) limited the practical applications to simply shaped sandwich constructions with three layers. The component B, the core layer, typically consisted of the A material with a physical or chemical foaming agent. In this way, large parts with hard, flat, and glossy skin layers could be moulded without the need for high clamping forces since shrinkage was compensated for by the expansion of the core material (instead of by packing at high pressures as in the conventional injection moulding process). Applications of the

thick-walled (> 4 mm) products could be found in the automotive, housing, and sanitary branches. In applications where thin-walled products are more suitable, light-weight, high-stiffness products could be moulded more economically using reinforcing ribs.

Initiated at the DSM Central Laboratory (Verheijen *et al.*, 1983), during the last decade, the multi-component injection moulding technology has also been evaluated for thin-walled products using the Battenfeld two-channel technique (figure 1.3 (after Eckardt, 1987)). With this technique not only
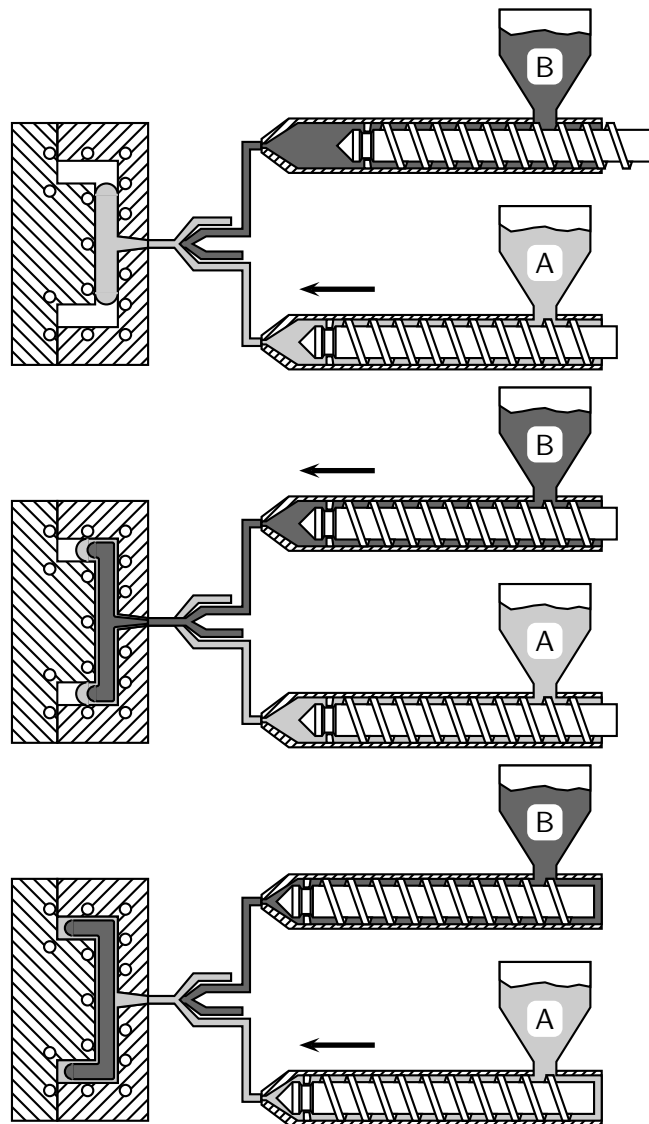
Figure 1.3: Principal of mould filling (A,B,A) with the Battenfeld system

sequential injection is possible as in the ICI technique, but also simultaneous injection of two components (A,A/B,A; A,B/A,A). In this way, thin, eccentric layers could be realized in a product.

Some examples of applications are:

- Shielding against electro-magnetic interference (EMI) of e.g. computer housings, where a Faraday-cage is created by a conductive layer inside the product (Eckardt, 1985, 1987).

- Barrier products, where a thin layer of a material with a low permeability for gases is enclosed by outer layers that provide properties like stiffness and visual appearance combined with water resistency (Eckardt, 1987; Tung and Kudert, 1990).

- Recycling of thermoplastic materials. The scrap material ends up in the core of a product surrounded by virgin plastic (for this application the original literature goes back to Donovan *et al.*, 1975).

- In-mould painting of the products. With the sandwich moulding process a thin layer of paint will cover the surface. No finishing of the product is needed.

- A thin (eccentric) layer of special polymer can be put just below the surface to provide for e.g. laser-writability.

Besides the development of the multi-component technology, structure development during moulding has been studied in order to gain more insight in the moulding process itself. White and Lee (1975) and Young *et al.* (1980) performed several tests with different material combinations and injection configurations. In the case of isothermal conditions, they found that the most uniform skin-core structures occurred when the melt injected first possessed a lower viscosity than the second melt. Moreover, in case of simultaneous injection of two materials, the melt with the lower viscosity did encapsulate the melt with the higher viscosity during the flow in the runner section (macroscopic phase inversion).

## 1.2.2   Modelling aspects

The last two decades have shown many contributions to the development of the numerical simulation of the injection moulding process. In the seventies the analysis of the filling stage, and thus the prediction of filling patterns, weld-lines and vent gates and of the pressure- and temperature distributions, was the main goal. Only simple geometries, of circular or rectangular shape,

could be analyzed. The flow was mainly uni-directional with a temperature field that was typically two-dimensional (one coordinate in the flow direction and the other in the thickness direction of the product) leading to the so-called $1\frac{1}{2}$D approach. In the simulations, generalized Newtonian fluid behaviour was assumed. Papers of Harry and Parrot (1970); Wu *et al.* (1974); Williams and Lord (1975); Lord and Williams (1975) are worth to be mentioned.

During the eighties, the simulations were extended to include more complex geometries. Richardson *et al.* (1980) combined basic $1\frac{1}{2}$D flow geometries, such as rectangular channels, circular pipes and discs, in parallel and series to form arbitrarily shaped cavities. The basic, useful and generally applicable approach that is used in all more serious programs that are still in development at present, was originally developed by Hieber and Shen (1980;1983). They combined the finite element method for solving the pressure field in two dimensions with the finite difference method for solving the temperature and velocity field in three dimensions. This so-called $2\frac{1}{2}$D approach was later improved and/or extended by many others (see e.g. Sitters, 1988; Boshouwers and van der Werf, 1988; Douven, 1991; Chiang *et al.*, 1991a).

In the same period, the $1\frac{1}{2}$D approach was extended to include the packing and holding stages of the process. Kamal and Lafleur (1982); Kamal *et al.* (1986); Lafleur and Kamal (1986) modelled the entire injection moulding cycle introducing viscoelastic material behaviour.

Today, the tendency is directed towards prediction of the final properties of injection moulding products rather than solely analyzing the mouldability of a product. Nearly all (commercial) codes use the $2\frac{1}{2}$D approach for all stages of the process combined with generalized Newtonian fluid behaviour during filling (Boshouwers and van der Werf, 1988; Dupret and Vanderschuren, 1988; Chiang *et al.*, 1991a,b) and/or differential (Leonov) models or integral Wagner models to account for the visco-elastic stresses in a direct (Baaijens, 1991; Papathanasiou and Kamal, 1993; Kamal and Papathanasiou, 1993) or indirect, decoupled (Douven, 1991) approach. The product properties that can be predicted are:

- flow-induced stresses (Isayev and Hieber, 1980; Flaman, 1990; Baaijens, 1991; Douven, 1991)

- thermally and pressure induced stresses (Titomanlio *et al.*, 1987; Douven, 1991; Baaijens, 1991)

- density distributions (Greener, 1986a,b; Caspers, 1995)

- dimensions and shape of products (St. Jacques, 1982; Isayev and Hariharan, 1985; Douven, 1991; Caspers, 1995)

In literature not much attention is paid to the modelling of the multi-component injection moulding process. Turng *et al.* (1993) modelled the sequential injection of two (different) polymers by calculating the residence time of particles that enter the mould cavity. By doing so, they were able to predict the position of the interface between the two materials. However, their method is restricted to sequential injection of two materials with one switch-over time only. In Peters *et al.* (1994) examples are given of both sequential and simultaneous injection. Their method, which uses a conservation of identity, can be extended to model all types of multi-component injection moulding.

### 1.2.3   Particle tracking

For obvious reasons, in the particle tracking technique adopted in this thesis, no real particles are present that exert hydrodynamic interaction to each other as is the case in the flow or the motion of particles in e.g. slurry flows. The 'particles' are abstract distinct points in the flow that have to be followed in time and space. Using similar definitions, particle tracking recently got considerable attention in numerical simulations of non-Newtonian flows employing memory integral equations (see e.g. Crochet *et al.*, 1984; Luo and Tanner, 1986; Luo and Mitsoulis, 1990). Since integral models take into account a part of the deformation history to calculate the Cauchy-Green and Finger strain tensors, it is essential to find the particle position as a function of the (residence) time. In two-dimensional steady flow situations, particle tracking was simplified by the formation of special streamline elements in which the element boundaries follow the streamlines (Luo and Tanner, 1986). However, these methods failed in recirculation regions. To solve this, Luo and Mitsoulis (1990) tracked particles individually for every nodal point in the finite element mesh. Based on the expression for particle acceleration in steady flow, they derived a step-by-step scheme with third-order accuracy, provided that the velocity gradients are exact. For the same purpose the particle paths can be constructed by integrating the reversed velocity field starting from every nodal point in the mesh (Crochet *et al.*, 1984). Caspers (1991) used this method in injection moulding simulation and solved the initial value problem with a Runga-Kutta method. However, in transient calculations, as in mould-filling, this requires storage of the complete velocity field for every time step. Thus, tremendous storage capacity is required. To get around this problem, Peters *et al.* (1994) developed a method of conservation of identity for multi-component injection moulding by defining material

particles by their unique identity (e.g. material, colour, place and time of injection). The transport of the identity during the flow can be described by a pure convection equation, which can be solved in either a Lagrangian or Eulerian way.

Particle tracking can also be used for other purposes. Matsuhiro and Shiojima (1990) determined the moving free surface by transporting marker particles in the front region. Those markers are convected numerically by integrating the velocity field denoting the newly filled elements at the front. Hannachi and Mitsoulis (1990) showed that particle tracking may provide a better understanding of flow kinematics by calculating the residence time distribution of material points through the integration of the velocity field and by plotting isochrones and the deformation field of fluid elements. These kinematic patterns provide a Lagrangian representation of the flow and describe the deformation history of fluid elements as they travel through the field. The patterns thus obtained can be compared easily with experimental results if colored tracers are used (see e.g. Vos *et al.*, 1991).

## 1.2.4  Fountain flow phenomena

In flows with one or more free boundaries and a no-slip condition at the walls, fluid elements adjacent to the moving front experience the so-called *fountain flow* (Rose, 1961). The fluid near the center moves at a higher speed than the local average speed across the channel, and when reaching the front, spreads towards the walls (figure 1.4). In experimental mould filling studies, these



velocity profile
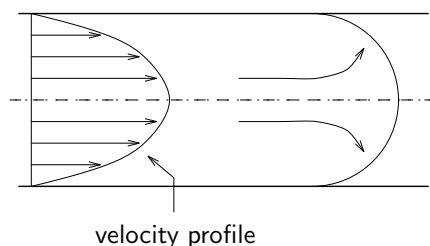
Figure 1.4: Fountain flow phenomena

specific flow patterns behind the advancing free surface were observed as well (Schmidt, 1974; Gogos *et al.*, 1986; Coyle *et al.*, 1987). The fountain flow directly affects transport characteristics such as the temperature distribution, conversion distribution and fibre orientation not only at the front but in the whole domain that is close to the walls, thus the (important) outsides of the product. Beris (1987) showed that the observed V-shape deformation of fluid elements is independent of the constitutive equation used, since it is completely determined by the balance of mass.

Studies dealing with the modelling of the fountain flow describe either an interface between two (immiscible) liquids or analyze a free front (thus one of the liquids is inviscid: air or vacuum) advancing in a capillary tube or between parallel plates. Bhattacharji and Savic (1965) made the first attempt to arrive at a semi-analytical solution of the Navier-Stokes equations for the liquid/liquid interface for Newtonian fluids in pipe flow under action of a piston. Castro and Macosko (1982) derived, analogously, the expressions for flow between two semi-infinite parallel plates. More recently, Haiqing (1993) gave an analytical expression for characterizing the fountain effect in rectangular shaped moulds with finite dimensions. In his analysis, an arbitrary dynamic slip boundary condition at the walls could be imposed, in contrast with the work of Bhattacharji and Savic. Unfortunately, no explicit expression can be found in Haiqing (1993) for this specific case.

Numerical solutions for the 2D flow between parallel plates, containing a transient free surface flow, were obtained using the Marker-and-Cell technique (Gogos *et al.*, 1986; Kamal and Lafleur, 1982; Kamal *et al.*, 1986; Lafleur and Kamal, 1986), or finite element methods (Coyle *et al.*, 1987; Mavridis *et al.*, 1986, 1988). Behrens *et al.* (1987) investigated numerically the fountain flow effect in a tube. In these studies, special attention was given to the motion of the free surface and the movement of the contact point at the wall.

Several models are proposed that can be used in combination with the $2\frac{1}{2}$D approximation in injection moulding (Manas-Zloczower *et al.*, 1987; Dupret and Vanderschuren, 1988; Sitters, 1988; Garcia *et al.*, 1991). In these models, the contact line between melt and air is a straight line that is normal to the mould walls and moves with the gapwise-averaged fluid velocity (figure 1.5). The essence of the flow kinematics in the flow region is captured by
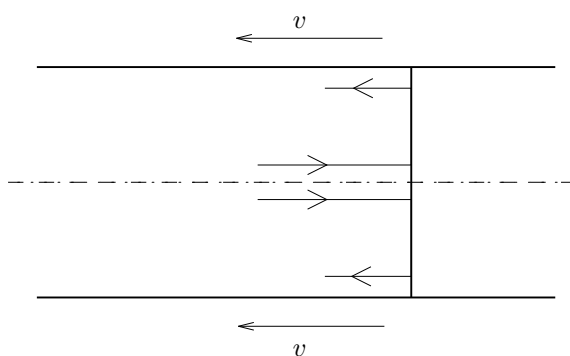


Figure 1.5: Simplified front model in injection moulding

transporting particles that enter the front domain instantly from the high-

velocity region in the core to the low-velocity regions near the walls based on a mass balance along the contact line. The point that separates the high- and low-velocity regions is travelling with the average front speed. However, this 'flat-front turnover rule' (Shen, 1992) neglects the residence time of the particles in the front domain. Peters *et al.* (1994) incorporated this residence time by parameterization of the results of particle tracking in the front domain according of the model of Bhattacharji and Savic. The residence time and the position of leaving the front are calculated only once and are fitted with a high order polynomial function. In this way, a sufficiently accurate description of the fountain effect can be established.

Recently, Friedrichs and Güçeri (1993) developed a hybrid numerical technique for capturing the flow kinematics in injection moulding for geometrical simple domains. They combined a 2D and a 3D finite element mesh to model the 3D fountain flow kinematics. The 2D-mesh covers the region behind the advancing front (Hele-Shaw approximation) and the 3D-mesh is used in the front domain. With this approach the main benefit of solving the flow kinematics in 2D gets lost and thus this approach represents a method that is only a small step away from a complete 3D analysis of the whole domain which would give a much larger improvement.

## 1.3   Research objectives

The advantage of the injection moulding process with its versatility in geometrical design of products can be extended to include the ability of combining different materials with specific properties in one product. In order to reach that target, some limitations of the existing technology should be overcome. First, the ability of injection of two components has to be extended to three components to be able of combining polar and apolar materials in one product with the third component typically acting as a compatibilizer. Second, the present limitation of the complexity of the products to relatively simple geometries has to be removed.

Given these major drawbacks of the existing technology, the research objective of this thesis can be summarized as:

> The development of numerical tools for calculating the flow path of particles. With these tools it will be possible to solve the inverted problem for predicting the injection sequences in multi-component injection moulding (figure 1.6). The results should provide all information needed for programming the control system of the injection moulding machine.

During the research project considerable effort is put on the development of a three component injection moulding technique including the machine and the control technology to remove the first limitation mentioned above. However, the set-up suffered from some problems and experimental results obtained with this machine will be expected to be accomplished in the near future.
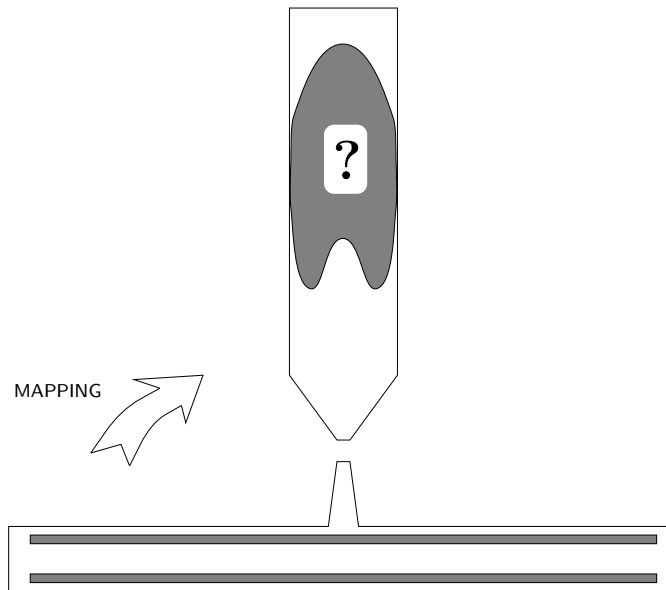


Figure 1.6: Inverse mapping

Apart from the direct practical applications, the multi-component technology can be used to produce tests on the quality of computer models developed to describe the different stages of the process. By using multi-colour injection, the experimentally obtained deformation patterns can be compared directly with numerical results. The total deformation history of every particle in the mould is important for all properties that are history dependent, such as e.g. the calculation of the local temperatures when the Péclet number is sufficiently high, or of the transient viscoelastic stresses for high Deborah numbers or the prediction of the local conversion in reactive systems for high Damköhler IV numbers.

## 1.4   Outline of the thesis

In order to make the multi-component technology more suitable for producing complex shaped products, Vos *et al.* (1991) proposed a more flexible

injection method that circumvented the relatively long opening and closing times of valves in a more traditional distribution device. Using an accumulator (see figure 1.7) in between the distribution device and the mould, any configuration requested can then be composed during the cooling stage of the previous product rather than during injection. The contents of the (heated) accumulator is subsequently injected into the mould. In this thesis, several
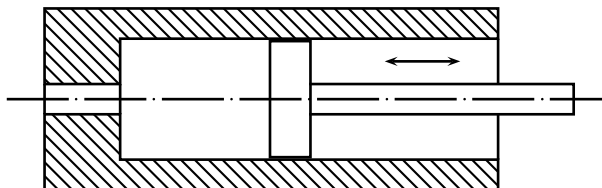


Figure 1.7: Basic design of an accumulator for the use in multi-component injection moulding

steps in the development of the multi-component injection moulding technology will be investigated separately. Starting with a piston driven flow, the flow characteristics will be studied especially in the (fountain) regions close to the pistons. Next, the piston driven flow through a contraction will be analyzed, providing the knowledge of the process of filling and emptying an accumulator. Finally, multi-component injection will be investigated using a distribution device which can be found in the existing multi-component injection moulding machines.

In Chapter 2 of this thesis, the set of equations needed to model the multi-component injection moulding process is summarized with special extensions for modelling particle tracking and the fountain flow phenomena. Chapter 3 deals with the numerical aspects, involved in solving the problems encountered. The material data necessary in the simulations are given in Chapter 4. Subsequently, Chapter 5 presents two well-defined flow problems which are used for testing of the modelling. Some examples of multi-component injection moulding are shown in Chapter 6. Finally, Chapter 7 summarizes the main results of the research and gives suggestions for future research.

# Chapter 2

# Modelling aspects

Modelling of the multi-component injection moulding process is almost identical to modelling of conventional injection moulding. Therefore, the derivation of the basic equations is not repeated in detail. The reader can be referred to existing literature (e.g. Hieber and Shen, 1980; Isayev, 1987; Dupret and Vanderschuren, 1988; Sitters, 1988; Chiang *et al.*, 1991a; Tucker III, 1991; Douven, 1991).

In Section 2.1 the main balance and constitutive equations will be summarized. Section 2.2 deals with the injection moulding process. In Section 2.3 particle tracking will be discussed followed by a treatment of the fountain flow phenomena in Section 2.4. The chapter ends with the formulation of two test problems for particle tracking.

## 2.1   Fundamental equations

The set of equations needed to describe moulding processes consists of the balance equations and the constitutive equations, completed with the proper set of boundary and initial conditions.

### 2.1.1   Balance equations

From continuum mechanics, which deals with the determination of fields of density, temperature, and motion for material points considered, the balance equations can be derived. In their local form they read :

*Balance of mass (continuity equation)*

$$\dot{\rho} + \rho \vec{\nabla} \cdot \vec{v} = 0 \tag{2.1}$$

where $\rho$ denotes the density, $\vec{v}$ the velocity vector, and $\vec{\nabla}$ the gradient operator.

*Balance of momentum*

$$\vec{\nabla} \cdot \boldsymbol{\sigma}^c + \rho\vec{f} = \rho\dot{\vec{v}} \tag{2.2}$$

with $\boldsymbol{\sigma}^c$ the Cauchy stress tensor, and $\vec{f}$ the specific body force.

*Balance of moment of momentum*

$$\boldsymbol{\sigma} = \boldsymbol{\sigma}^c \tag{2.3}$$

*Balance of energy (first law of thermodynamics)*

$$\rho\dot{e} = \boldsymbol{\sigma} : \mathbf{D} - \vec{\nabla} \cdot \vec{h} + \rho r \tag{2.4}$$

where $e$ is the specific internal energy, $\mathbf{D}$ is the rate of deformation tensor, $\vec{h}$ the heat flux vector, and $r$ is a specific heat source.

## 2.1.2    Constitutive equations

The set of balance equations can only be solved if relations are known for $\boldsymbol{\sigma}$, $\vec{h}$ and $e$ as function of density, temperature and motion. In this section the constitutive equations for the Cauchy stress tensor and the thermal properties will be given in their final form. For a more detailed description the reader is referred to (Douven, 1991, Chapter 2).

**Cauchy stress tensor**

Many different constitutive models exist that relate the Cauchy stress tensor to the independent variables $\rho$, $T$ and $\vec{x}$. Since we are basically interested in the flow kinematics, in this thesis only the generalized Newtonian fluid model will be used. This model is commonly employed in simulating the injection phase of the injection moulding process, although it neglects all the viscoelastic effects of the polymers; this proved to be not too serious (see Baaijens, 1991; Douven, 1991) since boundary and initial conditions are given as prescribed velocities and thus the kinematics dominate the flow.

**Generalized Newtonian fluid behaviour**    The Cauchy stress tensor $\boldsymbol{\sigma}$ is split into a hydrostatic part $-p\mathbf{I}$ and an extra stress tensor $\boldsymbol{\tau}$:

$$\boldsymbol{\sigma} = -p\mathbf{I} + \boldsymbol{\tau}. \tag{2.5}$$

The extra stress tensor is assumed to satisfy the generalized Newtonian fluid model:

$$\boldsymbol{\tau} = 2\eta \mathbf{D}^d, \tag{2.6a}$$

$$\eta = \eta(p, T, \dot{\gamma}), \quad \dot{\gamma} = \sqrt{2\mathbf{D}^d : \mathbf{D}^d} \tag{2.6b}$$

$$\mathbf{D}^d = \mathbf{D} - \frac{1}{3}\mathrm{tr}(\mathbf{D})\mathbf{I}, \quad \mathbf{D} = \frac{1}{2}\left(\vec{\nabla}\vec{v} + (\vec{\nabla}\vec{v})^c\right), \tag{2.6c}$$

where $\eta$ is shear viscosity, $p$ the hydrostatic pressure, $T$ the temperature, $\mathbf{I}$ the unit tensor, $\mathbf{D}^d$ the deviatoric part of the rate of deformation tensor, and $\dot{\gamma}$ the shear rate (second invariant of $\mathbf{D}^d$). Two models for the steady state shear viscosity are widely used in simulations of moulding processes (Hieber, 1987): the *Cross model*

$$\eta(p, T, \dot{\gamma}) = \frac{\eta_0}{1 + (\eta_0 \dot{\gamma}/\tau^*)^{1-n}} \tag{2.7}$$

and the *Carreau model*

$$\eta(p, T, \dot{\gamma}) = \eta_0 (1 + (\eta_0 \dot{\gamma}/\tau^*)^2)^{\frac{n-1}{2}}, \tag{2.8}$$

where $\eta_0 = \eta_0(p, T)$ is the zero shear rate viscosity, $\tau^*$ and $n$ are constants. The Cross model fits the viscosity curve well for polymers with a broad molecular weight distribution, whereas the Carreau model can be employed successfully for models with less polydispersity.

**The $p\nu T$- relation**    For amorphous polymers the double-domain Tait equation is widely used (Zoller, 1982):

$$\nu(p, T) = \begin{cases} (a_{0s} + a_{1s}(T - T_g))(1 - 0.0894 \ln(1 + \frac{p}{B_s})) & (T \leq T_g) \\ (a_{0m} + a_{1m}(T - T_g))(1 - 0.0894 \ln(1 + \frac{p}{B_m})) & (T > T_g) \end{cases} \tag{2.9a}$$

$$T_g = T_{g0} + sp, \tag{2.9b}$$

$$B_m = B_{0m}e^{-B_{1m}T}, \quad B_s = B_{0s}e^{-B_{1s}T}, \tag{2.9c}$$

where $T_g$ is the pressure dependent glass transition temperature and $a_{0m}$, $a_{1m}$, $B_{0m}$, $B_{1m}$, $a_{0s}$, $a_{1s}$, $B_{0s}$, $B_{1s}$, and $s$ are constants.

**Thermal properties**

Finally, Fourier's law for the heat flux vector is used:

$$\vec{h} = -\boldsymbol{\lambda} \cdot \vec{\nabla}T, \tag{2.10}$$

with $\boldsymbol{\lambda}$ the thermal conductivity tensor. The specific internal energy $e$ can be expressed as (Sitters, 1988),

$$\dot{e} = c_p \dot{T} + \frac{p}{\rho^2}\dot{\rho} + \frac{T}{\rho^2}\left(\frac{\partial \rho}{\partial T}\right)_p \dot{p}, \tag{2.11a}$$

$$c_p = c_p(p, T) = \left(\frac{\partial g}{\partial T}\right)_p, \tag{2.11b}$$

$$g = e + p/\rho, \tag{2.11c}$$

where $c_p$ is the thermal capacity at constant hydrostatic pressure and $g$ is the specific enthalpy. Equation (2.11a) is derived under assumption that the elasticity has a negligible contribution to the mechanical dissipation.

## 2.2   Injection moulding

The simplifications commonly applied in injection moulding will be summarized, with emphasis on the thin film approximation and the definition of the pressure and temperature problems to be solved.

### 2.2.1   Thin film approximation

In most practical applications the thickness of a injection moulded product is small (0.5–4 mm) compared to the other dimensions. Cavities thus consist of narrow, weakly curved channels. Therefore the Hele-Shaw or thin film approximation can be employed (see e.g. Hieber and Shen, 1980; Sitters, 1988; Boshouwers and van der Werf, 1988; Douven, 1991; Tucker III, 1991).

A local Cartesian vector base $O_\varepsilon : \{\vec{\varepsilon}_x, \vec{\varepsilon}_y, \vec{\varepsilon}_z\}$ can be defined in every point of the midplane of the mould. The vector $\vec{\varepsilon}_z$ is normal with respect to the midplane (figure 2.1). An arbitrary vector $\vec{a}$ can be decomposed in a vector $\vec{a}^*$ parallel to the midplane and a component in the direction of $\vec{\varepsilon}_z$

$$\vec{a} = a_i^\varepsilon \vec{\varepsilon}_i = \vec{a}^* + a_z^\varepsilon \vec{\varepsilon}_z \tag{2.12}$$

Because of the high viscosity of polymer melts, the Reynolds number (ratio between viscous and inertia forces) is small and, therefore, the inertia in the momentum equation (2.2) may be neglected. The main assumptions made in the approximations are:

- the pressure is constant in the gapwise $\vec{\varepsilon}_z$ direction.

- the velocity gradients parallel to the midplane are small compared to those in $\vec{\varepsilon}_z$ direction.
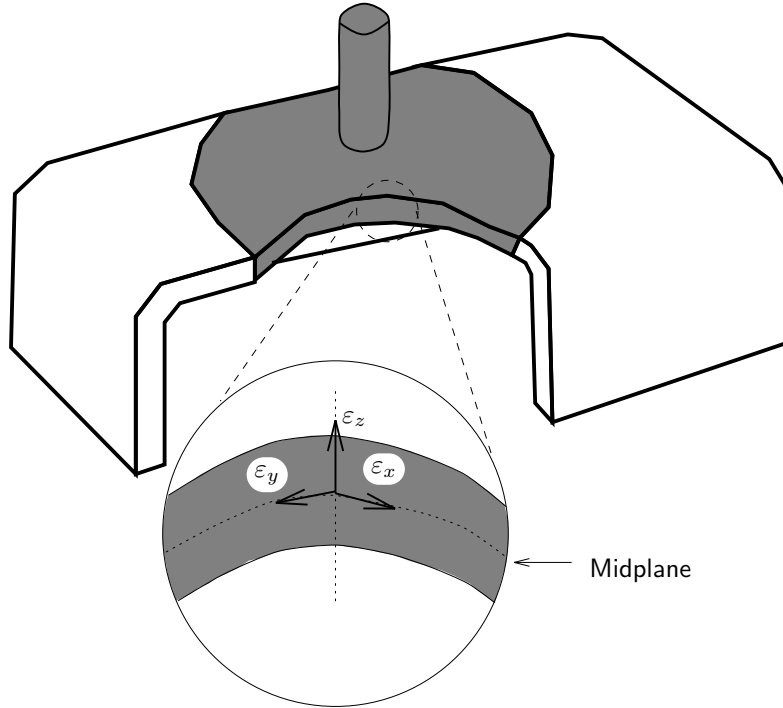
Figure 2.1: Local base $O_\varepsilon$

- the thermal conduction parallel to the midplane may be neglected with respect to conduction in $\vec{\varepsilon}_z$ direction.

- the velocity components in the $\vec{\varepsilon}_z$ direction are small compared to those tangent to the midplane.

- the mould is rigid, so the pressure field does not interact with the cavity dimensions.

The mould is cooled below the glass transition temperature causing the solidification of the melt that contacts the walls. These solid layers grow inwards from the mould walls during the process. In the solidified layers the velocity components parallel to the midplane are assumed to be zero while small non-zero velocity components in the $\vec{\varepsilon}_z$ direction may exist due to density changes. The local solid-liquid interface positions are given by $h^-\vec{\varepsilon}_z$ and $h^+\vec{\varepsilon}_z$ for the lower and upper solid layer respectively. The total local mould thickness is $h(\vec{x})$.

As a consequence of these simplifications, the deviatoric part of the rate of deformation tensor reduces to

$$\mathbf{D}^d = \frac{1}{2}\frac{\partial}{\partial z^\varepsilon}(\vec{v}^*\vec{\varepsilon}_z + \vec{\varepsilon}_z\vec{v}^*). \tag{2.13}$$

Then, the shear rate, defined as $\dot{\gamma} = \sqrt{2\mathbf{D}^d : \mathbf{D}^d}$, is given by $|\frac{\partial \vec{v}^*}{\partial z^\varepsilon}|$. With these simplifications the set of equations for a generalized Newtonian fluid read

$$\vec{\nabla}^* \cdot \vec{v}^* + \frac{\partial v_z^\varepsilon}{\partial z^\varepsilon} = -\frac{\dot{\rho}}{\rho}, \tag{2.14a}$$

$$\vec{\nabla}^* p = \frac{\partial}{\partial z^\varepsilon}\left(\eta \frac{\partial \vec{v}^*}{\partial z^\varepsilon}\right), \qquad \frac{\partial p}{\partial z^\varepsilon} = 0, \tag{2.14b}$$

$$\rho c_p \dot{T} = \frac{\partial}{\partial z^\varepsilon}\left(\lambda \frac{\partial T}{\partial z^\varepsilon}\right) + \eta \dot{\gamma}^2 - \frac{T}{\rho}\left(\frac{\partial \rho}{\partial T}\right)_p \dot{p}. \tag{2.14c}$$

The equations (2.14a)-(2.14c) are instationary, non-linear and coupled because viscosity and density are both temperature and pressure dependent.

## 2.2.2   Pressure and temperature problem

### Pressure problem

The pressure problem (PP) can be derived by integrating equations (2.14a) and (2.14b) over the thickness $\zeta$, eliminating the velocity components (Douven, 1991, Chapter 2). The resulting equations defining the PP read:

$$\vec{\nabla}^* \cdot (S\vec{\nabla}^* p) - \int\limits_{-h/2}^{h/2} \kappa \dot{p}\, d\zeta = -\int\limits_{-h/2}^{h/2} \alpha \dot{T}\, d\zeta, \tag{2.15}$$

with

$$S = J_2 - \frac{J_1^2}{J_0}, \quad J_i = \int\limits_{h^-}^{h^+} \frac{X^i}{\eta}\, d\zeta, \tag{2.16}$$

and the boundary conditions:

- Injection area:  $\begin{cases} \|\frac{\partial p}{\partial \vec{n}^*}\| = q/S & \text{if } p < p_{\max} \\ p = p_{\max} & \text{otherwise} \end{cases}$
- Mould walls:  $\|\frac{\partial p}{\partial \vec{n}^*}\| = 0$
- Flow fronts:  $p = p_{\text{atm}}$

$$\tag{2.17}$$

where $S$ is the fluidity, $q$ the prescribed volume flux per unit of length, $\vec{n}^*$ the normal vector in midplane of product and $p_{\max}$ and $p_{\text{atm}}$ the maximum machine pressure and the atmospheric pressure respectively.

Once the pressure is known, the velocity $\vec{v}^*$ can be evaluated with (Douven, 1991)

$$\vec{v}^*(z^\varepsilon) = \int\limits_{z^\varepsilon}^{h^+} \frac{1}{\eta}\left(X - \frac{J_1}{J_0}\right) dX \; \vec{\nabla}^* p. \tag{2.18}$$

**Temperature problem**

The temperature problem (TP) can be summarized as:

$$\rho c_p \dot{T} = \frac{\partial}{\partial z^\varepsilon}\left(\lambda \frac{\partial \vec{T}}{\partial z^\varepsilon}\right) + \eta \dot{\gamma}^2 - \frac{T}{\rho}\left(\frac{\partial \rho}{\partial T}\right)_p \dot{p}, \tag{2.19}$$

with the boundary conditions:

- Injection area: $\quad T = T_i$
- Lower mould wall: $\quad \lambda \frac{\partial T}{\partial z^\varepsilon} = H^-(T - T_w^-)$
- Upper mould wall: $\quad \lambda \frac{\partial T}{\partial z^\varepsilon} = H^+(T - T_w^+)$
- Or: cooling to air: $\quad \lambda \frac{\partial T}{\partial z^\varepsilon} = H_a(T - T_a)$ (after ejection)

$$\tag{2.20}$$

where $T_i$ is the injection temperature of the melt, $T_w^-$, $T_w^+$ the lower and upper mould wall temperatures, $T_a$ the ambient temperature, and $H^-$, $H^+$, $H_a$ the heat transfer coefficients of the lower and upper mould wall and to the air respectively.

## 2.3   Particle tracking

In simulating the multi-component injection moulding process it is necessary to know where and when a material particle has to be injected to end up at the desired position in the product. Particle tracking can be carried out by constructing the flow path $\ell$ for a certain particle. The track of a particle during the time span $[t, t-s]$ can be constructed by using:

$$\vec{x}_s = \vec{x}_s(\vec{x}, t; t-s). \tag{2.21}$$

Equation (2.21) states that $\vec{x}_s$ is the position at $t-s$ of a particle which occupies the position $\vec{x}$ at time $t$. Connecting all positions $\vec{x}_s$ with $s \in [0, t]$, its total particle track (or flowpath) is obtained. Summarizing, the trajectory $\ell$ of a particle which occupies the position $x$ at time $t$ can be expressed as:

$$\ell : \vec{x}_s = \vec{x}_s(\vec{x}, t; t-s) \quad \forall\, s \in [t_0, t]. \tag{2.22}$$

Because the velocity vector $\vec{v}(\vec{x}, t)$ is tangent to $\ell$, the flow path can be obtained by integrating

$$\frac{\mathrm{d}\vec{x}}{\mathrm{d}t} = \vec{v}(\vec{x}, t) \quad \text{with initial condition:} \quad \vec{x}_0 = \vec{x}(t = t_0). \tag{2.23}$$

This initial value problem can be adequately solved by a Runga-Kutta integration method (Crochet *et al.*, 1984; Caspers, 1991). Employing this method, the velocity field of several timesteps in the past has to be stored, which requires extra storage capacity.

An alternative method of particle tracking is to identify particles, when entering the flow domain, with an unique set of labels $\xi$, representing their 'identity' (Peters, 1989; Zoetelief, 1992). During flow, the identity of each particle does not change (figure 2.2). Using the formal definition of a material
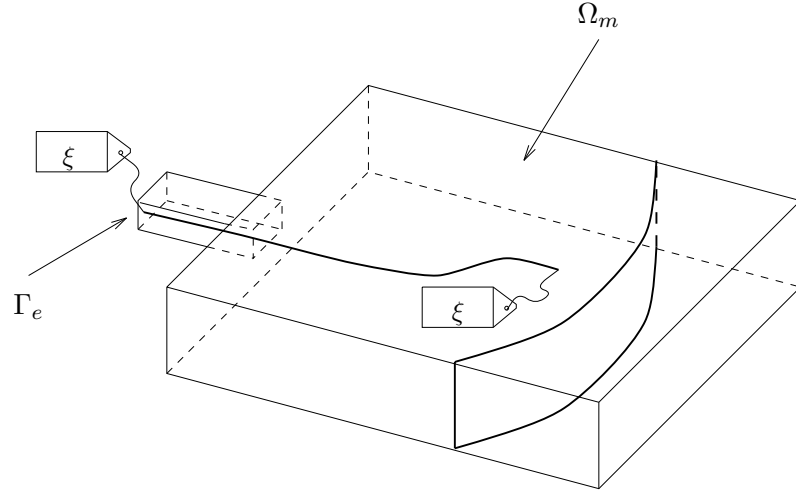


Figure 2.2: Conservation of identity of a particle (labeling)

derivative

$$\frac{D\phi}{Dt} \overset{\text{def}}{=} \dot{\phi} = \frac{\partial\phi}{\partial t} + \vec{v} \cdot \vec{\nabla}\phi, \tag{2.24}$$

(with the spatial derivative $\partial\phi/\partial t$ defined as the rate of change of $\phi$ at a fixed position in space) the conservation of identity can be expressed as

$$\dot{\underset{\sim}{\xi}} = \frac{D\underset{\sim}{\xi}}{Dt} = \underset{\sim}{0} \quad \text{in } \Omega_m, \quad \text{with } \underset{\sim}{\xi}(\vec{x}, t) = \underset{\sim}{f}(\vec{x}, t) \text{ on } \Gamma_e, \tag{2.25}$$

where $\underset{\sim}{\xi}$ is for instance a column containing the starting position and time $(x_0, y_0, z_0, t_0)$, $\Gamma_e$ the injection area and $\Omega_m$ the cavity geometry. The problem of particle tracking can then be solved with either a Lagrangian (moving frame of reference) or an Eulerian approach (fixed frame of reference).

**Eulerian approach**    In a fixed frame of reference the conservation of identity can be expressed as:

$$\frac{\partial \underset{\sim}{\xi}}{\partial t} + \vec{v} \cdot \vec{\nabla} \underset{\sim}{\xi} = \underset{\sim}{0}. \tag{2.26}$$

In this representation the change of label values in space is calculated instead of tracking pre-defined particles. The actual tracking can be carried out by determining the positions of a given set of labels in time if materials with identical material properties are used. For use in multi-component injection moulding, label values at the end of filling provide all the necessary information: i.e. where and when all particles had entered the mould. By defining a specific, desired shape and position of a second component inside a product, only the label values of these particles have to be determined to know what configuration should have been injected to realize this desired multi-component product.

The main advantage of this method is the use of field information rather than tracking a set of particles. For every given material distribution the injection sequence can be determined easily by looking for the label values, the actual particle tracking has not to be performed again. In the Lagrangian approach every newly defined set of particles result in restarting the particle tracking procedure. Moreover, velocity data at every time step must be available which requires large storage capacity. Another advantage is that the method is somewhat less sensitive to erroneous velocity values, e.g. a velocity that points out of the mould. When trying to determine the particle trajectory in this case, the particle will end up outside the mould and the method fails (Caspers, 1991).

## 2.4   Front flow

In mould filling, two flow regimes can be distinguished: the main flow domain and a front flow. In the last, the fountain effect occurs while in the main flow a simple 2D stratified flow situation exists (see figure 2.3). The fountain flow affects the particle distribution in moulded products, especially for material elements close to the mould walls. Also, break-through of core layers towards the surface of a product is completely controlled by the fountain region. For those reasons it is important to incorporate the fountain flow in the modelling of moulding processes.
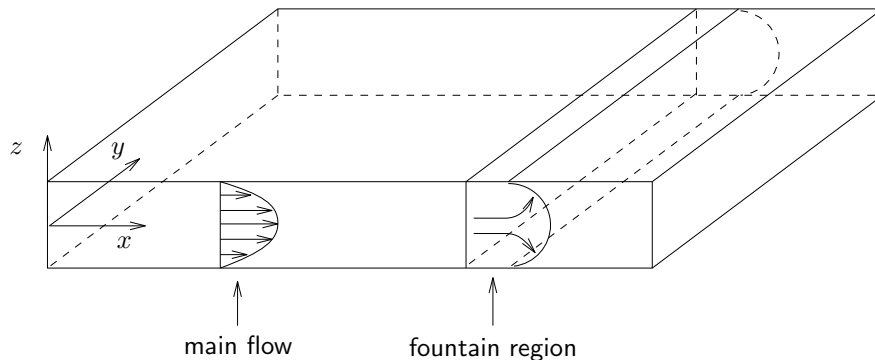
Figure 2.3: Fountain region in the Hele-Shaw approximation

In the idealized fountain flow, the residence time is neglected and a simple model, based on conservation of mass, is applied (Manas-Zloczower *et al.*, 1987; Dupret and Vanderschuren, 1988; Sitters, 1988). In these approaches, the fountain flow region simplifies to a single straight line that moves with the average front velocity $\bar{v}_s$ (see figure 2.4). Particles that enter the front region at a position $z_i$ will be transported instantaneously to a position $z_o$ where they leave the front. The relation between the ingoing position $z_i$ and the outgoing position $z_o$ is only governed by a local mass balance on the front line. Depicting the fountain flow in the Lagrangian framework with the mould wall moving with $-\bar{v}_s$, the front flow can be divided in two parts (figure 2.4): a high-velocity region $0 < z < z_f$ and a low-velocity region $z_f < z < h/2$, where $z_f$ is the position where $v_s(z) = \bar{v}_s$. According to the
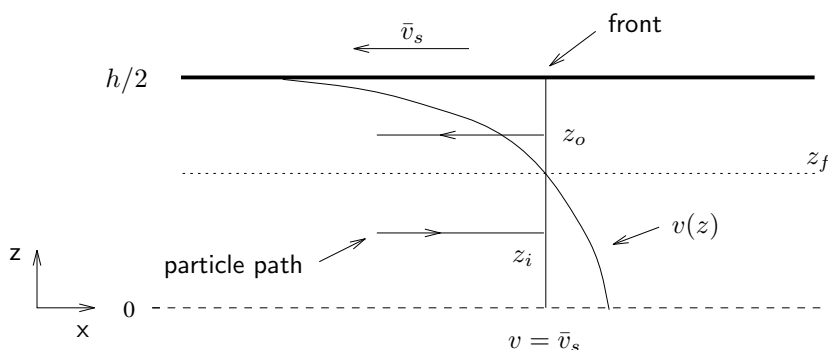


Figure 2.4: Lagrangian representation of simplified front model (only one mould half is considered)

balance of mass (assuming an incompressible fluid), the relation between the

inflow $z_i$ and the outflow position $z_o$ can be expressed by:

$$\int_{z_i}^{z_f} (v_s(\zeta) - \bar{v}_s) \, d\zeta = \int_{z_f}^{z_o} (\bar{v}_s - v_s(\zeta)) \, d\zeta \qquad (2.27)$$

In the case of a Newtonian fluid (in an isothermal flow) it can be derived easily that the folding line is positioned at $z_f = \frac{h}{2\sqrt{3}}$. Substituting the main flow velocity profile into equation (2.27) and integrating, results in the relation

$$z_o^3 - z_o + z_i - z_i^3 = 0. \qquad (2.28)$$

In a similar way the expression for a Power Law fluid reads (Manas-Zloczower *et al.*, 1987):

$$z_o^{\frac{1}{n}+2} - z_o + z_i - z_i^{\frac{1}{n}+2} = 0. \qquad (2.29)$$

In this case the position of the folding line is $z_f = (\frac{1}{n} + 2)^{\frac{-n}{1+n}} \frac{h}{2}$. For models that predict the viscosity more accurately (e.g. Cross model or Carreau model) the folding line is situated between the extremes given by the Newtonian and the Power Law fluid. The actual position depends on the shear rate and the material constants $n$ (the power law index) and $\tau^*$ (denoting the transition from the Newtonian plateau to the shear-thinning region). For these viscosity models the folding line can best be determined by evaluating equation (2.27). Using this approach, an estimation can be made of the gapwise distribution of particles with material quantities attached. It should be noted that it is assumed that these properties are not influenced by the (fountain) flow.

For some applications, the residence time in the fountain flow region is of importance, e.g. in the case of multi-component or in reactive injection moulding (Castro and Macosko, 1982). For a Newtonian fluid, the semi-analytical model of Bhattacharji and Savic (1965) gives the opportunity to derive a relation between the residence time in the front flow and the inflow or outflow position (Zoetelief, 1992; Peters *et al.*, 1994). The original Bhattacharji and Savic model gives an analytical expression of the velocity field in the fountain region (see Appendix A) from which the flow paths can be constructed (figure 2.5). The residence time as function of the inflow or outflow position can be computed by integrating along a flow-path until the particle re-enters the main flow. This representation can be parameterized by fitting the curves obtained with a polynomial function. In doing so, not much extra computing effort is required for incorporating the residence time distribution into a front model.
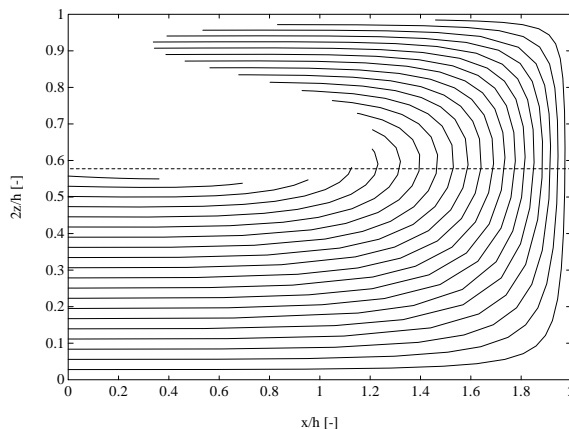
Figure 2.5: Flow paths in the fountain region for a certain time interval

For non-Newtonian viscosity models, the gapwise velocity profile does not correspond to the parabolic profile of a Newtonian fluid. Therefore, the model of Bhattacharji and Savic can only be applied when no precise information is needed.

In cases where it is desirable to incorporate fountain effects more accurately, particle trajectories can be determined separately by solving the fountain flow problem given the flow field at the line that separates the main flow domain from the fountain flow region. Moreover, such a procedure gives the opportunity to alter the shape of the flow front itself. In the most existing models, the flow front is considered as a straight line. In practice the flow front is of course more like a semi-circle (see e.g. Mavridis *et al.*, 1986). Changing this flow front shape does, however, only affect the residence time in the front, since the relation between the ingoing and outgoing position is completely determined by a local mass balance. The final comparison of two different fountain flow models is presented in Appendix A.

## 2.5   Multi-component flows

In multi-component flows a discontinuity in material properties is present at the interface between the components. Instead of modelling the interface, discontinuous functions can be used for the material properties. In order to satisfy the conservation of mass, the global conservation laws have to be adapted for incorporating the discontinuous functions.

### 2.5.1   Interface modelling

Consider a time-dependent volume $V(t)$ that is divided into subvolumes $V_k(t)$. The subvolumes correspond with parts of the total volume that have specific material properties, like density $\rho_k$ and viscosity $\eta_k$. The local mass conservation yields (Müller, 1984)

$$\frac{\partial \rho_k}{\partial t} + \vec{\nabla} \cdot (\rho_k \vec{v}_k) = 0, \tag{2.30}$$

and the local balance of momentum with discontinuities over the material interface is given by

$$\rho_k \frac{\partial \vec{v}_k}{\partial t} + \rho_k (\vec{u}_k \cdot \vec{\nabla}) \vec{u}_k - \vec{\nabla} \cdot \boldsymbol{\sigma}_k = \rho_k \vec{f}_k. \tag{2.31}$$

For simplicity, the contribution of surface tension at the interfaces is neglected here.

### 2.5.2   Inverse mapping

The ultimate goal of simulation of the injection moulding process, is to predict the process conditions given the required product properties. In the case of multi-component injection moulding it is important that one can predict the injection sequence on beforehand, since for complex geometries it is almost impossible to do this by trial-and-error. The task to complete can be summarized as:

> Given the particle distribution at the end of the filling stage and the definition of a required layer distribution, determine the injection configuration and sequence necessary in order to attain that pre-set definition.

In our case, the particle distribution is given by the label field $\tilde{\xi}$.

For one-component flow, like occurring in multi-colour injection, the label field contains all the information necessary to determine the injection configuration and the inverse mapping can be carried out straightforward (as a post-processing task). For multi-component flows, however, the material distribution influences the flow kinematics. In that case the injection configuration has to be obtained iteratively:

1. Perform a filling simulation with one component.

2. Determine the injection sequence given the required material distribution.

3. Perform a multi-component filling simulation with the injection sequence determined under step 2 as input.

4. Repeat steps 2 and 3 until the injected and calculated injection sequences correspond to a sufficient degree.

## 2.6   Piston driven flow

In the piston driven flow problem, which is drawn schematically in figure 2.6, a fluid is advancing between two pistons in a tube. In contrast to the mould-
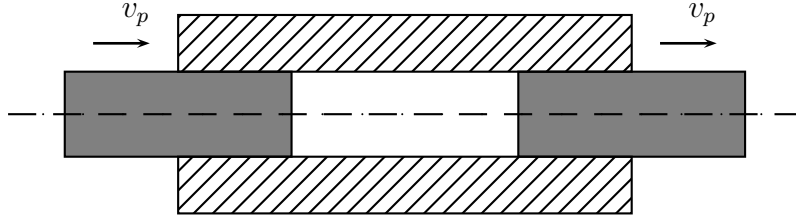


Figure 2.6: Schematic representation piston driven flow problem

ing processes dealt with in the preceding sections, the piston driven flow, with or without contraction, is modelled via the instationary Navier-Stokes equations for incompressible fluids. These equations can be derived from the equations for conservation of mass (2.1) and balance of momentum (2.2) using Newton's constitutive equation (2.5),(2.6a) and read:

$$\rho\frac{\partial \vec{v}}{\partial t} + \rho(\vec{v} \cdot \vec{\nabla})\vec{v} - \vec{\nabla} \cdot \boldsymbol{\sigma} = \rho\vec{f}, \tag{2.32a}$$

$$\vec{\nabla} \cdot v = 0, \tag{2.32b}$$

$$\boldsymbol{\sigma} = -p\mathbf{I} + \eta(\vec{\nabla}\vec{v} + (\vec{\nabla}\vec{v})^c). \tag{2.32c}$$

Substituting equation (2.32c) in equations (2.32a) and (2.32b) and introducing the dimensionless variables

$$\vec{\nabla} = \frac{1}{L}\vec{\nabla}', \ \vec{v} = V\vec{v}', \ p = \frac{p'}{\rho V^2}, \ \vec{f} = \frac{L}{V^2}f', \ t = \theta t', \ \eta = \eta_0\eta', \tag{2.33}$$

and omitting the accents yields

$$Sr\frac{\partial \vec{v}}{\partial t} + (\vec{v} \cdot \vec{\nabla})\vec{v} - \frac{1}{Re}(\vec{\nabla} \cdot \eta\vec{\nabla})\vec{v} + \vec{\nabla}p = \vec{f}, \tag{2.34a}$$

$$\vec{\nabla} \cdot v = 0 \tag{2.34b}$$

where the Reynolds number $Re$ is defined as $Re = \frac{\rho V L}{\eta_0}$ and the Strouhal number $Sr$ as $Sr = \frac{L}{\theta V}$ with $\theta$ being a characteristic time.

The boundary of the computational domain $\Omega$ is supposed to consist of two non-overlapping parts $\Gamma_v$ and $\Gamma_\sigma$ on which the velocity (essential boundary conditions) or the stress (natural boundary condition) can be prescribed:

$$\vec{v} = \vec{g} \qquad \text{on } \Gamma_v, \tag{2.35}$$

$$\boldsymbol{\sigma} \cdot \vec{n} = \vec{h} \qquad \text{on } \Gamma_\sigma. \tag{2.36}$$

An initial condition at $t = 0$ has to be applied to complete the set of equations:

$$\vec{v}(\vec{x}, 0) = \vec{v}_0 \qquad \text{in } \Omega. \tag{2.37}$$

The variables $\vec{g}$, $\vec{h}$, and $\vec{v}_0$ are arbitrary functions that depend on the problem considered.

Since the Reynolds number is typically $\mathcal{O}(10^{-3} - 10^{-6})$, the inertia term $(\vec{v} \cdot \vec{\nabla})\vec{v} = \mathcal{O}(1)$ is negligible small compared to the term preceded by $Re^{-1}$ and therefore may be omitted.

The thus obtained instationary Stokes equations read as:

$$Sr\frac{\partial \vec{v}}{\partial t} - \frac{1}{Re}(\vec{\nabla} \cdot \eta\vec{\nabla})\vec{v} + \vec{\nabla}p = \vec{f}, \tag{2.38a}$$

$$\vec{\nabla} \cdot v = 0. \tag{2.38b}$$

with the initial condition (2.37) and boundary conditions (2.35), (2.36). Further simplification can be established by neglecting the time derivative. For the problems encountered in this thesis this is justified, since $Sr$ is negligible small compared with $Re^{-1}$. The piston driven flow problem either without or with the contraction are modelled using the thus obtained instationary Stokes equations.

In non-isothermal flow situations, the Navier-Stokes equations are coupled via the viscosity with the energy equation (2.4) or (2.11):

$$\rho c_p \dot{T} = (\vec{\nabla} \cdot \lambda\vec{\nabla})T + \eta\dot{\gamma}^2, \tag{2.39}$$

where the shear rate is defined as $\dot{\gamma} = \sqrt{2\boldsymbol{D}^d : \boldsymbol{D}^d}$.

## 2.7   Conclusions

The balance and constitutive equations given in this chapter can be applied for simulating the conventional as well as the multi-component injection moulding process. In the latter case, an extra conservation law is

added to solve the particle tracking problem. A strategy is given to model multi-component flows using different material properties for each component which results in an interface represented by the discontinuity of those properties. In the next chapter, the numerical aspects of solving these equations are discussed.

# Chapter 3

# Numerical solution strategies

In this chapter, the numerical solution of the equations defined in Chapter 2 is discussed. Section 3.2 deals with the numerical methods used for solving the problems defined in multi-component injection moulding. Special attention will be paid to the method used for particle tracking and for the fountain flow phenomena. In Section 3.3 the numerical solution of the piston driven flow will be described. Here, the combined flow of a polymer melt in between two (extremely high viscous) pistons, will be emphasized. Finally, Section 3.4 gives some concluding remarks.

The extension of the filling stage of the conventional injection moulding process to multi-component injection moulding is implemented in VI$p$, a package for the simulation of moulding processes developed at Eindhoven University of Technology. This program make use of the finite element package SEPRAN (Segal, 1984).

## 3.1  Temporal discretization

To solve the sets of non-linear partial differential equations derived in Section 2.2 numerically, the problem has to be discretized in both space and time to get an approximate solution. For the temporal discretization the time domain $\mathcal{T} = [0, t_{\mathrm{end}}]$ is divided in $n_t$ intervals according to

$$\mathcal{T} = \bigcup_{n=0}^{n_t} \mathcal{T}_{n+1}, \quad \mathcal{T}_{n+1} = [t_n, t_{n+1}], \quad \Delta t_{n+1} = t_{n+1} - t_n. \tag{3.1}$$

The time derivatives that occur in the equations for the pressure problem (2.15) and the temperature problem (2.19) are all material derivatives. The

material derivative of an arbitrary variable $\alpha$ is formally defined by

$$\frac{D\alpha}{Dt} \overset{\text{def}}{=} \dot{\alpha} \equiv \lim_{\theta \to 0} \frac{\alpha(\vec{x}, t + \theta \Delta t) - \alpha(\vec{s}, t)}{\theta \Delta t}, \tag{3.2}$$

where $\vec{s}$ denotes the position at time $t$ of the particle that is located at $\vec{x}$ at time $t + \Delta t$. Equation (3.2) can be approximated as:

$$\dot{\alpha}_{n+1} \approx \frac{\alpha_{n+1} - \alpha_c}{\Delta t_{n+1}} \tag{3.3}$$

where $\alpha_{n+1} = \alpha(\vec{x}, t + \theta \Delta t)$ and $\alpha_c = \alpha(\vec{s}, t)$. Now, it remains to determine the convected variable $\alpha_c$. Consider $\alpha_c \overset{\text{def}}{=} \alpha(\vec{s}(\vec{x}, t_{n+1}), t_n)$ as a field variable. This field can be obtained by convecting the variable field at $t = t_n$, $\alpha_n \overset{\text{def}}{=} \alpha(\vec{x}, t_n)$ by the known velocity field $\vec{v}(\vec{x}, t)$. Hence, the variable $\alpha_c$ is determined by solving

$$\frac{\partial \alpha_c}{\partial t} + \vec{v} \cdot \vec{\nabla} \alpha_c = 0, \qquad \alpha_c(t_n) = \alpha_n. \tag{3.4}$$

Using this method, the convection operator can be splitted from the remainder of the equation. Although it differs from the operator splitting technique, where the convection operator is part of a larger operator as appears in e.g. the convection-diffusion equation or differential models in visco-elastic flow calculations (see e.g. Donea, 1991; Baaijens, 1992), the procedure is the same. The procedure can be summarized as follows: The solution field at $t - \Delta t$ is convected by a known velocity field. The outcome of this calculation provides the initial condition for the remaining part of the original equation for the current time step. The advantage of this method is that different numerical schemes can be used for solving different terms in the equations. Especially in the case of convection dominated problems this is a great benefit, since the classical schemes often show spurious oscillations.

## 3.2   Multi-component injection moulding

### 3.2.1   Spatial discretization

The spatial discretization is performed by using a *finite element method.* The different finite element meshes used are depicted in figure 3.1. The pressure problem requires a finite element mesh that covers the midplane of the product (figure 3.1a). The discretization is performed using biquadratic quadrilateral elements defined in $\mathbb{R}^2$ (Segal, 1984) with one degree of freedom
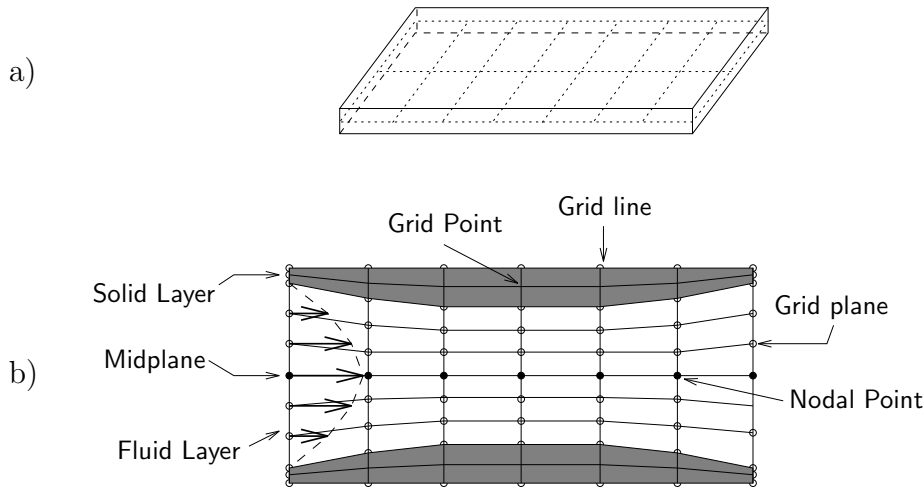
Figure 3.1: Spatial discretization in midplane (a) and perpendicular to that (b)

– the pressure – per node. Since realistic injection moulding products are three dimensionally shaped, the elements are situated in a 3D space.

The temperature problem is solved using one-dimensional finite element meshes consisting of linear elements in the gapwise direction of the product (figure 3.1b). These 1D-meshes are present in every vertex node (nodal point) of the 2D mesh of the pressure problem, which are named the gridlines. The nodal points of the 1D-meshes are called the gridpoints.

Finally, the convection problem – for determining the convected variables and particle tracking – is solved on meshes of bilinear quadrilateral elements in $\mathbb{R}^2$ (Segal, 1984). These meshes are formed by the gridplanes (figure 3.1b) which are the 2D planes spanned by the gridpoints.

Although the total product is discretized in three dimensions, the computation differs considerably from a complete 3D analysis. In a 3D computation the systems to be solved are normally very large, especially when temperature gradients in the thickness direction demands for a fine discretization which usually is the case in injection moulding. The systems to be dealt with in the so-called $2\frac{1}{2}$D approach are much smaller, since the gapwise and the midplane discretizations are decoupled, which is computationally much more efficient.

### 3.2.2   Pressure and temperature problem

**Pressure Problem**

Applying the splitting technique of the convection operator and an implicit Euler time-stepping to equation (2.15) yields:

$$-\vec{\nabla}^* \cdot (S_{n+1}\vec{\nabla}^* p_{n+1}) + \bar{\kappa}_{n+1}p_{n+1} = f_{n+1}, \tag{3.5}$$

where the subscript $n + 1$ denotes the new time step. The coefficient $\bar{\kappa}_{n+1}$ and the right-hand side $f_{n+1}$ are defined as:

$$\bar{\kappa}_{n+1} = \frac{1}{\Delta t_{n+1}} \int\limits_{-h/2}^{h/2} \kappa_{n+1}\, d\zeta, \tag{3.6}$$

$$f_{n+1} = \frac{1}{\Delta t_{n+1}} \int\limits_{-h/2}^{h/2} \alpha_{n+1}(T_{n+1} - T_c)\, d\zeta + \frac{1}{\Delta t_{n+1}} \int\limits_{-h/2}^{h/2} \kappa_{n+1}p_c\, d\zeta, \tag{3.7}$$

in which $T_c, p_c$ denote the convected temperature and pressure respectively. Equation (3.5) is a second order elliptic differential equation and is solved using the Bubnow-Galerkin finite element method with the pressure as the unknown. As the pressure is biquadratic per element, the pressure gradient $\vec{\nabla}^* p$ and thus the velocity $\vec{v}^*$, which is a function of $\vec{\nabla}^* p$ (see equation (2.18), are bilinear per element. Obviously, the velocity parallel to the midplane $\vec{v}^*$ and the pressure gradient $\vec{\nabla}^* p$ have the same direction.

For calculating the integrals over the thickness, the grid is divided in $n_{elgrp}$ parts, $n_{elgrp} = 2$ for symmetrical problems and $n_{elgrp} = 3$ for asymmetrical temperature boundary conditions. These parts coincide with the solid and fluid parts of the grid lines. The fluid layer is discretized using $n_f$ gridpoints that form an equidistant grid and the solid layer is divided in the same way in $n_s$ gridpoints. For convenience, double nodes are present at the fluid-solid interfaces. The integrals in the $z^\varepsilon$ direction in the pressure problem are approximated by

$$\int\limits_{-h/2}^{h/2} f(\zeta)\, d\zeta \approx \sum_{i=1}^{n_{fs}} \sum_{j=1}^{n_{elgrp}} f_i w_{j,i} \tag{3.8}$$

where $n_{fs} = n_f + n_s$ or $n_{fs} = n_f + 2n_s$ for symmetrical or asymmetrical problems respectively. The weighting factors for the symmetrical case are defined as:

$$
w_{1,i} = \begin{cases} \frac{2h^+}{n_f - 1} & \text{if } i = 1 \text{ or } i = n_f \\ \frac{4h^+}{n_f - 1} & \text{if } 1 < i < n_f \\ 0 & \text{otherwise} \end{cases} \tag{3.9}
$$

$$
w_{2,i} = \begin{cases} \frac{h - 2h^+}{n_s} & \text{if } i = n_f \text{ or } i = n_{fs} \\ \frac{2h - 4h^+}{n_s} & \text{if } n_f < i < n_{fs} \\ 0 & \text{otherwise} \end{cases} \tag{3.10}
$$

and for the asymmetrical case as:

$$
w_{1,i} = \begin{cases} \frac{h^- - h}{n_s} & \text{if } i = 1 \text{ or } i = n_s + 1 \\ \frac{2(h^- - h)}{n_s} & \text{if } 1 < i < n_s + 1 \\ 0 & \text{otherwise} \end{cases} \tag{3.11}
$$

$$
w_{2,i} = \begin{cases} \frac{h^+ - h^-}{n_f - 1} & \text{if } i = n_s + 1 \text{ or } i = n_s + n_f \\ \frac{2(h^+ - h^-)}{n_f - 1} & \text{if } n_s + 1 < i < n_s + n_f \\ 0 & \text{otherwise} \end{cases} \tag{3.12}
$$

$$
w_{3,i} = \begin{cases} \frac{h - h^+}{n_s} & \text{if } i = n_s + n_f \text{ or } i = n_{fs} \\ \frac{2(h - h^+)}{n_s} & \text{if } n_s + n_f < i < n_{fs} \\ 0 & \text{otherwise} \end{cases} \tag{3.13}
$$

Assembling the weighting vector $w$ and calculating the dot product $(w \cdot f)$ gives the approximation of the integral according to the trapezium rule. In case of calculating the fluidity, the weight factors in the solid layer, $w_{2,i}$ for the symmetrical and $w_{1,i}, w_{3,i}$ for the asymmetrical case, are set to zero.

**Temperature problem**

Analogous to the pressure problem, equation (2.19) can be discretized with respect to time and reads

$$
-\frac{\partial}{\partial z^\varepsilon} \left( \lambda_{n+1} \frac{\partial T_{n+1}}{\partial z^\varepsilon} \right) + \bar{\nu}_{n+1} T_{n+1} = g_{n+1}, \tag{3.14}
$$

where $\bar{\nu}_{n+1}$ and the right-hand side $f_{n+1}$ are given by

$$\bar{\nu}_{n+1} = \frac{1}{\Delta t_{n+1}} \left[ \rho_{n+1} c_{p,n+1} + \left( \frac{\partial \rho}{\partial T} \right)_{p,n+1} \frac{p_{n+1} - p_c}{\rho_{n+1}} \right], \qquad (3.15)$$

$$g_{n+1} = \eta \dot{\gamma}^2 + \frac{\rho_{n+1} c_{p,n+1} T_c}{\Delta t_{n+1}}. \qquad (3.16)$$

Equation (3.14) is a second order elliptic equation which is solved using the Bubnow-Galerkin finite element method. The transport of heat is incorporated by the convective variable $T_c$.

Since the pressure- and temperature problems form a coupled, non-linear set of differential equations, they have to be solved iteratively. Moreover, the computational domain changes with time because of the moving flow front. The propagation of the flow front is carried out with the source propagation method (Sitters, 1988; Caspers *et al.*, 1994). In this method, every point on the flow front acts as a (point) source and fills a certain circular area with radius $\Delta x = \vec{v}_n^* \Delta t$. The envelope of all these circles give the new flow front position. The new mesh is constructed by connecting the intersections of the envelope with the element edges of a background mesh that covers the complete product. Only that part of the background mesh that contains intersections with the flow front envelope has to be remeshed temporary, the part that contains completely filled elements only, remains unchanged.

The calculation of the filling stage is executed in the following steps:

1. determine the flow front position based on the velocity field of the previous time step and perform a local remeshing of the background mesh.

2. map the solution field from the old mesh (previous time step) to the mesh constructed in step 1.

3. determine the convected variables $T_c$ and $p_c$.

4. solve the pressure problem.

5. solve the temperature problem.

6. update the material function using the calculated pressure-, temperature-, and shear rate fields.

7. repeat step 3 to 5 until convergence is achieved.

8. perform particle tracking.

9. generate output for post-processing.

10. update the time step if the product is not yet filled completely and return to step 1.

### 3.2.3  Convection problem

The particle tracking problem as modelled by the conservation of identity and the splitting technique of the convection operator are based on the same instationary scalar convection equation. This partial differential equation is hyperbolic of nature and needs special treatment to avoid spurious oscillations in the solution (see e.g. Donea, 1991). The time derivative in equation (2.26) is approximated by a two-step $\theta$-method (van de Vosse, 1987). Application of this method to the equation

$$\frac{\partial \alpha}{\partial t} = f, \tag{3.17}$$

results in

$$\frac{\alpha_{n+\theta} - \alpha_n}{\theta \Delta t} = f_{n+\theta}, \tag{3.18}$$

with

$$f_{n+\theta} = \theta f_{n+1} + (1-\theta) f_n, \tag{3.19}$$
$$t_{n+\theta} = t_n + \theta \Delta t. \tag{3.20}$$

The value at the new time level is given by

$$\alpha_{n+1} = \frac{1}{\theta} \alpha_{n+\theta} - \frac{1-\theta}{\theta} \alpha_n. \tag{3.21}$$

Here $\theta$ is a parameter in the interval $0 < \theta \leq 1$. This scheme is unconditionally stable for $\theta \geq 0.5$. For $\theta = 1$ the scheme reduces to the Euler implicit method which has an accuracy of $\mathcal{O}(\Delta t)$. The well-known Crank-Nicholson scheme appears for $\theta = 0.5$ which is $\mathcal{O}(\Delta t^2)$ accurate. The two-step scheme can be considered as a Euler implicit step to time level $n + \theta$ followed by an extrapolation to the required time level $t_{n+1}$.

Applying the $\theta$-method to equation (2.26) yields

$$\frac{\xi_{n+\theta} - \xi_n}{\theta \Delta t_{n+1}} + \vec{v}^*_{n+\theta} \cdot \vec{\nabla}^* \xi_{n+\theta} = 0, \tag{3.22}$$

followed by the extrapolation step according to equation (3.21). Because of its relatively high accuracy the Crank Nicholson $\theta = 0.5$ scheme is chosen in the calculations.

The solution of equation (3.22) is carried out with the Streamline Upwind Petrov Galerkin (SUPG) finite element method (Brooks and Hughes, 1982). The SUPG method provides stable solutions in case of convection dominated

flows with discontinuities in the solution as may occur in the particle tracking problem. However, some numerical dispersion may occur both down- and upstream of such a discontinuity. The performance of the scheme chosen is demonstrated in Appendix B.

The convection equation is solved on a finite element mesh consisting of bilinear quadrilateral elements coinciding with the gridplanes that are situated in the fluid layer (figure 3.1b). The gridplanes are slightly curved in the direction of the flow (figure 3.1b) following the shape of the already solidified layer. In this way a rough approximation of the (small) velocity component $v_3^\varepsilon$ is established (without explicitly calculating it), since the gridpoints are equally divided between the midplane and the solid/liquid interface.

## 3.2.4 Bifurcations of the midsurface

When a product consists of thin walled sections with their normal vectors not pointing in the same direction (as is usually the case), bifurcations of the midsurface exists. In nearly all existing simulation codes one pressure value is present at the intersection points of those branches but, of course, a different pressure gradient may exist for each separate branch. All other properties like e.g. temperature are equalized in the intersection points. In case of e.g. T-junctions, whose upstream part is connected with two downstream parts, this leads to an unrealistic distribution of properties of material particles. Couniot *et al.* (1993) showed numerically that, when dealt with correctly via a proper splitting of the flow, an initially symmetric gapwise temperature distribution in the upstream part of the connection results in asymmetrical distributions in the downstream parts (figure 3.2) instead of the symmetrical distribution that is usually taken for granted.
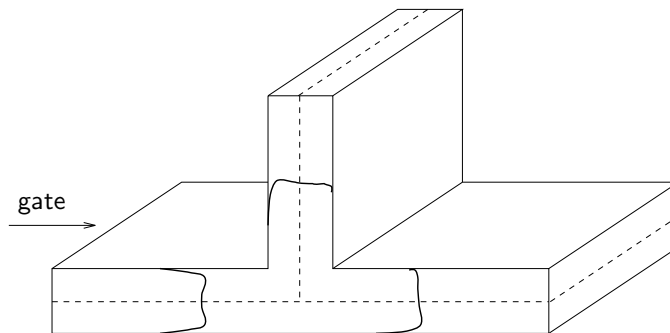


Figure 3.2: Temperature distribution in a T-junction (after Couniot *et al.*(1993))

The origin of this erroneous distribution stems from the fact that conservation of mass is only taken into account in the calculation of the pressure

field when employing the $2\frac{1}{2}$D approach. The mass balance is only weakly satisfied by imposing that at flow splittings the sum of the downstream fluxes equals the upstream outflow flux. In order to deal with these splittings properly, local conservation of mass has to be satisfied for all those properties that are dependent of the flow history (such as temperature, density, stresses, orientation, conversion, etc.) or for the particle identity. In the case of bifurcations this demands for a special treatment.

The improved strategy in resolving the convection problem is to split the product geometry into parts that contain no bifurcations, but that can be considered as 2D flow geometries. At the intersections, the values at the inflow boundaries of the downstream branches are considered as inflow boundary conditions (Dirichlet condition). Then, the convection problem is solved for each part separately, irrespective of the order of filling. After convection, the values at the inflow boundaries of the downstream branches are updated using the calculated values at the outflow branches of the upstream sections. Hereby, it is assumed that the time steps taken are small enough so that the material particles do not cross the opposite element boundaries, which is in fact the well known Courant-Friedrichs-Lewy (CFL) condition (Hirsch, 1990).

During updating the values at the downstream inflow boundaries, local mass conservation has to be satisfied. Suppose that there are $n$ outflow boundaries and $m$ inflow boundaries. For every inflow boundary $i$ the fractional thickness $f_{i,j}$ of the connected outflow boundaries $j$ that fills the inflow part is determined by a local mass balance. Let $f_{i,j} = [f^-, f^+]$, then the fractional thickness can be determined by solving

$$\int_{f^-}^{f^+} v_j^*(z)dz = q_i \tag{3.23}$$

where $v_j^*(z)$ is the velocity profile of the outflow boundary $j$ and $q_i$ the volume flux at the inflow boundary $i$. An additional relation has to formulated to determine the positions $f^-, f^+$ completely. For that purpose, the spatial sequence of the element groups around a connection node is taken into account. For example in the case of two inflow nodes connected with one outflow node (see figure 3.2) $f_{1,1} = [-h/2, f^+]$ and $f_{2,1} = [f^+, h/2]$. Whether a connection curve is a inflow or outflow boundary is checked by evaluating the dot product $(\vec{\nabla}^* p \cdot \vec{n})$ with $\vec{n}$ the outward normal vector parallel to the midplane.

The gapwise values of any property to be convected can be distributed over the connected downstream points by simply mapping the values in the

fractional thicknesses of the upstream points to the inflow gridlines. In this way, local conservation of mass is only weakly satisfied. A further improvement is to preserve mass conservation by evaluating

$$\int\limits_{z_1}^{z_k} v_d^*(\zeta)\, d\zeta = \int\limits_{f_{i,j}}^{s} v_u^*(\zeta)\, d\zeta \qquad k = 2, .., nf \tag{3.24}$$

where $v_d^*, v_u^*$ are the gapwise velocities at the down- or upstream node respectively and $s$ the gapwise position at which the value has to be determined. This latter method can also be applied when an abrupt change of thickness exist at the interconnection between two parts. This could be useful when the shape of the velocity profile is expected to change much with in- or decreasing flow rate, e.g. when using shear-thinning liquids or materials with a yield stress.

### 3.2.5    Fountain flow

In the thin film or lubrication approximation the fountain region is reduced to a front perpendicular to the midplane. Since in the midplane no pressure gradient normal to the flow direction exists, the front can be further simplified to a single straight line in every node situated on the melt front. When defining the folding point as the position where the velocity equals the average front velocity, the front line can be divided in two regions: gridpoints that are situated between the folding points and those that are between the folding points and the walls. Only the latter gridpoints have experienced the fountain effect, the others are entering the front region. The parameterized front model gives for those points the residence time in the front and the entrance position.

How to incorporate the fountain effect depends on whether the residence time is included or not. In both cases particle tracking is carried out first in the whole computational domain before applying the front model to the gridpoints situated at the flow front. The gridpoints between the folding points get their values naturally by solving the particle tracking problem in the fluid. When neglecting the residence time, a material particle at a certain gridpoint between the folding point and the wall originates from a position $z_i$ between the folding points on the front line. The position $z_i$ is given by the parameterized model or by a local mass balance according to equation 2.27.

In case of incorporation of the residence time, the values cannot be taken from the front line directly anymore, but have to be found at a spatial position $\vec{x}^{fp}$, the position of front passage ($fp$). This position corresponds with the place where a certain particle that leaves the front at the actual time $t$ enters

the front region at a time $t^{fp} = t - t^{rf}$, with $t^{rf}$ the residence time in the front given by the parameterized model. The remaining problem for the field variable $\alpha$ considered is to determine $\alpha(\vec{x}^{fp}, t^{fp})$ of $\alpha$. For this purpose another field variable $\alpha^{fp}$ is introduced that contains the values at the nodes that are just filled during the past time step. In the same way, the velocity at front passage $\vec{v}_{fp}^{*}(z)$ is stored. Given the position $z_o$ where a particle leaves the front, the residence time $t^{rf}$ and the position $z_i$ are known. A gridpoint between the folding point and the wall can now be filled with a value taken from a position $z_i$ on the front line calculated by solving

$$\frac{\partial \alpha^{fp}}{\partial t} + \vec{v}_{fp}^{*}(z_i) \cdot \vec{\nabla}^* \alpha^{fp} = 0, \qquad \text{for } t \in [t^{fp}, t] \tag{3.25}$$

The solution of this convection equation is carried out in the same way as equation (3.22).

## 3.2.6   Interface modelling

The description of a discontinuity in the material properties, e.g. $\eta$ or $\rho$ (thus the injection of more than one component), in a spatial discretization problem is only possible if the material interfaces coincide with element boundaries. This implies that a suitable remeshing technique has to be implemented in order to follow interfaces between the two interfaces in time. Mavridis *et al.* (1987) used double nodes at the interfaces to model the discontinuity in the pressure field that arises when surface tension cannot be neglected or with viscosities being different. In that case two different values for the variables ($\vec{v}$ and $p$) are allowed on two nodes at the same spatial position. Such a method is relatively expensive since remeshing is needed at each interface.

In this study, three different type of interfaces can distinguished. First, there exists an interface between the polymer melt and the air during the filling. In the simulation the possible influence of the air is neglected and the front flow (interface) position is determined by local remeshing of the background mesh. The second type of interface is the one between the solid and the liquid layer, occurring in non-isothermal filling problems. This solid/liquid interface is modelled using the above mentioned double nodes at the melt-liquid interface(s). Remeshing has to be carried out on 1D meshes only (in the thickness direction), so not much computational effort is involved. The last type are the interfaces between two different materials that occur in multi-component injection moulding (or in the multi-material piston driven flow problems (see Chapter 5). These are modelled via a discontinuity in the material properties that are approximated by continuous functions with a steep gradient. The maximum steepness is controlled by the local

mesh size and the order of the element. It is assumed that the smoothing of discontinuities only has a local effect on the final solution. The main advantage of this approach compared to remeshing techniques is that it can be used easily in all kind of (complex) geometries in 2D or 3D. Examples of transient flow problems like mould filling, where the free surface is modelled by the transition from a high (polymer) viscosity to a low (air) viscosity can be found in Thompson (1986); Xie *et al.* (1991); Akkerman (1993). Other examples concern the interface between a reactive fluid and the already gelled material (Peters *et al.*, 1993).

In the latter interface modelling technique, the position of the moving interface(s) can be determined by using particle tracking. In accordance with the method presented in Section 2.3 an initial set of labels defining the particle identity is transported through the flow domain, thus representing the material distribution. By doing so, the material properties become also a function of the label values. The strategy is also used to model the piston driven (contraction) flow problem. The pistons are represented by an artificial high viscosity material which slips at the walls of the domain. This so-called fixed domain approach can be condidered as an variation of the version of the pseudo-concentration method as used by Thompson (1986).

## 3.3   Model flow problems

The problems descibed in this section refer to the piston driven flows (with or without a contraction) that are used to test the particle tracking (see chapter 5). Since these model flows are much simpler than the multi-component injection moulding problem (2D isothermal, rather than $2\frac{1}{2}$D non-isothermal), a simplified and fast test code has been written based on the finite element package SEPRAN (Segal, 1984).

### 3.3.1   Discretization

The Stokes equations (2.38) are solved using a standard Galerkin finite element method. The spatial discretization is performed with quadratic isoparametric triangular elements in $\mathbb{R}^2$ (Segal, 1984). The velocity components are the unknowns in all nodal points of the elements whereas the pressure and the pressure gradient are only known in the center node.

After spatial discretization of equation (2.38) and applying the Galerkin formulation the following set non-linear differential equations is derived (Cu-

velier *et al.*, 1986)

$$\mathbf{M}\frac{\partial \mathbf{v}}{\partial t} + \mathbf{S}(\mathbf{v})\mathbf{v} + \mathbf{L}^T\mathbf{p} = \mathbf{f} + \mathbf{b}, \tag{3.26a}$$

$$\mathbf{L}\mathbf{v} = 0, \tag{3.26b}$$

with $\mathbf{M}$ the mass matrix, $\mathbf{S}(\mathbf{v})$ the stress matrix, $\mathbf{L}^T\mathbf{p}$ the pressure gradient, and $\mathbf{L}\mathbf{v}$ denotes the divergence of the velocity. The right-hand side is formed by the body and boundary forces $\mathbf{f}$ and $\mathbf{b}$. The unknowns $\mathbf{u}$ and $\mathbf{p}$ are columns containing the velocity and pressure in the interpolation points. The incompressibility constraint is discretized with a penalty function method (Cuvelier *et al.*, 1986). The balance of mass is perturbed with a small parameter $\epsilon$ times the pressure:

$$\mathbf{L}\mathbf{v} = \epsilon\mathbf{M}_p\mathbf{p}. \tag{3.27}$$

The matrix $\mathbf{M}_p$ is called the pressure mass matrix. The penalty parameter $\epsilon$ must be chosen such that $\epsilon p = \mathcal{O}(10^{-6})$. By substituting equation (3.27) into equation (3.26a) the pressure is eliminated from the momentum balance by which means the momentum equations are no longer coupled with the continuity equation. Hence, the velocity is considered as the unknown and the pressure can be calculated afterwards. The penalty function method reads:

$$\mathbf{M}\frac{\partial \mathbf{v}}{\partial t} + [\mathbf{S}(\mathbf{v}) + \frac{1}{\epsilon}\mathbf{L}^T\mathbf{M}_p^{-1}\mathbf{L}]\mathbf{v} = \mathbf{f} + \mathbf{b}, \tag{3.28a}$$

$$\mathbf{p} = \frac{1}{\epsilon}\mathbf{M}_p^{-1}\mathbf{L}\mathbf{v}. \tag{3.28b}$$

The time integration is performed with the two-step $\theta$-method already described in section 3.2.3 . The first step is given by:

$$[\frac{1}{\theta\Delta t}\mathbf{M} + \mathbf{S}(\mathbf{v}_n) + \frac{1}{\epsilon}\mathbf{L}^T\mathbf{M}_p^{-1}\mathbf{L}]\mathbf{v}_{n+\theta} = \frac{1}{\theta\Delta t}\mathbf{M}\mathbf{v}_n + \mathbf{f}_{n+\theta} + \mathbf{b}_{n+\theta},$$
$$\tag{3.29a}$$

$$\mathbf{p}_{n+\theta} = \frac{1}{\epsilon}\mathbf{M}_p^{-1}\mathbf{L}\mathbf{v}_{n+\theta}. \tag{3.29b}$$

The extrapolation step is performed according to equation (3.21). It should be noted that in the case of time-dependent boundary conditions, they have to be prescribed at the time level $t_{n+\theta}$.

In the case of generalized Newtonian fluid behaviour, a linearization of the stress must be applied. For values of the power-law index of $0 < n < 1$ Picard iteration (successive substitution) can be used.

For the solution of the particle tracking problem, the Streamline Upwind Petrov Galerkin finite element method is applied using the same mesh as in the Stokes problem. The time integration is carried out with an Euler implicit scheme ($\theta = 1$).

### 3.3.2    Piston driven flow

The geometry for the piston driven flow problem is given in figure 3.3. The boundary conditions that define the piston driven flow problem (axi-
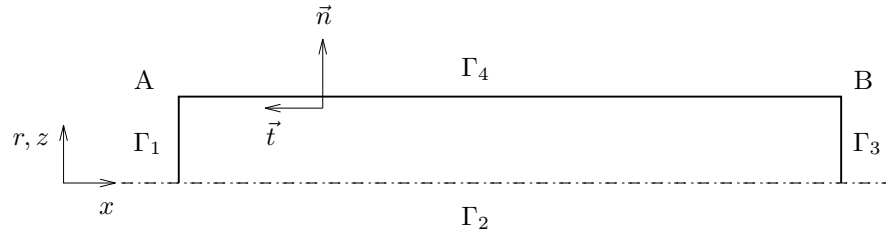


Figure 3.3: Boundaries of cavity flow problems

symmetric) are:

$$
\begin{aligned}
\vec{v} &= \vec{0} & \text{on } \Gamma_1 \\
(\vec{v} \cdot \vec{n}) &= 0 & \text{on } \Gamma_2 \\
\vec{v} &= \vec{0} & \text{on } \Gamma_3 \\
\vec{v} &= \vec{v}_0 & \text{on } \Gamma_4.
\end{aligned}
\tag{3.30}
$$

Instead of moving the pistons, the cylinder is moved with $\vec{v}_0 = [-V_w \quad 0]^T$ while the pistons are kept fixed.

In the point A and B the boundary conditions are in conflict. The points could be considered as a regular wall points or as belonging to the piston. Following Vos *et al.* (1991), the point at the driving piston (B) is considered to be part of the wall while at the driven piston (point A) some leakage is introduced by assigning the point to the piston. However, when applying proper mesh refinement in this point, the leakage will not influence the overal flow kinematics.

### 3.3.3    Piston driven contraction flow

This flow situation can be seen as a simplified version of the problem of emptying an accumulator into a mould, like applied in transfer moulding processes. The flow domain is shown in figure 3.4 (only one half is considered because of symmetry).

For this problem the flow domain changes in time. A possible way of solving this problem is to remesh the flow domain every time step with e.g. a compression-expansion scheme as advocated by Ding *et al.* (1990). In this scheme the mesh is compressed in front of the driving piston and expanded in the region in between the contraction and the driven piston. To circumvent the problem of remeshing every time step, the fixed domain method is employed. As explained in this method the pistons are represented by an artificial high viscosity material that slips at the walls. The shaded regions
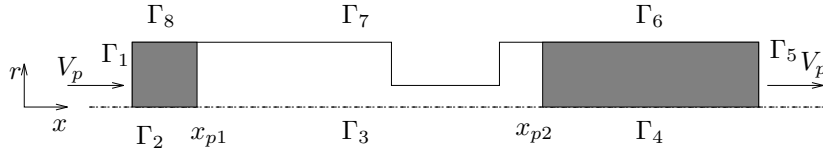


Figure 3.4: Piston driven flow through a contraction: flow domain

represent the pistons which move synchronously with the velocity $V_p$. The viscosity of the piston material is chosen a factor $10^3$ higher than the polymer viscosity. At the entrance boundary $\Gamma_1$ and the exit boundary $\Gamma_5$ the material is supposed to flow continuously with the same flow rate to take care of mass conservation. The interface positions are tracked by the label field initially defined as the axial coordinate $x$. Material with $x \leq x_{p1}$ and $x \geq x_{p2}$ is defined as piston material (steel). Obviously, the mesh has to be large enough to represent the total area that will be occupied by the melt during the experiment. The boundary conditions for this problem are given by:

$$
\begin{aligned}
\vec{v} &= \vec{v}_0 & \text{on } \Gamma_1, \\
\vec{v} &= \vec{v}_0 & \text{on } \Gamma_2, \\
(\vec{v} \cdot \vec{n}) &= 0 & \text{on } \Gamma_3, \\
\vec{v} &= \vec{v}_0 & \text{on } \Gamma_4, \\
\vec{v} &= \vec{v}_0 & \text{on } \Gamma_5, \\
\vec{v} &= \vec{v}_0 & \text{on } \Gamma_6, \\
\vec{v} &= \vec{0} & \text{on } \Gamma_7, \\
\vec{v} &= \vec{v}_0 & \text{on } \Gamma_8,
\end{aligned}
\tag{3.31}
$$

with $\vec{v}_0 = [V_p \ \ 0]^T$. Note that the boundaries $\Gamma_2$, $\Gamma_3$, $\Gamma_4$, $\Gamma_6$, $\Gamma_7$, and $\Gamma_8$ change every time step.

The interface conditions, at the wall as well as in the fluid, can be dealt with in several ways. Numerical studies (Oosterling, 1994) revealed that the viscosity jump can best be approximated by a linear interpolation within the biquadratic element. For the stick/slip transition at the wall the appoximation used is dependent of the position on the interface within the element.

When the interface is situated between the first vertex node and the midside node of the element, the boundary condition at these points are prescribed equal to the piston velocity $\vec{v}_0$ whereas a zero velocity is prescribed at the other vertex node at the wall. In the case that the piston has passed the midside node, in all three nodes of the element which are situated along the wall, a piston velocity is prescribed. To avoid a negative velocity in the integration points of the adjacent downstream element, at the midside node of that element a velocity value is assigned such that the interpolation polynomial remains positive within the element.

For this problem, two possible ways of tracking the interface can be applied. First, the interface can be determined by using particle identities as material markers. A second, less general, way is to calculate the exact positions of the interface using the (known) piston velocities. The latter method appeared to give the best results (see Oosterling, 1994) when combined with a label correction elucidated in the following. In the more general approach, the interface, especially at the driving piston, starts to deform and due to the interaction between the label field and the velocity field, the deformation grows with larger piston displacements. Application of a higher viscosity does not give the desired improvement and, moreover, results in a decreasing accuracy, since the penalty parameter ($\epsilon < \mathcal{O}(10^{-12})$ reaches the machine accuracy. Since the identity labels are employed for visualization of the deformation patterns in the fluid as well as the piston interfaces, a correction of the label field at the driving piston proved to be necessary. The label values in the regions occupied by the driving piston are updated every time step with their exact values. In this way, the interface remained straight and did not influence the deformation pattern in the fluid.

## 3.4   Conclusions

The equations derived in Chapter 2 are discretized in both space and time and the appropriate boundary conditions are defined. Splitting of the convection operator from the equations is applied to be able of calculating the convective transport with a suitable solution method. The balance of mass is satisfied locally in the $2\frac{1}{2}$D approach, by introducing a special treatment of flow splittings. The interfaces that occur in the mould filling simulations can be modelled with either a local remeshing technique or with a jump of the material properties at the interfaces. The latter technique requires the material distributions to be known in the flow domain, which can be established with particle tracking. The piston driven contraction flow is modelled using the fixed domain approach.

# Chapter 4

# Material characterization

## 4.1  Introduction

In this chapter the material properties of the three polymers, polystyrene (PS, Styron 678E from DOW Chemical), acrylonitrile-butadiene-styrene (ABS, Ronfalin FX-50 from DSM), and polyamide (PA66, Zytel 101 L NC-10 from DuPont), are presented and appropriate model parameters are determined. Since the rheological behaviour of a polymer melt has a significant influence on the deformation patterns in the flow situations investigated, the emphasis is put on the determination of the rheological (model) parameters.

## 4.2  Rheological characterization

The rheological data were measured using small amplitude oscillatory shear experiments on a Rheometrics Dynamic Spectrometer RDS-II using the parallel plate geometry. In these type of experiments, a shear strain expressed by

$$\gamma = \gamma_0 \cos(\omega t) = \gamma_0 \, \Re(e^{i\omega t}) \tag{4.1}$$

is imposed upon the sample, where $\gamma_0$ is the amplitude of the oscillation and $i^2 = -1$ in the complex representation. The responding shear stress $\tau$ will be sinusoidal with the frequency $\omega$, but with a different amplitude $\tau_0$ and phase shift $\delta$:

$$\tau = \tau_0 \sin(\omega t + \delta) = \tau_0 \, \Im(e^{i(\omega t + \delta)}). \tag{4.2}$$

The amplitude of the stress $\tau_0$ can be written as $\gamma_0 G_d$ where $G_d$ is the amplitude of the complex shear modulus $G^*$. The dynamic modulus $G_d$ and the

45

loss angle $\delta$ are defined by

$$G_d = \sqrt{G'^2 + G''^2}, \qquad \tan\delta = \frac{G''}{G'} \tag{4.3}$$

where the storage modulus $G'$ and the loss modulus $G''$ are the real and imaginary part of $G^*$ respectively. Introducing a complex viscosity $\eta^*$ defined by

$$\eta^* = -\frac{i}{\omega}G^* = \eta' - i\,\eta'', \qquad \eta' = \frac{G''}{\omega}, \qquad \eta'' = \frac{G'}{\omega}, \tag{4.4}$$

the dynamic data can be converted to a flow curve by employing the empirical Cox-Merz rule:

$$\eta(\dot{\gamma}) = \eta_d(\omega)|_{\omega=\dot{\gamma}}, \qquad \eta_d = \sqrt{\eta'^2 + \eta''^2} \tag{4.5}$$

which states that the steady state shear viscosity at a certain shear rate equals the dynamic viscosity $\eta_d$ at an angular frequency equal to the shear rate.

Using the RDS-II apparatus, the frequency range that can be imposed on the sample is $10^{-1} \leq \omega \leq 500$ $rad/s$. However, the frequency can be extended over many decades by employing the time-temperature superposition principle. Assuming thermo-rheologically simple material behaviour, the measured isothermal data ($G_d$ and $\delta$) may be shifted onto a single mastercurve. Since the loss angle $\delta$ is not influenced by the temperature, and therefore does not need a vertical shift, the horizontal shift factors $a_T$ can be determined properly using $\delta(\omega)$. Using the shift factors thus obtained to shift the dynamic modulus horizontally, an additional vertical shift factor $b_T$ can then be determined by shifting the modulus vertically to form a mastercurve. In this way, both shift factors are determined independently. The mastercurves can be expressed as:

$$\delta(\omega a_T, T_0) = \delta(\omega, T) \tag{4.6}$$

$$G_d(\omega a_T, T_0) = \frac{1}{b_T}G_d(\omega, T) \tag{4.7}$$

with the horizontal shift factor defined as $a_T = a_T(T, T_0)$ and analogously $b_T = b_T(T, T_0)$. For amorphous polymers the horizontal shift factors are usually fitted with the WLF-equation (Ferry, 1980):

$$^{10}\log a_T(T, T_0) = \frac{-a_1(T - T_0)}{a_2 + T - T_0} \tag{4.8}$$

and sometimes (e.g. close to and below $T_g$) with an Arhenius type of equation:

$$\ln a_T(T, T_0) = \frac{E_A}{R_G}(\frac{1}{T} - \frac{1}{T_0}) \tag{4.9}$$

where $E_A$ is the activation energy and $R_G$ the universal gas constant. Note that in the 7-constant Cross model the shift factor is modelled by

$$\ln a_T(T, T_0) = \frac{-c_1(T - T_0)}{c_2 + T - T_0} \tag{4.10}$$

with $c_1 = a_1 \ln^{-1}(10)$ and $a_2 = c_2$. The vertical shift factors represent the influence of the density on the modulus and might be modelled by a temperature-density correction:

$$b_T(T, T_0) = \frac{\rho_0 T_0}{\rho T} \tag{4.11}$$

where the index 0 represents the values at the reference temperature $T_0$ and the density $\rho$ can be evaluated from the $p\nu T$-data.

### 4.2.1 Polystyrene

The sample dimensions for the parallel plate geometry are: $\emptyset 25 \times 1.5\ mm$. The data are measured as a function of the frequency ($\omega \in [10^{-1}, 500]\ rad/s$) at different temperatures between $393\ K$ and $538\ K$. The isothermal curves are shifted onto a single mastercurve at a reference temperature of $T_0 = 462\ K$. The resulting curves for the loss angle and dynamic modulus of PS are shown in figure 4.1 and 4.2 respectively. The horizontal shift factors are plotted as a function of temperature in figure 4.3a which also shows the WLF-fit and its parameters. The vertical shift factors and the temperature-density correction are given in figure 4.3b.

From the dynamic data, the viscosity is calculated and fitted with a Cross model equation (2.7). The zero-shear rate viscosity $\eta_0$ is chosen to be a function of the pressure and temperature:

$$\eta_0(p, T) = H e^{\frac{-c_1(T - T^*)}{c_2^* + T - T^*}}, \qquad T^* = T_0 + S_p\, p, \qquad c_2^* = c_2 + S_p\, p. \tag{4.12}$$

The experimental data and fit are plotted in figure 4.4 for three different temperatures. The parameters used in the 7-constant Cross model are listed in table 4.1. The viscosity curve can roughly be divided into two separate regions: a plateau zone revealing Newtonian behaviour and a shear thinning zone. For high shear rates the slope of the curve is not constant but the
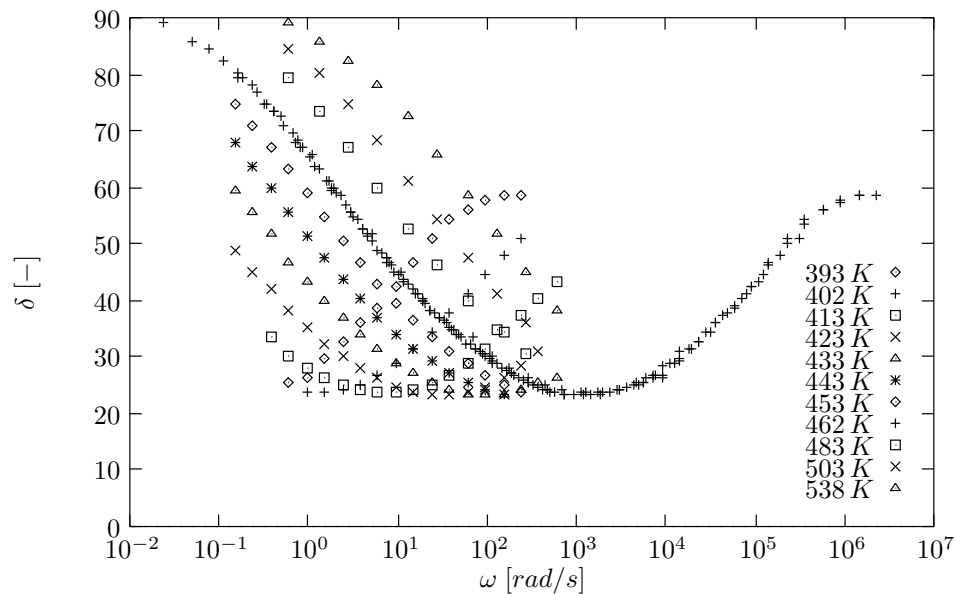
Figure 4.1: Loss angle as a function of angular frequency at different temperatures and the mastercurve at $T_0 = 462\ K$ for PS
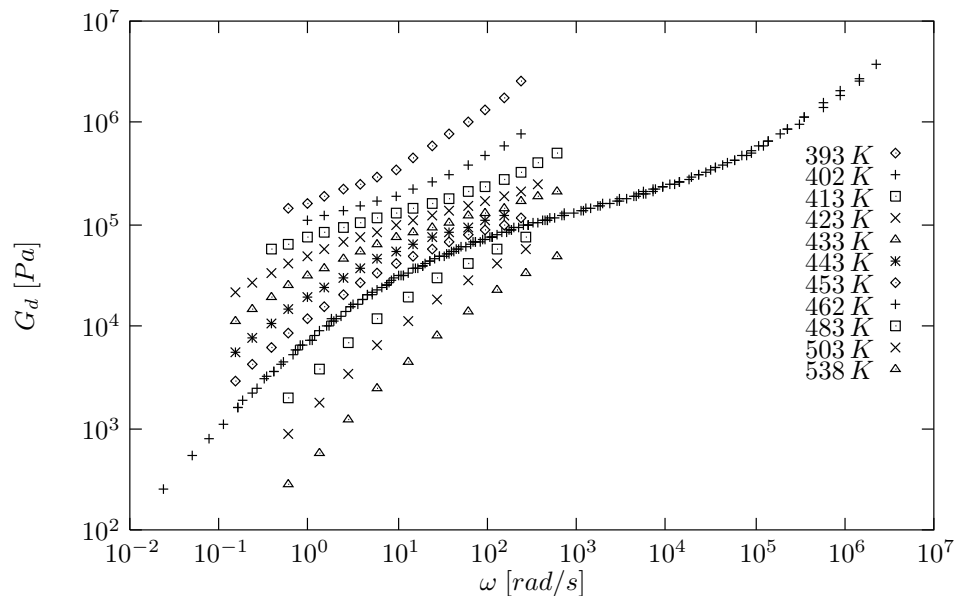


Figure 4.2: Dynamic modulus as a function of angular frequency at different temperatures and the mastercurve at $T_0 = 462\ K$ for PS

viscosity tends to reach a second plateau. The Cross model employed does not take this behaviour into account.

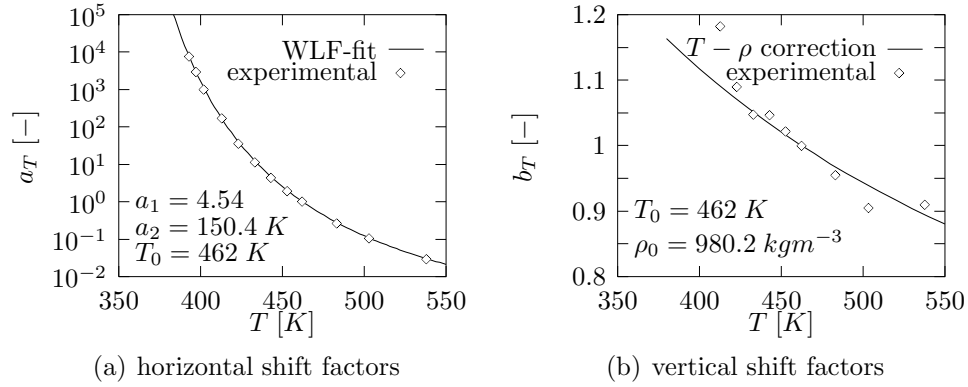(a) horizontal shift factors      (b) vertical shift factors

Figure 4.3: Shift factors against temperature for PS

For PS the glass transition temperature is considered to be pressure dependent:

$$T_g = T_{g0} + S_p\, p, \qquad\qquad (4.13)$$

where $T_{g0} = 373\ K$ and $S_p = 5.1 \cdot 10^{-7}\ K/Pa$. In the numerical simulations the $T_g$ is used as the no-flow temperature.



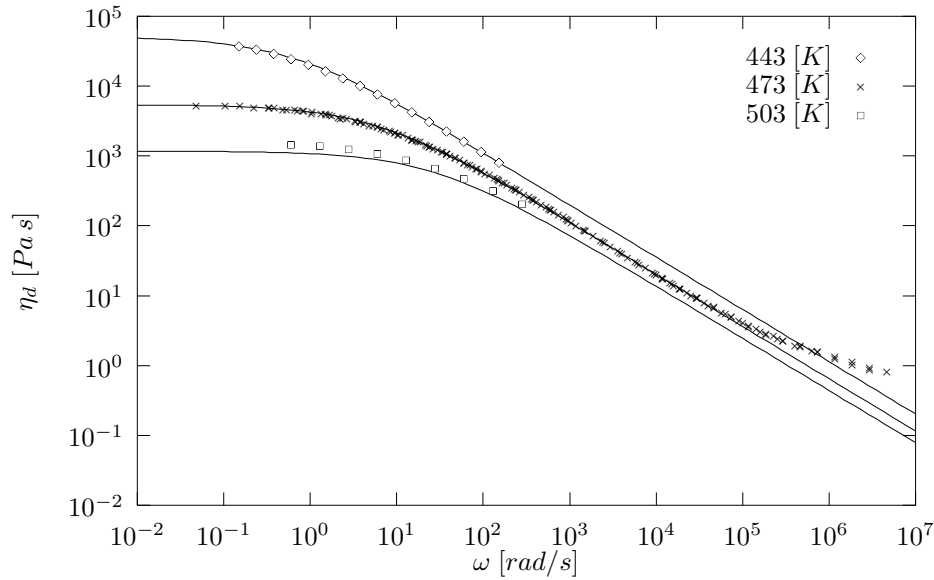Figure 4.4: Viscosity curve of PS at three different temperatures (solid lines: fit, symbols: measured data)

| PS, Styron 678E | | |
|---|---|---|
| $n$ | | 0.2520 |
| $\tau^*$ | $Pa$ | $3.080 \cdot 10^4$ |
| $H$ | $Pas$ | $4.76 \cdot 10^{10}$ |
| $T_0$ | $K$ | 373 |
| $c_1$ | | 25.74 |
| $c_2$ | $K$ | 61.06 |
| $S_p$ | $K/Pa$ | $5.1 \cdot 10^{-7}$ |

Table 4.1: Parameters in 7-constant Cross model

## 4.2.2   Acrylontrile-butadiene-styrene

The (dynamic) shear data for ABS are determined following the same proce-dure as described before for PS. The mastercurves at a reference temperature of $T = 473\ K$ are constructed using isothermal curves covering the temper-ature range $T \in [433, 523]\ K$. Figure 4.5 shows the determined horizontal shift factors and the fitted WLF-parameters. The vertical shift factors $b_T$ are taken equal to 1. The results for the loss angle and the dynamic modulus are shown in figure 4.6 and 4.7 respectively.
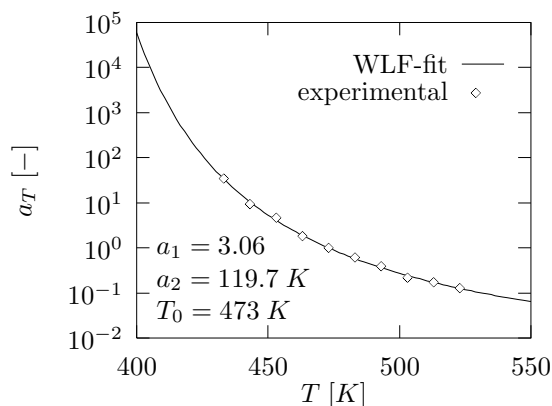


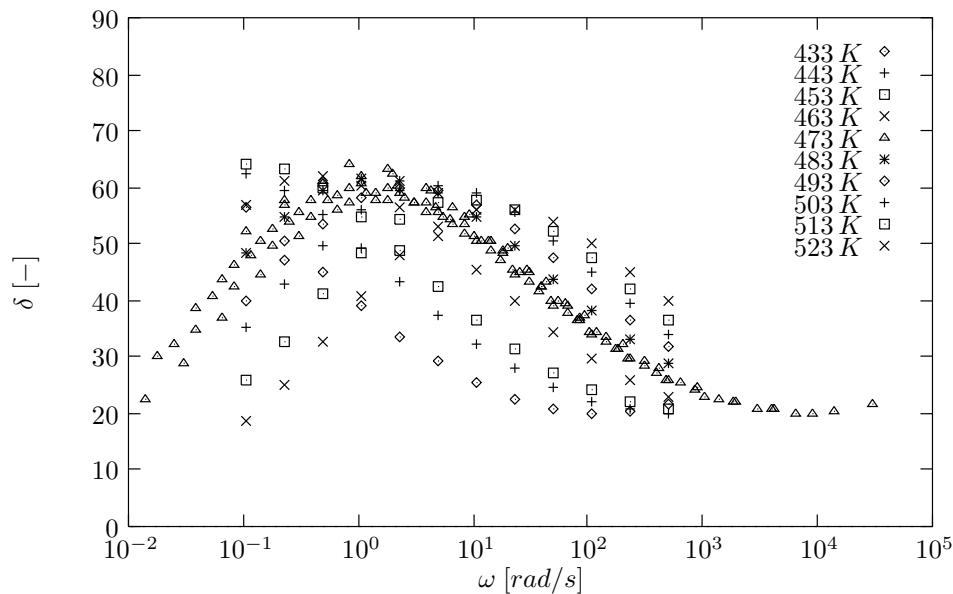Figure 4.5: Horizontal shift factor against temperature for ABS

Figure 4.6: Loss angle as a function of angular frequency at different temperatures and the mastercurve at $T_0 = 473\ K$ for ABS
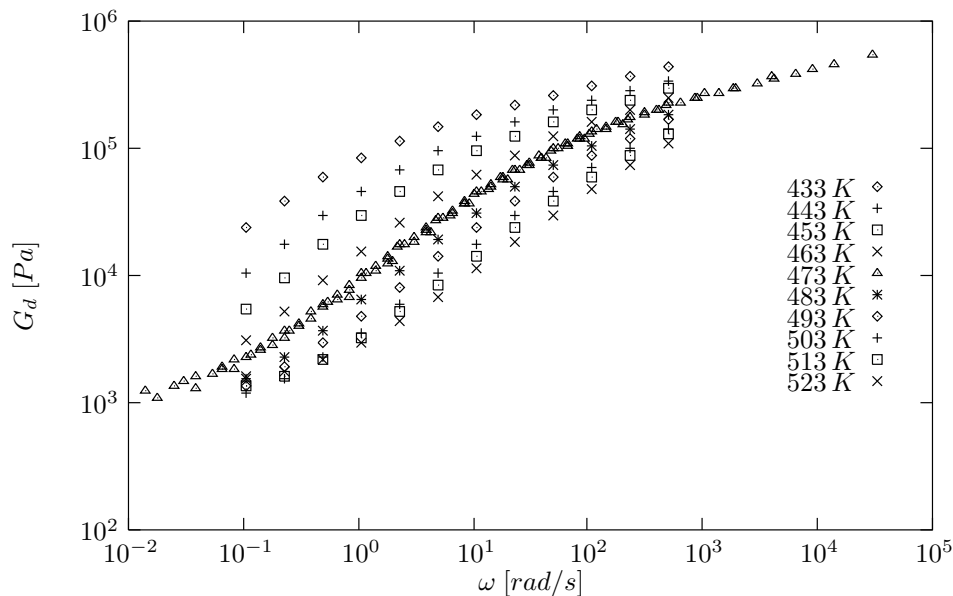


Figure 4.7: Dynamic modulus as a function of angular frequency at different temperatures and the mastercurve at $T_0 = 473\ K$ for ABS

The dynamic viscosity is plotted for three different temperatures in figure 4.8. From this figure it can be deduced that ABS does not expose a Newtonian plateau region, but the viscosity rises with a decreasing frequency.
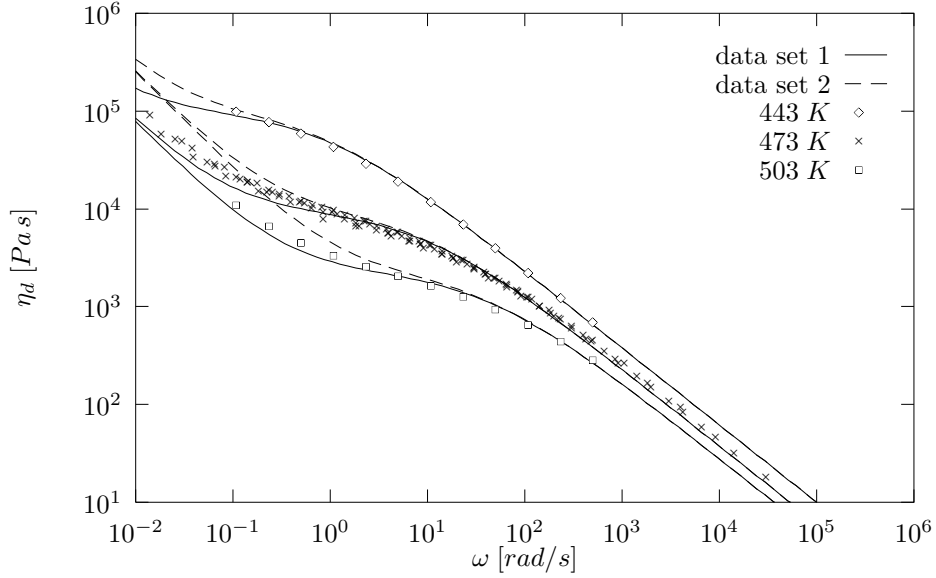
Figure 4.8: Viscosity curve of ABS at three different temperatures (solid lines: fit, symbols: measured data)

This observation points to the existence of a yield stress. These findings are in agreement with those of Münstedt (1981) who showed that in the low shear rate region the viscosity can be influenced considerably by increasing the rubber content of ABS. The presence of a yield stress can be shown more convincing when plotting the viscosity as a function of the shear stress $\tau$ (see figure 4.9). To model the specific shear properties of this ABS, the Cross model is not suitable unless it is extended to incorporate a Bingham-like behaviour. In a paper on the existence and nature of a yield stress Evans (1992) proposed a generalization of the Cross model:

$$\frac{\eta - \eta_\infty}{\eta_0 - \eta_\infty} = \frac{1 + k_2\dot{\gamma}^{n_2}}{1 + k_1\dot{\gamma}^{n_1}}. \tag{4.14}$$

In order to incorporate a temperature independent yield stress but temperature dependent viscosity, equation (4.14) is extended and rewritten in the following form:

$$\eta(T, \dot{\gamma}) = \eta_0(T)\frac{1 + (\lambda_2\dot{\gamma})^{-1}}{1 + (\lambda_1\dot{\gamma})^{n_1}}, \tag{4.15}$$

with

$$\eta_0(T) = He^{\frac{-c_1(T-T_0)}{c_2+T-T_0}}, \quad \lambda_j(T) = B_je^{\frac{-c_1(T-T_0)}{c_2+T-T_0}} \quad (j = 1, 2). \tag{4.16}$$
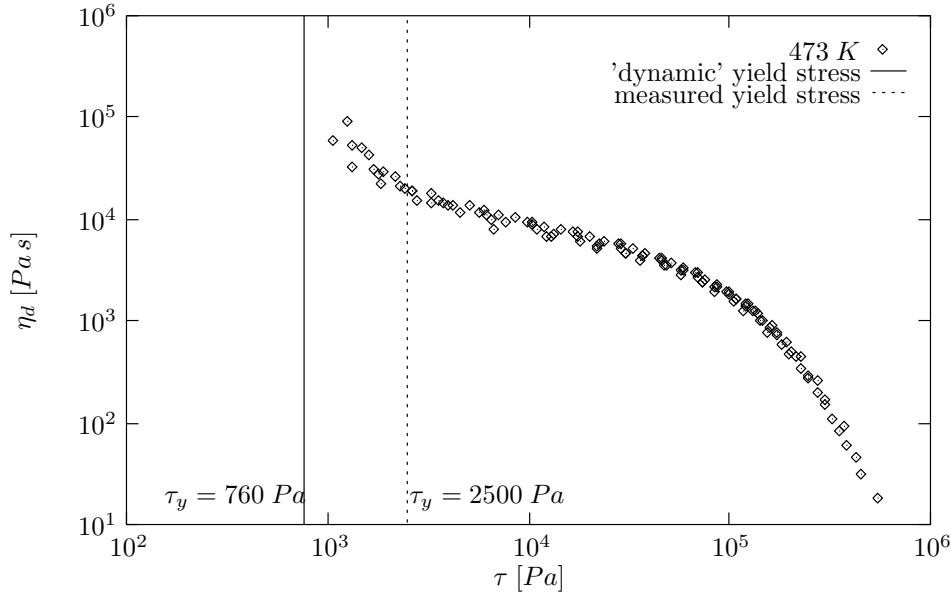
Figure 4.9: Viscosity as a function of shear stress for ABS at $T = 473\ K$

For $\dot{\gamma} \to 0$ equation (4.15) reduces to a model for a Bingham liquid

$$\eta(T, \dot{\gamma}) = \eta_0(T) + \tau_y \dot{\gamma}^{-1}, \quad \text{with } \tau_y = \frac{\eta_0(T)}{\lambda_2}. \tag{4.17}$$

Equation (4.17) reveals that the yield stress $\tau_y = H/B_2$ is temperature independent. The results of the fit on the dynamic viscosity data are shown in figure 4.8. From this fit the yield stress value can be derived and equals $\tau_y = 760\ Pa$. This value is considerably lower than the value reported by Münstedt (1981), who found that $\tau_y = 3 \cdot 10^3 - 10^4\ Pa$ for ABS types with a rubber contents between 30% and 40% which is the case for the Ronfalin FX-50 grade. However, a material with a yield stress may not be expected to be thermo-rheologically simple for low frequencies or shear rates. Therefore a yield stress determined from dynamic data is unreliable. Additional measurements with a constant-stress rheometer at DSM Research yielded a yield stress with a value $1875 \le \tau_y \le 3125\ Pa$. From these results the averaged value of $\tau_y = 2500\ Pa$ is taken for further investigation. The viscosity curve calculated with the latter value is also plotted in figure 4.8. All final parameter values for the generalized Cross model used for ABS are given in table 4.2. The data set 1 is the result of the fit of the dynamic data, whereas data set 2 incorporates the measured yield stress.

| ABS, Ronfalin FX-50 | | | |
|---|---|---|---|
| | | set 1 | set 2 |
| $n_1$ | | 0.79 | 0.79 |
| $H$ | $Pas$ | $9.5 \cdot 10^3$ | $9.5 \cdot 10^3$ |
| $T_0$ | $K$ | 473 | 473 |
| $c_1$ | | 7.04 | 7.04 |
| $c_2$ | $K$ | 119.7 | 119.7 |
| $B_1$ | $s$ | 0.11 | 0.11 |
| $B_2$ | $s$ | 12.5 | 3.8 |

Table 4.2: Parameters in generalized Cross model

### 4.2.3   Polyamide

The data for polyamide are taken from (Peters *et al.*, 1994). The viscosity is modelled using a Truncated Power Law model:

$$\eta(T, \dot{\gamma}) = \begin{cases} m_0 e^{\frac{-\beta T}{n}} \phi^{1-n} & \text{for } \dot{\gamma} \leq \frac{1}{\phi} e^{\frac{\beta T}{n}}, \\ m_0 e^{-\beta T} \dot{\gamma}^{n-1} & \text{for } \dot{\gamma} > \frac{1}{\phi} e^{\frac{\beta T}{n}}. \end{cases} \tag{4.18}$$

The viscosity as a function of shear rate for three different temperatures is shown in figure 4.10.
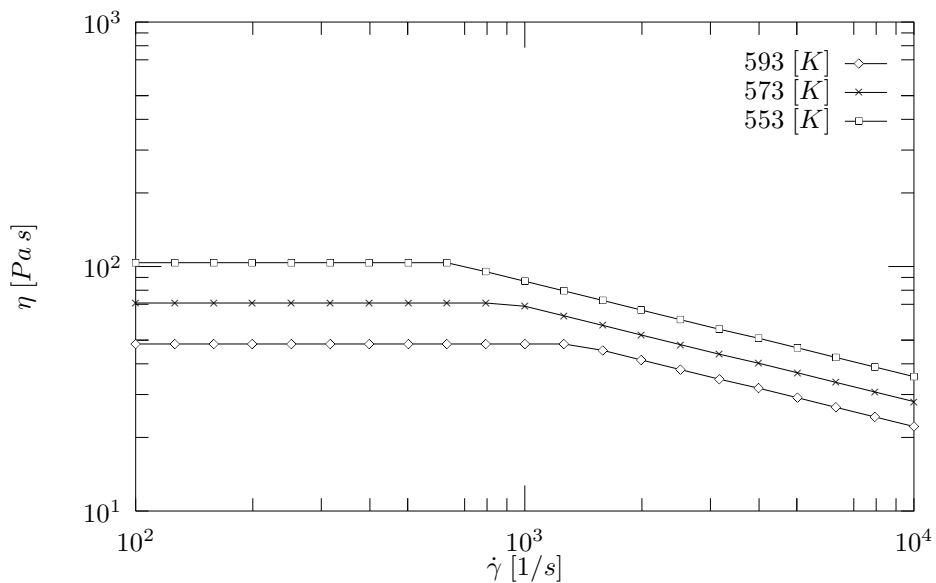


Figure 4.10: Viscosity as a function of shear rate and temperature for PA66

The model parameters are listed in table 4.3.

| PA66, Zytel 101 L NC-10 | | |
|---|---|---|
| $n$ | | 0.61 |
| $m_0$ | $Pa\,s$ | $3.455 \cdot 10^4$ |
| $\phi$ | $s$ | 0.347 |
| $\beta$ | $K^{-1}$ | $1.175 \cdot 10^{-2}$ |

Table 4.3: Parameters truncated power law model

## 4.3   $p\nu T$-data and thermal properties

The data for the specification of the density and the thermal properties are all taken from literature. Since the ABS material is not used in a simulation of the injection moulding proces, the $p\nu T$-data need not to be modelled and a constant value of $\rho = 945 \; kgm^{-3}$ (at $T = 473 \; K$) is taken instead.

### 4.3.1   Polystyrene

The $p\nu T$-behaviour for the PS material was measured by Flaman (1990). The data are fitted using the Tait equation (2.9). The model parameters are given in table 4.4.

| PS, Styron 678E | | melt | glass |
|---|---|---|---|
| $a_0$ | $m^3/kg$ | $9.72 \cdot 10^{-4}$ | $9.72 \cdot 10^{-4}$ |
| $a_1$ | $m^3/(kgK)$ | $5.44 \cdot 10^{-7}$ | $2.24 \cdot 10^{-7}$ |
| $B_0$ | $Pa$ | $2.53 \cdot 10^8$ | $3.53 \cdot 10^8$ |
| $B_1$ | $K^{-1}$ | $4.08 \cdot 10^{-3}$ | $3.00 \cdot 10^{-3}$ |
| $T_g(0)$ | $K$ | 373 | |
| $s$ | $K/Pa$ | $5.1 \cdot 10^{-7}$ | |

Table 4.4: Parameters in Tait-equation

The thermal conductivity is taken to be constant in the solid as well as in the melt with a value of $\lambda = 0.17 \; W/(mK)$ (see Flaman, 1990, chapter 4). The specific heat capacity $c_p$ is modelled using constant values in either the molten or solid phase. For $T \leq T_g$ the value is $c_p = 1785 \; J/(kg\,K)$ and $c_p = 2289 \; J/(kg\,K)$ for temperatures above $T_g$.

### 4.3.2   Polyamide

The specifications of the nylon were again taken from (Peters *et al.*, 1994). Due to lack of more precise data of the density and the thermal properties, constant values are assumed in either the molten or solid phase. The parameter values are summarized in table 4.5.

| PA66, Zytel 101 L NC-10 | | melt | solid |
|---|---|---|---|
| $\rho$ | $kg\,m^{-3}$ | 950 | 1140 |
| $\lambda$ | $W/(m\,K)$ | 0.1346 | 0.27 |
| $c_p$ | $J/(kg\,K)$ | 2897 | 2432 |

Table 4.5: Specification density and thermal properties

Furthermore, a no-flow temperature of $T = 507\ K$ was used in the calculations.

## 4.4   Conclusions

Concluding this material characterization chapter we can state that PS is the most extensively described material (with steady state viscosity data fitted by the 7-constant Cross model and density data using the 6 parameter Tait equation), followed by ABS (7 parameter generalized Cross model with inclusion of a yield stress) while PA was, because of lack of own data, more roughly described (4 parameter truncated power law model and constant density). Since in this thesis we do not intend to perform visco-elastic calculations, the characterization has not been elaborated in this direction. See for a complete visco-elastic description of the PS used, e.g. Douven (1991) and/or Zoetelief (1992).

# Chapter 5

# Particle tracking: two test problems

## 5.1  Introduction

In this chapter the numerical models, especially those for particle tracking, are tested using two well-defined problems. The first problem that will be considered in section 5.2 is the flow of a generalized Newtonian fluid between two pistons advancing in a tube. In the next section the geometrical complexity of the problem is increased, resulting in the piston driven contraction flow. In these problems, the numerically and experimentally obtained deformation patterns that develop during the flow, are compared.

## 5.2  Piston driven flow

In order to validate the particle tracking capability, the test problems have to meet some demands regarding their geometrical complexity and flow characteristics. The piston driven flow problem proved to be suited for this purpose, since its geometrical complexity is low and the initial and boundary conditions are well defined while the flow is complex. Moreover, the flow geometry is in accordance with the accumulator which is designed for future use in the multi-component moulding.

### 5.2.1  Material and methods

**Experimental**

The experimental set-up used is drawn schematically in figure 5.1. A sample ($\varnothing 16 \times 54$ $mm$) containing differently coloured slices is placed between two
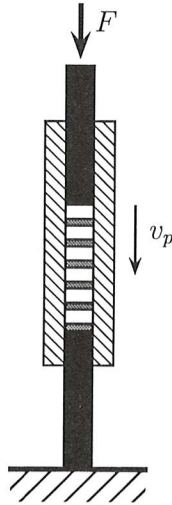
Figure 5.1: Experimental set-up piston driven flow

pistons in a heated cylinder. The lower piston is kept fixed, while the upper piston is able to move freely. A load $F$ is put on top of the upper piston to prevent the development of shrinkage holes during cooling of the sample and, moreover, to ensure contact between the piston and the polymer. After the cylinder has been heated to the required temperature, the cylinder is driven downwards with a constant rate $v_p$. By doing so, the lower piston acts like a driving piston and the upper piston can be regarded as driven by the fluid. After moving the cylinder, the apparatus is cooled down and after solidification the sample can be taken out. The deformation patterns are made visible by cutting the sample along the axial plane of symmetry. The development of the deformation patterns in time is visualized by using different cylinder displacements $\Delta s$.

The experiments are carried out with polystyrene (PS) and acrylonitrile-butadiene-styrene (ABS). These materials differ in their flow behaviour at low shear rates as is described in chapter 4. PS shows Newtonian behaviour in this region whereas ABS tends towards a more complex, Bingham-like, flow behaviour. The experiments are carried out at different temperatures and cylinder velocities $v_p$. The thermal soak-time was 20 minutes after the set-point of the temperature has been reached. Two different sets of tests are performed. First, tests with a sample solely consisting of coloured slices of PS or ABS are discussed. In these series also the influence of the temperature or cylinder velocity on the deformation patterns is examined. In the second

series, the samples are composed of a combination of the two materials: PS on top of ABS and the reversed configuration. The experimental conditions are summarized in table 5.1.

| no. | material | $v_p$ [mm/s] | $T$ [K] | $\Delta s$ [mm] |
|-----|----------|--------------|---------|------------------|
| 1 | PS | 1.0 | 473 | 0, 10, 20, 30, 40 |
| 2 | PS | 1.0 | 443 | 40 |
| 3 | PS | 1.0 | 503 | 40 |
| 4 | PS | 43.2 | 473 | 40 |
| 5 | ABS | 1.0 | 473 | 0, 10, 20, 30, 40 |
| 6 | ABS | 1.0 | 443 | 40 |
| 7 | ABS | 1.0 | 503 | 40 |
| 8 | ABS | 43.2 | 473 | 40 |
| 9 | PS/ABS | 1.0 | 473 | 0, 10, 20, 30, 40 |
| 10 | ABS/PS | 1.0 | 473 | 0, 10, 20, 30, 40 |

Table 5.1: Experimental conditions piston driven flow

## Numerical

The numerical simulations are performed using a finite element mesh consisting of 776 biquadratic triangular elements as is depicted in figure 5.2. The applied boundary conditions are already given in figure 3.3. Because of symmetry, only one half of the geometry is modelled. The wall ($\Gamma_4$) is moving
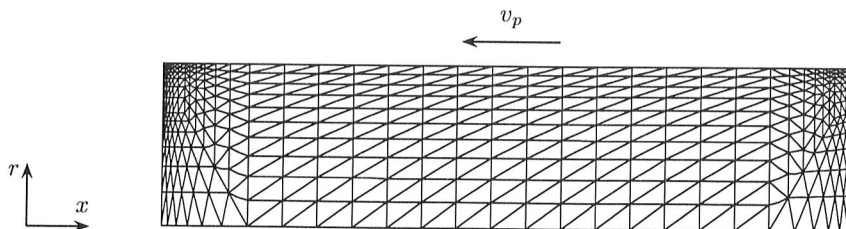


Figure 5.2: Finite element mesh piston driven flow problem

with the velocity $v_p$. The total time interval for the displacement of 40 $mm$ ($= \Delta s/v_p$) is divided into 200 timesteps. For the simulations with the samples consisting of one material only, one iteration for each time step proved to be sufficient. The combination of two materials in one sample introduce an extra non-linearity in the simulations, since the velocity is also depend

of the distribution of those two materials which is defined by the label field. In these cases, the velocity field is calculated by a Picard iteration method (successive substitution) every time step. The particle tracking problem is solved using the SUPG finite element method with the time-dependent upwind parameter (see Appendix B). The time integration is carried out with a Crank-Nicholson scheme ($\theta = 0.5$). The axial coordinates $z$ are taken as initial label field at $t = 0$. By making contour plots of that label field, in which the contours coincide with the tracer positions in the experiments, the deformation patterns are visualized and can be compared with the experimentally obtained results.

### 5.2.2   Validation

The experimentally obtained and calculated development of the deformation patterns for PS are presented in figure 5.3a and b respectively. The deformation pattern for a displacement of 0 $mm$ shows that the heating and subsequent cooling introduces considerable disturbance of the initially straight tracers. This effect can still be seen in the sample undergoing a cylinder displacement of 10 $mm$. From the displacements of 20 $mm$ or more, the fountain effect occurring at both pistons can be recognized. In the fountain region near the upper piston material elements move from the center towards the wall which results in a strong elongation of those elements close to the piston. When approaching the wall, the material acquires a reverse velocity causing continuously stretching Z-shapes. Note that these Z-shapes correspond with the V-shapes that are found in mould filling (see e.g. the discussion of Beris, 1987). At the driving piston similar behaviour can be observed, but here the material moves from the walls inwards to the center of the sample. The resulting Z-shapes now appear in the core instead of close to the wall. These observations show that in piston driven flow experiments three different regions can be distinguished: the region near the driving piston where a reverse fountain flow occurs, the fountain flow region near the driven piston and an intermediate region where an axi-symmetrical two-dimensional flow exists.

The calculated deformations reveal all the details described above. The difference that attract the attention is that the deformation in the region along the symmetry line of the sample is overpredicted for all displacements. However, the relative distance between two successive displacements $\Delta s$ of the same tracer that is situated in the 'main' flow, for example the second one from below, agree well with the experiments. Also, the position of the Z-shapes in the upper part of the domain is predicted well. Seemingly, the residence time in the reverse fountain region is underpredicted. It is raised
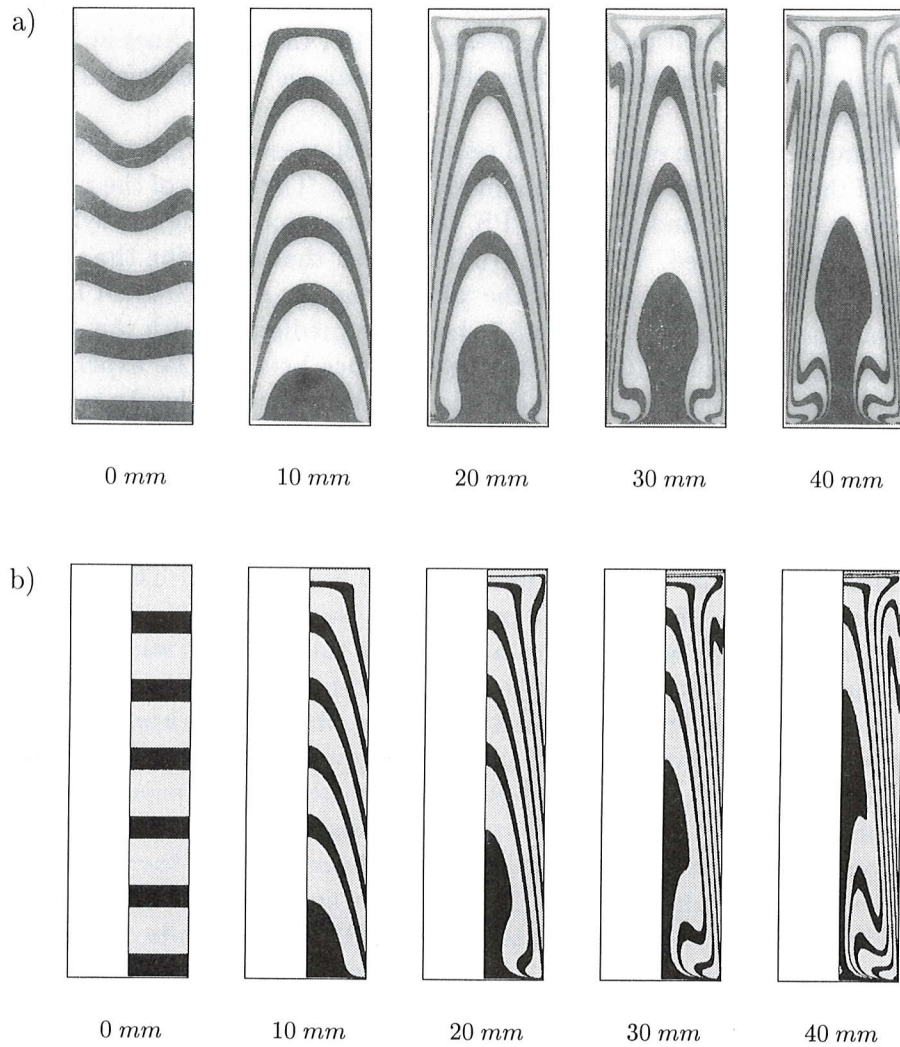
Figure 5.3: Deformation of PS for different piston displacements: a) experiments, b) calculated ($v_p = 1.0 \ mm/s$, $T = 473 \ K$)

that visco-elastic effects in the fountain flow region (may) cause this deviation.

The results for ABS (see figure 5.4a and 5.4b for the experiments and simulations using the data set 1 (table 4.2) respectively) show a similar behaviour of forming the Z-shapes. This was expected, since the the characteristic deformation patterns in the fountain regions are solely governed by the balance

of mass irrespective of the rheological behaviour of the fluid (see also Beris, 1987). In contrast with the experiments with PS, the tracer lines in the center region reveal a plug flow rather than a parabolic shaped deformation of the tracers.

Comparing to the experimental results, the flattened tracer profiles in the core of the sample are not that distinctly present. The width of the plug flow region is too small and, like with PS, the deformations along the symmetry line are overpredicted. Vos *et al.* (1991) showed that adjusting the material data, i.e. changing the value of the yield stress for ABS, resulted in a improvement of the results. Figure 5.5 shows the predictions with the material data set 2 (see table 4.2). Now the resemblance between the experimental and calculated results is remarkably good, especially up to the $\Delta s = 30\,mm$. Therefore, in the following only data set 2 will be used.

Figure 5.6a and 5.6b show, respectively, the experimentally and numerically obtained influence of the temperature and the cylinder velocity on the deformation of the tracers for PS. For the PS samples, the effect of the temperature disappears almost completely above $T = 473\ K$. The increasing temperature shifts the transition between the Newtonian plateau region and the shear-thinning region towards higher shear rates. In this way, the viscosity gradient from the core towards to wall that is still present at $T < 473\ K$ levels off to zero. The difference that can be observed between the deformations in the core of the sample is mainly governed by the shear-thinning behaviour of the PS. The experiment with the high cylinder velocity confirms this observation. In the numerical results the discrepancies in the core deformation are the same as described before, but the influence of the temperature and velocity show the same tendency as in the experiments.

The same test conditions are also used for ABS. The results can be found in figure 5.7. Compared with PS, ABS shows a different response on the variation of the temperature. Where the core deformations for PS increase with increasing temperature, for ABS the deformations decrease. This can be explained by the effect of the yield stress in ABS. Since the shear stress for a certain shear reate will increase with decreasing temperature, the region of the sample where the shear stress, governed by the local shear rate and viscosity values, does not exceed the yield stress will be smaller. An higher velocity (and thus a higher shear rate) has the same effect upon the width of the core region where the plug type deformation can be observed. As a consequence, the resulting deformation patterns become similar to those of a shear thinning liquid. This is clearly demonstrated with the sample that has undergone the higher cylinder velocity. On the other hand, with increasing temperature the yield stress becomes more important and only the flow conditions in a small layer of material near the wall is such that
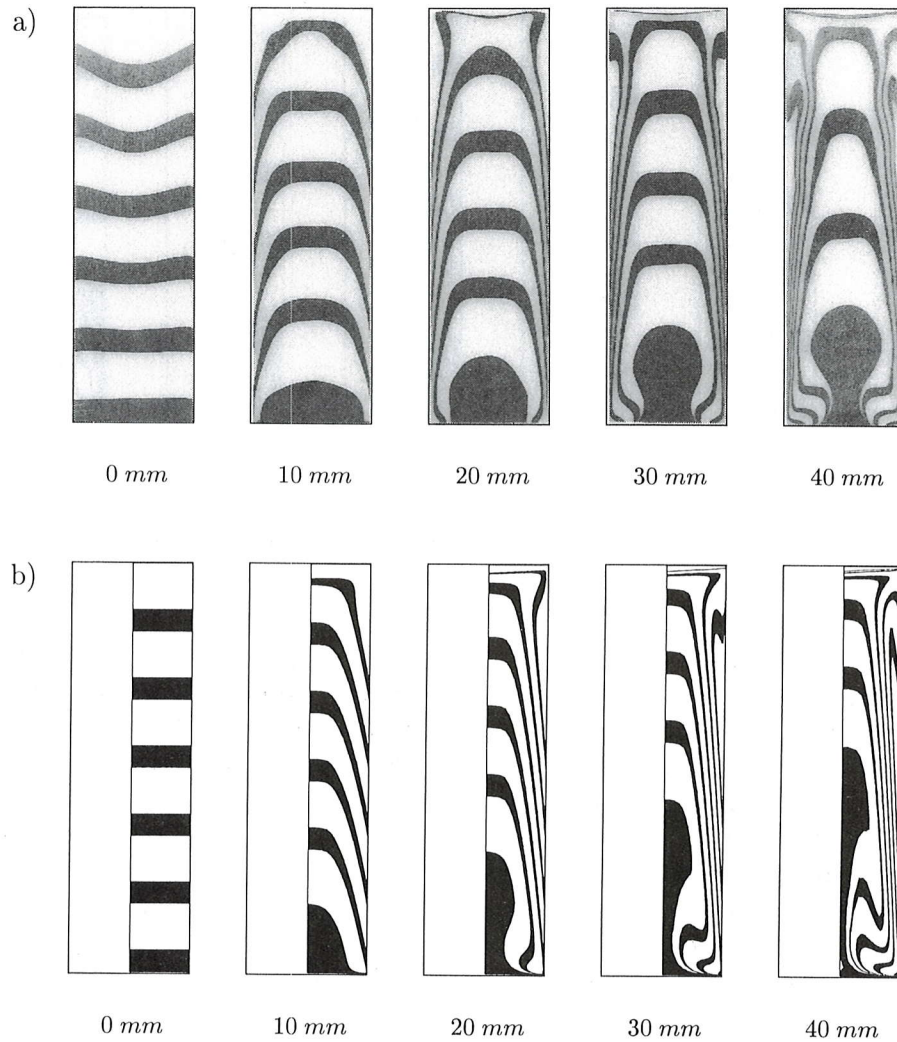
Figure 5.4: Deformation of ABS for different piston displacements: a) experiments, b) calculated ($v_p = 1.0 \ mm/s$, $T = 473 \ K$, material data set 1)

$\tau_y$ is exceeded. This explains the broadening of the plug flow region and the decreasing core deformation with increasing temperature. Again, the agreement between the experimental and calculated results is good.

The development of the deformation patterns in case that two materials are combined in one sample is shown in the figures 5.8 and 5.9. The results of the two series experiments with the material combinations differ in many aspects. With the PS material situated on top of ABS, a second reverse
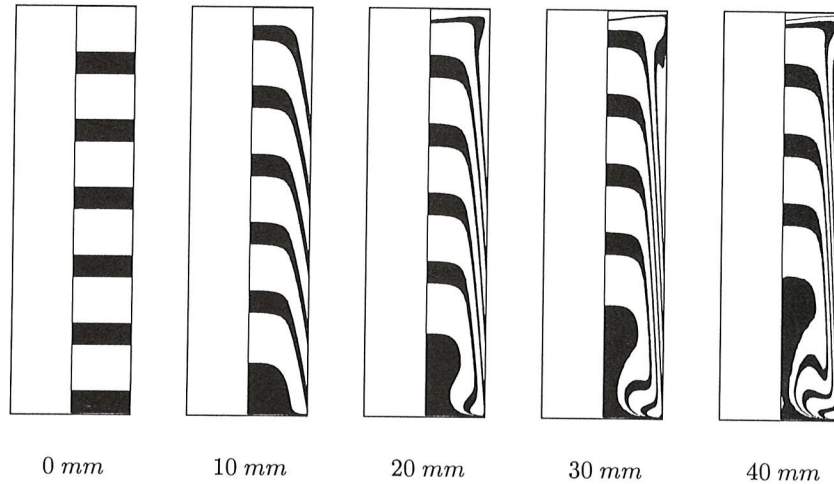
Figure 5.5: Calculated deformation of ABS for different piston displacements
($v_p = 1.0 \ mm/s$, $T = 473 \ K$, material data set 2)

fountain region at the interface of the two materials can be observed, while
in the reverse initial configuration the PS material protrudes in the ABS. In
figure 5.9a it can be seen that the core deformation is even higher than was
observed in figure 5.3a. For these series also, the resemblance between the
predicted and measured tracer deformations is remarkably good. Even the
onset of the reverse fountain region at the material interface is present in the
calculations.

From the results we can conclude that the predictive quality of the simu-
lation code (and the applied constitutive models with the measured parame-
ters) is satisfactory for the experimental conditions used. In order to attain a
better agreement between the calculated and experimentally obtained defor-
mation patterns, visco-elastic modelling of the flow should be employed and
the influence of shrinkage should be eliminated or controlled and calculated.
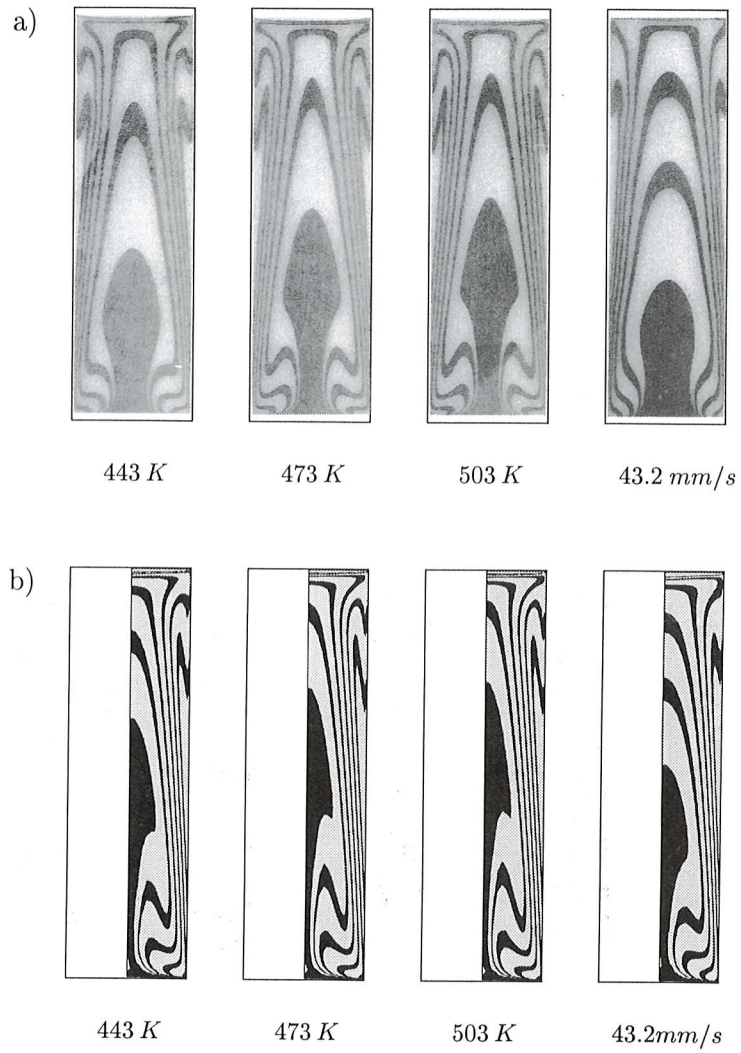
Figure 5.6: Deformation of PS for different test conditions: a) experiments, b) calculated

a)

443 *K*          473 *K*          503 *K*          43.2 *mm/s*

b)

443 *K*          473 *K*          503 *K*          43.2 *mm/s*
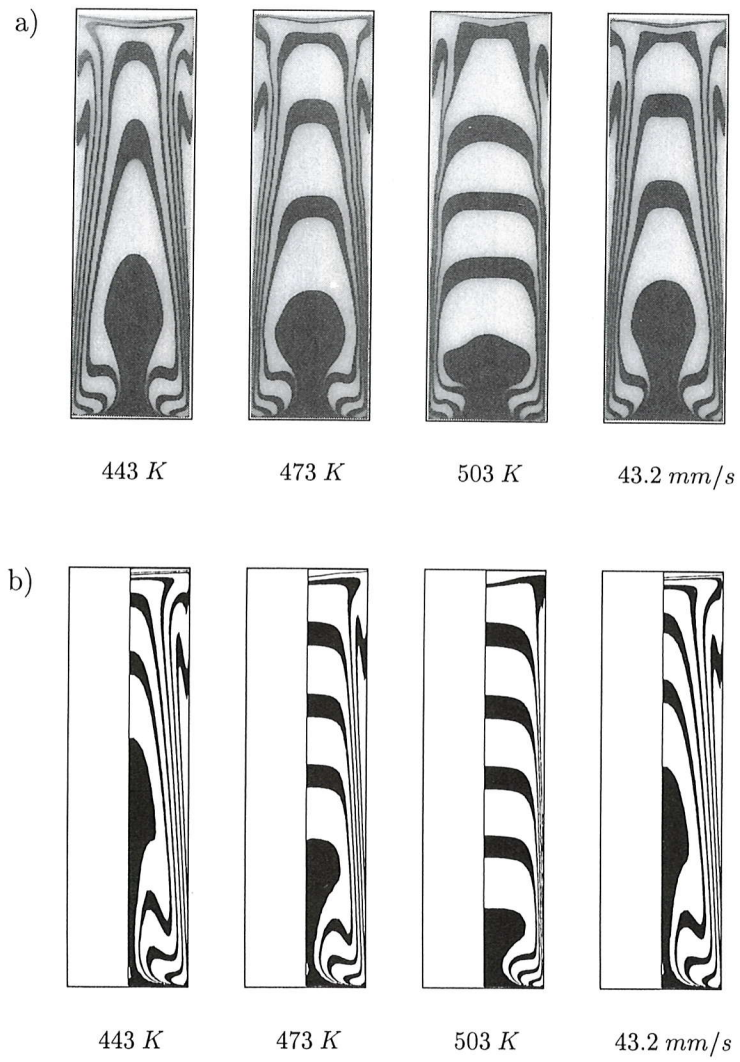
Figure 5.7: Deformation of ABS for different test conditions: a) experiments, b) calculated

a)

PS

ABS

0 *mm*        10 *mm*        20 *mm*        30 *mm*        40 *mm*

b)

PS

ABS

0 *mm*        10 *mm*        20 *mm*        30 *mm*        40 *mm*

Figure 5.8: Deformation of the combination PS/ABS for different piston displacements: a) experiments, b) calculated ($v_p = 1.0$ *mm/s*, $T = 473$ *K*)
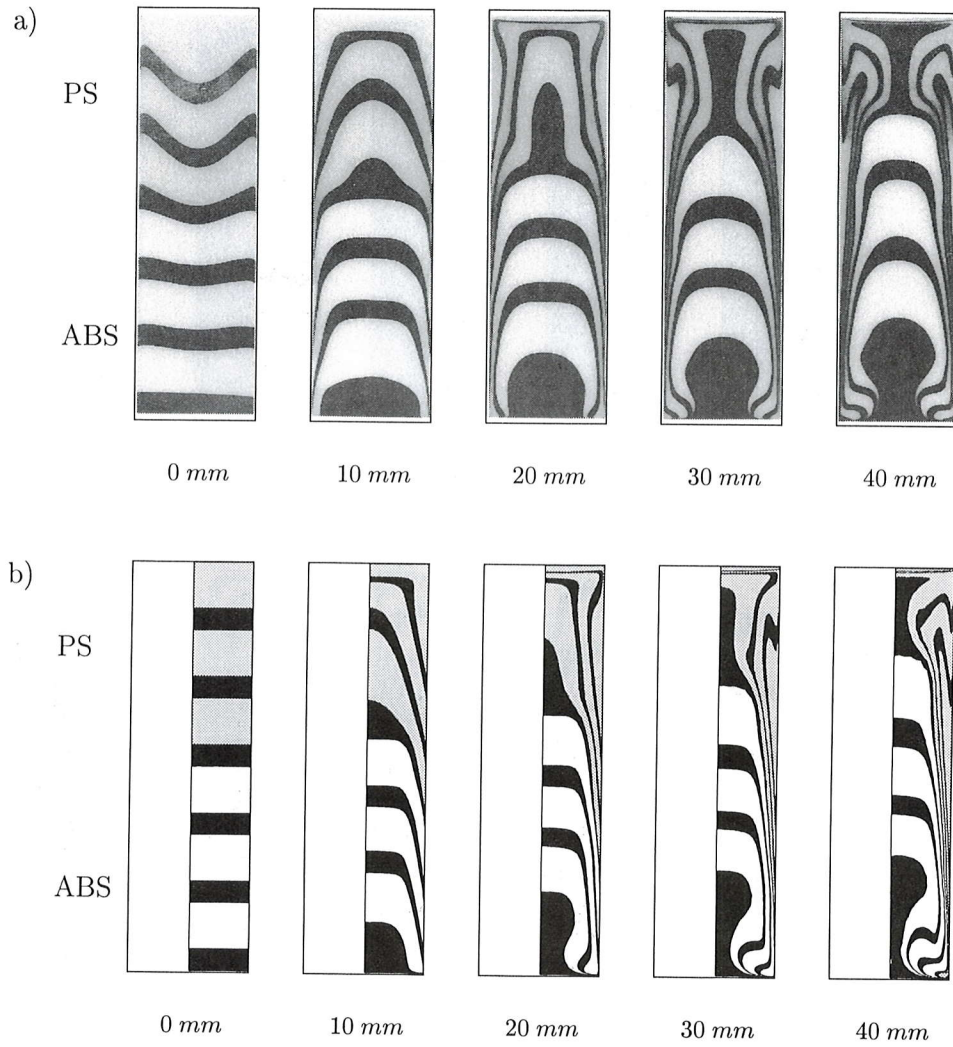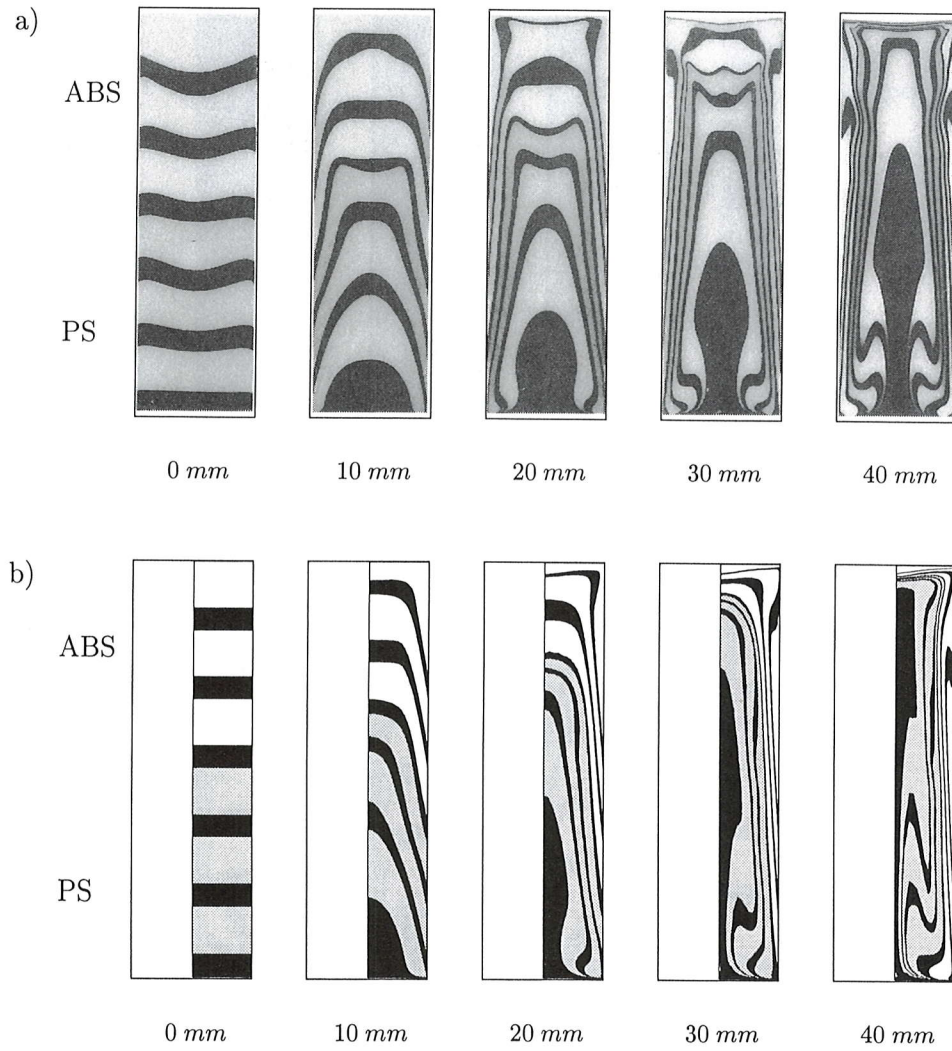
Figure 5.9: Deformation of the combination ABS/PS for different piston displacements: a) experiments, b) calculated ($v_p = 1.0\ mm/s$, $T = 473\ K$)

# 5.3   Piston driven contraction flow

In the basic design of an accumulator, the material is forced through a nozzle into the mould. The effect of such a contraction on the deformation patterns is studied with a piston driven contraction flow. These experiments are also used for validation of the fixed domain approach.

## 5.3.1   Material and methods

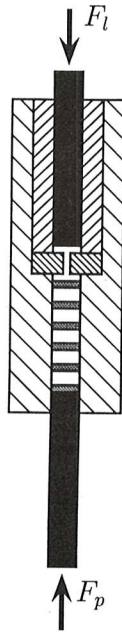The experimental set-up is shown schematically in figure 5.10. The master



Figure 5.10: Experimental set-up constricted tube experiments

cylinder contains a replaceable inner cylinder and a restriction with the dimensions $\varnothing 5 \times 20 mm$. After the experiment has been carried out, the sample and the inner cylinder and restriction can be taken out of the master cylinder for further examination. The plug ($\varnothing 16 \times 60 mm$) consisting of differently coloured slices is put between the lower piston and the restriction. After the apparatus has been heated to the required temperature, the lower piston is driven upwards with a constant rate by means of a hydraulic cylinder with a force $F_p$. On top of the driven piston a load $F_l$ is placed to ensure contact between the piston and the polymer.

For the experiments, the same materials are used as described in previous section. Also the same test series are carried out: PS, ABS, PS/ABS, and

ABS/PS. The tests are performed with a cylinder temperature of 473 $K$ and with a piston velocity of 5 $mm/s$. The thermal soak-time was 20 minutes after the set-point of the temperature has been reached. During heating and cooling, the hydraulic pressure was chosen such that the force $F_p$ equals the load $F_l$. By doing so, the temperature change, which induces volumetric expansion or contraction, takes place under equally isobaric conditions at both sides of the restriction and therefore no material is transported from one side of the restriction to the other.

In the calculations, the fixed domain approach is used (see chapter 3). The mesh containing 2240 elements covers the complete flow domain, thus includes the region below the contraction as well as above the contraction (see figure 5.11). The steel pistons are represented by a material with a
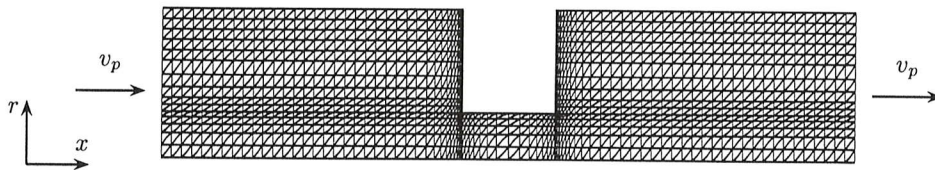


Figure 5.11: Mesh of piston driven contraction problem

high (Newtonian) viscosity of $10^7$ $Pa\,s$ which is about 3 orders in magnitude higher than the viscosity of the polymers. Moreover, the boundary condition at the wall is dependent on the material: a no-slip condition for polymer and a slip condition for the pistons. Every time step the velocity field is calculated using a Picard iteration. The positions of the piston/material interfaces are updated every time step $\Delta t$ by moving them with an amount of $v_p\Delta t$. The viscosity is interpolated linearly per element to avoid the occurrence of unrealistic values in the intergration points. This may occur at the piston/material interfaces due to the quadratic shape functions of the elements used. As a consequence, the 'thickness' of the interface depends on the local mesh size.

The total time-span of 11.9 $s$ ($\Delta s = 60$ $mm$) is divided into 595 timesteps. The tracer deformations are made visible by plotting the colour contours at several values of the label field containing the initial axial coordinates. The time integration is for stability reasons chosen to be fully implicit ($\theta = 1$).

### 5.3.2 Validation

The deformation patterns for PS and ABS at different piston displacements can be found in the figures 5.12 to 5.15 respectively. These results show the same characteristics as is shown in the 'normal' piston driven flow: a reverse fountain flow at the driving piston and a fountain flow at the driven piston. It is remarkable, that the Z-shapes that are developed at the driving piston also can be observed at the upper part of the restriction. However, these Z-shapes originates from those that are developed at the driving piston and do not stem from a reversed fountain flow in upper part of the geometry as is clearly shown in the calculations (see e.g. figure 5.13). The results for ABS differ not much from those of PS, only the deformation of the tracers is larger for PS. The plug flow observed for ABS in the previous section cannot be observed in these experiments, apparently because of the overruling influence of the (axial) deformation in the contraction region. For both materials, the calculated tracer deformations compare well with the experimental results. Only some slight deformation of the piston/polymer interface can be observed.

The tests with the combination of the two materials reveal that the difference in flow behaviour of the two materials has a large effect on the deformation patterns as is depicted in the figures 5.16 to 5.19. For the combination ABS/PS (figure 5.18) the tracer pattern in the lower part (between lower piston and the restriction) tends towards a plug like deformation with the black tracers at the wall surrounding the core material. A closer look shows that the PS material encapsulates the ABS. In figure 5.16 no such phenomenon can be observed, neither any difference can be found in the upper part between the restriction and the driven piston for both combinations when comparing the results to those depicted in the figures 5.8a and 5.9a. Again the resemblance between the experimentally and numerically obtained results is good.

## 5.4  Conclusions

The deformation patterns have proven to be sensitive to all aspects that may influence the flow kinematics and thus can be considered as good comparative experimental information for selective material testing. The material behaviour influences the deformation patterns considerably. Difference in fluid behaviour, e.g. the presence of a yield stress, can be revealed directly from the results.

The numerical simulations show a good resemblance with the experimental results. Even in the case with the piston driven contraction flow, where the piston material is modelled as a fluid with a high viscosity that slips at the walls, the calculations compare well with the experiments.

0 mm        10 mm        20 mm        30 mm        40 mm        50 mm
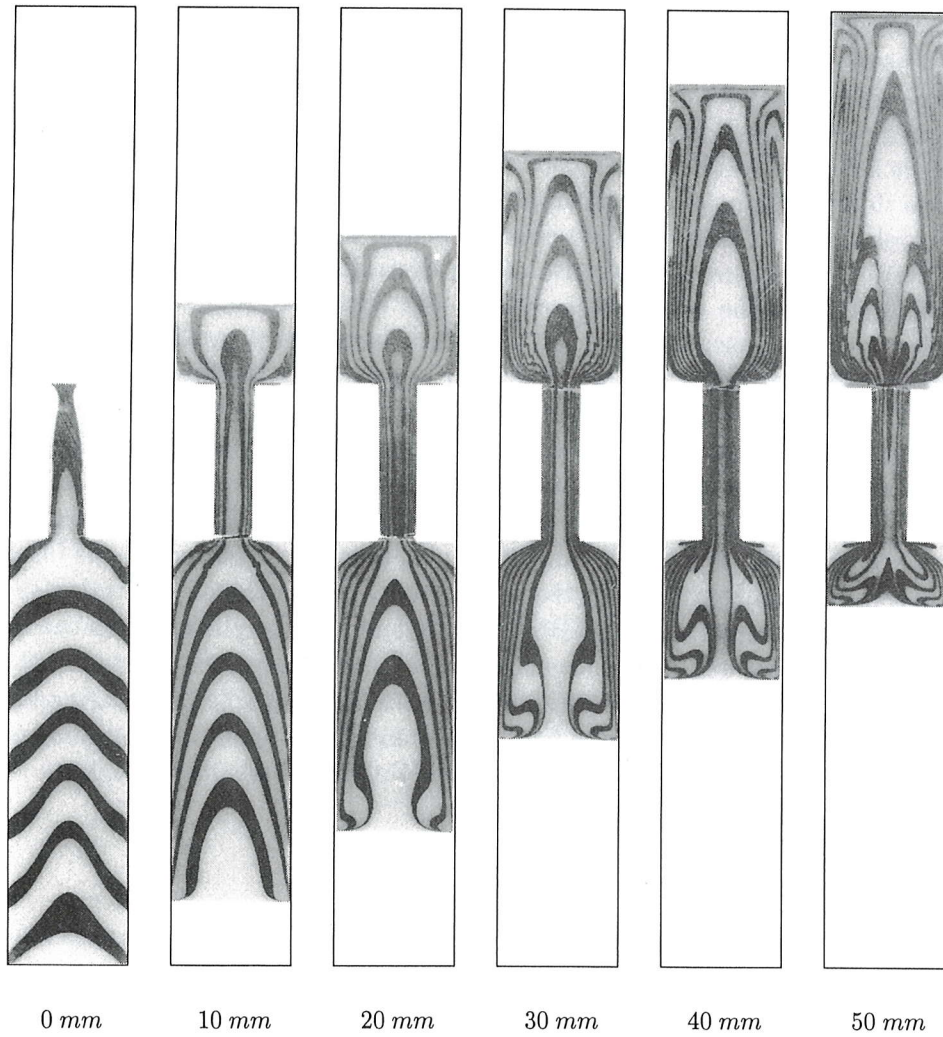
Figure 5.12: Experimental deformation of PS when using a restriction.

| 0 *mm* | 10 *mm* | 20 *mm* | 30 *mm* | 40 *mm* | 50 *mm* |
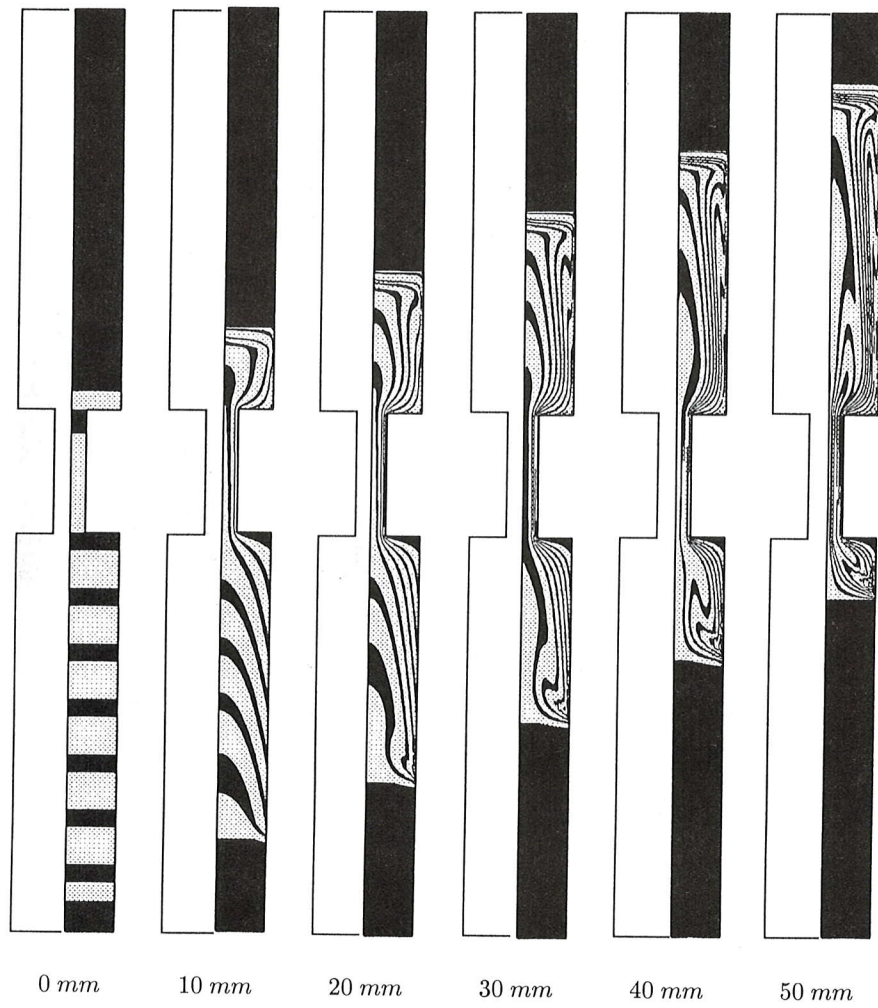
Figure 5.13: Calculated deformation of PS when using a restriction.

0 mm          10 mm          20 mm          30 mm          40 mm          50 mm
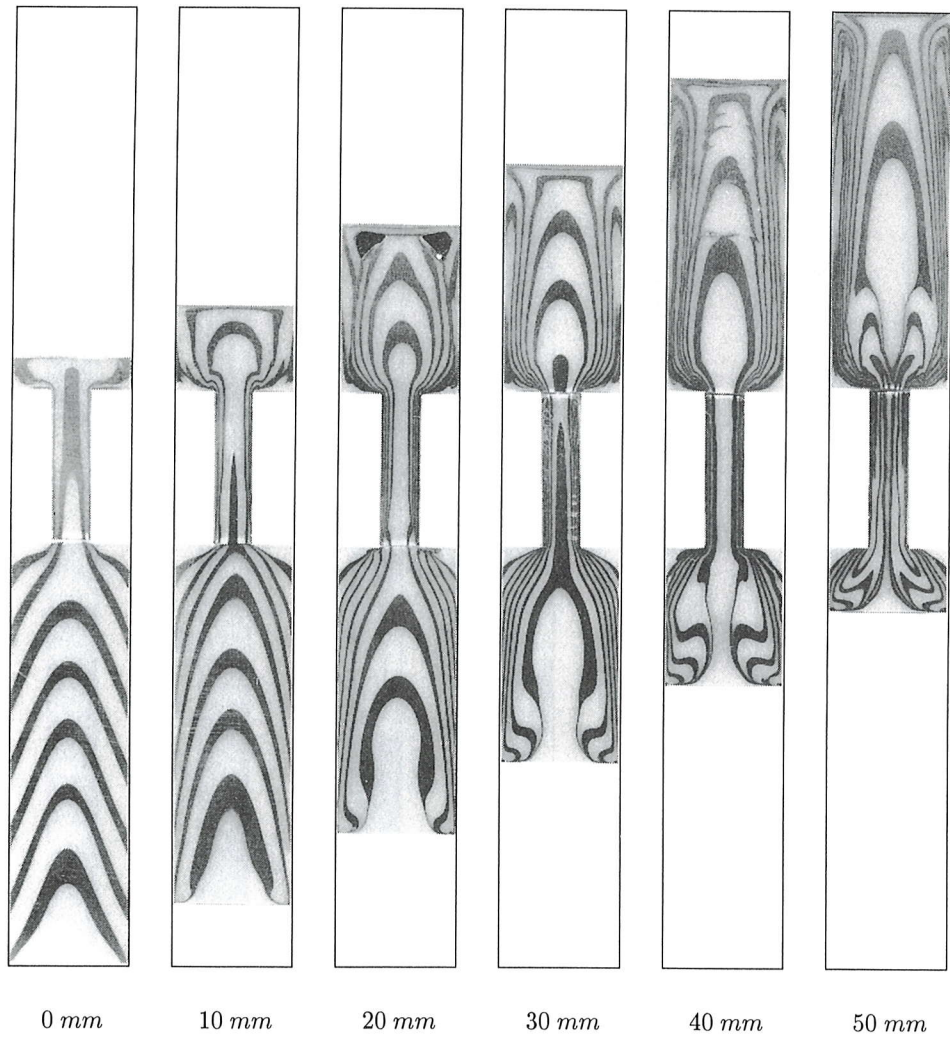
Figure 5.14: Experimental deformation of ABS when using a restriction.

0 *mm*    10 *mm*    20 *mm*    30 *mm*    40 *mm*    50 *mm*
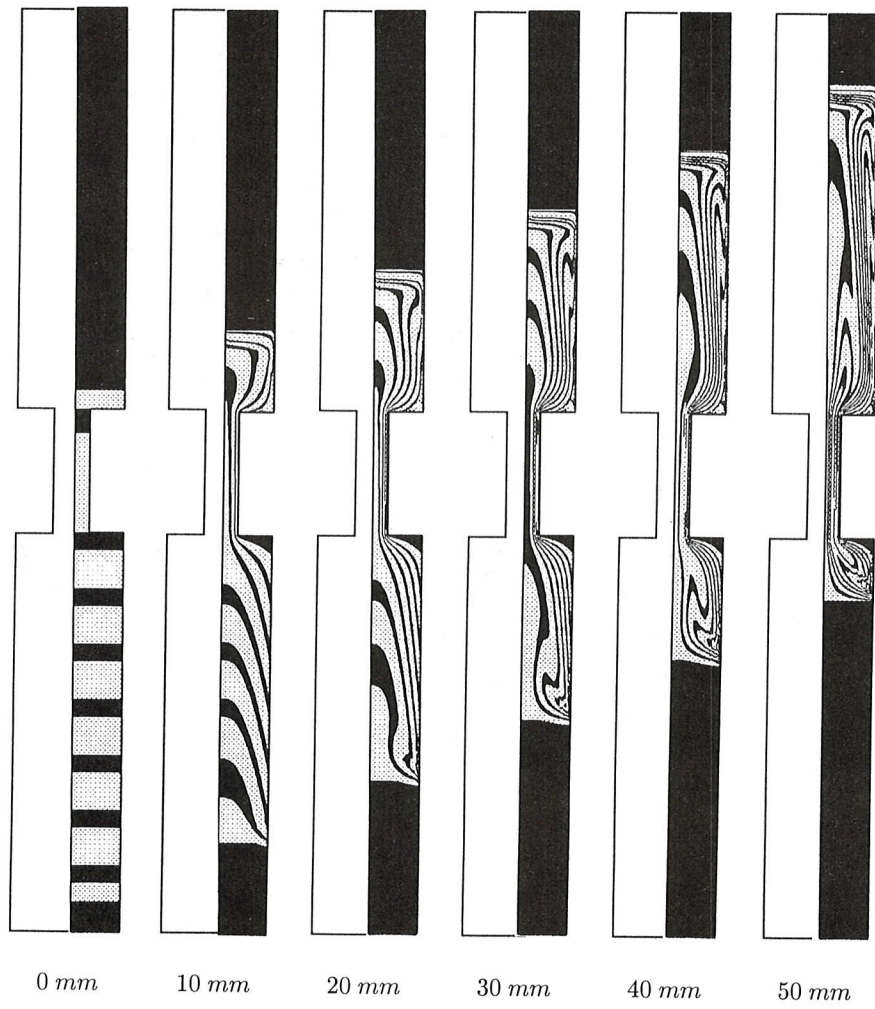
Figure 5.15: Calculated deformation of ABS when using a restriction.

PS

ABS

0 *mm*        19 *mm*        38 *mm*        57 *mm*
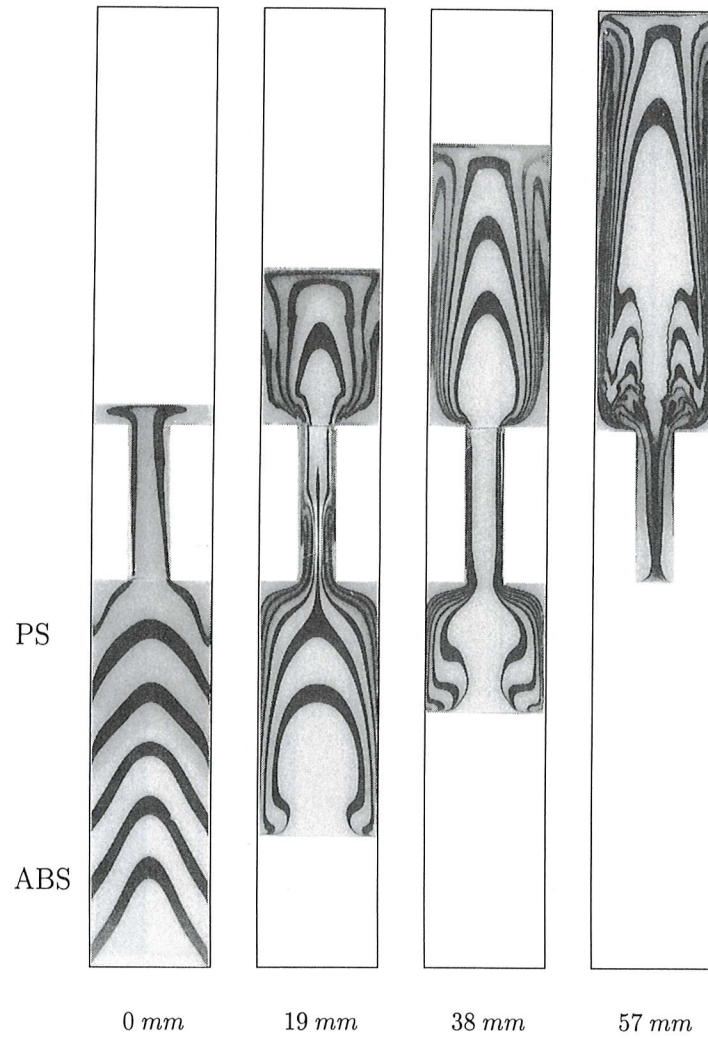
Figure 5.16: Experimental deformations of the materials combination PS/ABS

PS

ABS

0 *mm*        19 *mm*        38 *mm*        57 *mm*
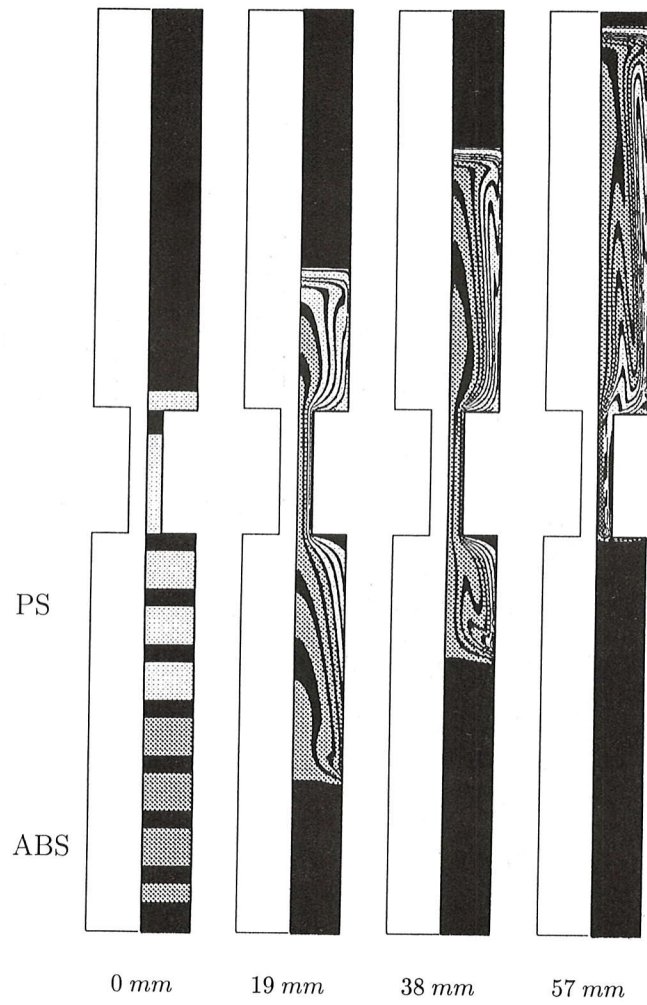
Figure 5.17: Calculated deformation of the material combinations PS/ABS

ABS

PS

0 mm        19 mm        38 mm        57 mm
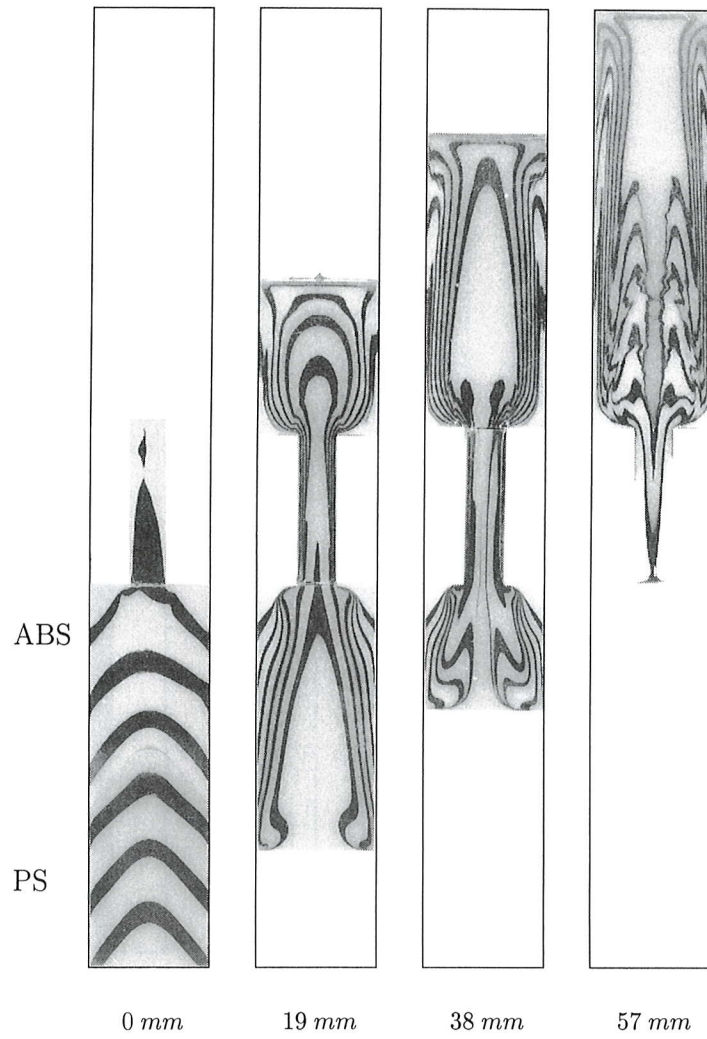
Figure 5.18: Experimental deformations of the two materials combination ABS/PS

ABS

PS

0 *mm*    19 *mm*    38 *mm*    57 *mm*

Figure 5.19: Calculated deformation of the material combination ABS/PS

# Chapter 6

# Multi-component moulding: some examples

## 6.1 Introduction to the case studies

Since modelling of injection moulding and particle tracking are combined in one simulation code (VI$p$), filling with multi-colours or even multi-components can be studied. In this chapter, several characteristics will be elucidated with the aid of three different examples: ($i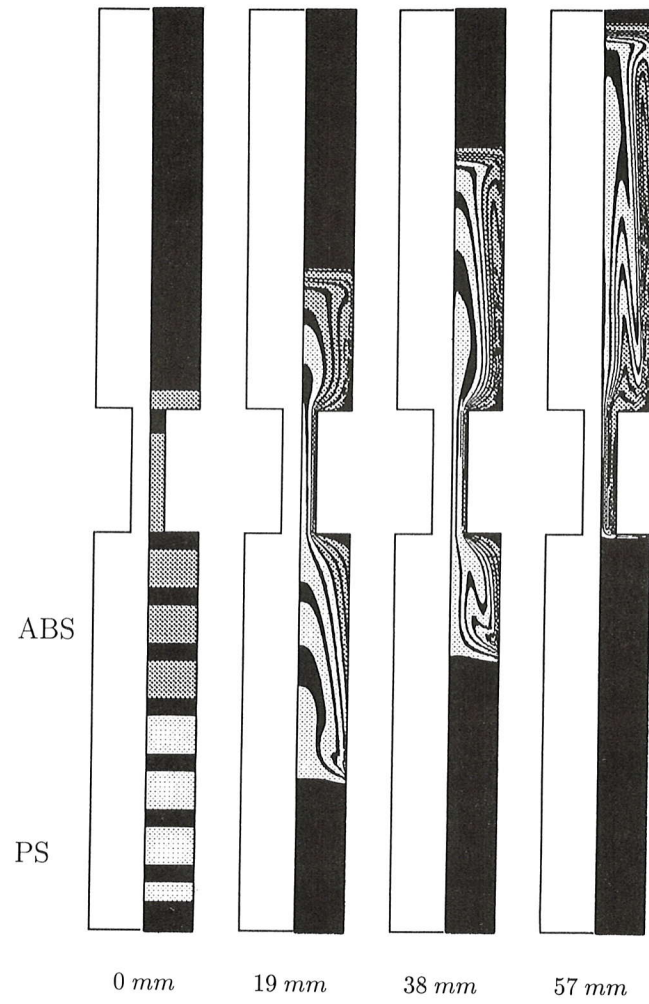$) co-injection of a strip, ($ii$) filling a product with a bifurcation, and ($iii$) inverse mapping in order to determine the injection sequence for a desired colour or even material distribution.

## 6.2 Co-injected strip with ribs

Experimental results were obtained in a cooperation between Philips Centre for Manufacturing Technology, Eindhoven, The Netherlands and the Du Pont European Technical Centre where the products were moulded. The different test series are described in Peters *et al.* (1994) and Hendriks (1992).

### 6.2.1 Experimental conditions

The product consist of a strip of $230 \times 120 \times 2.3$ $mm$ with 4 stiffener-ribs and a beam-like edge (see figure 6.1). The ribs are 12.7 $mm$ in height and have different cross-sections. The beam-like edge ($7 \times 9 \times 120$ $mm$), acting as a flow divider, connects the strip with the runner section. The product is filled by sequential injection of two differently coloured nylons (PA66). The colour first injected was white-translucent, followed by the second which was blue. They are also referred to as skin and core material respectively.
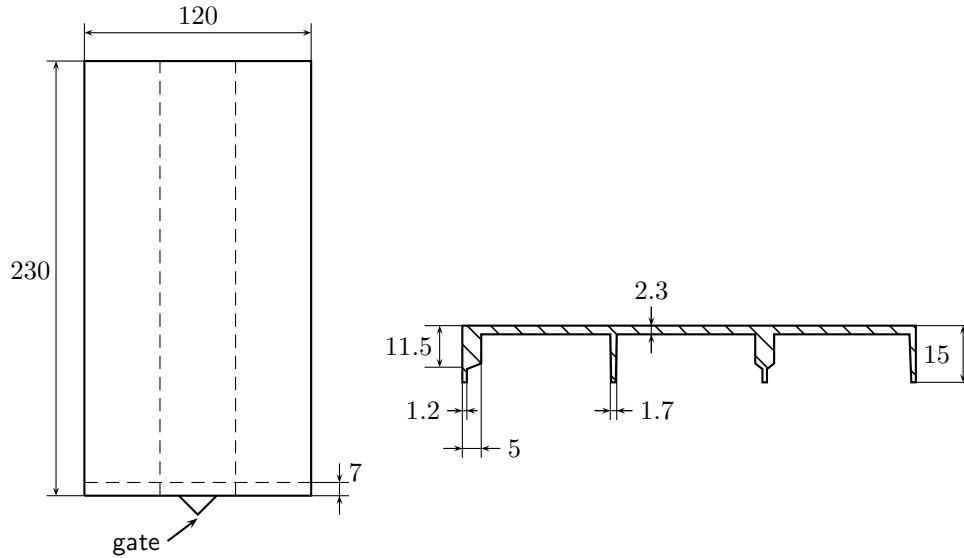
Figure 6.1: Schematic drawing of test geometry

The strips were injected in a mould with a constant temperature of 348 $K$ using different processing conditions. In particular the injection temperature of the two materials and their relative fractions were altered, see table 6.1. The core material is injected after the product has been filled up to the

| series | $T_{inj}$ $[K]$ | | $swp$ |
|--------|-----------------|-----------|-------|
|        | skin (1)        | core (2)  |       |
| PA1    | 571             | 556       | 67 %  |
| PA2    | 571             | 556       | 50 %  |
| PA3    | 571             | 556       | 22 %  |
| PA4    | 571             | 556       | 56 %  |
| PA5    | 574             | 573       | 56 %  |
| PA6    | 556             | 568       | 56 %  |

Table 6.1: Processing conditions test series PA1-PA6

volume percentage given by the switch point *swp*. The machine settings aimed at an average flow rate of $1.33 \cdot 10^{-4}$ $m^3/s$. The measured filling time proved to be about 1.9 $s$ for product including runners (with a total volume of $1.16 \cdot 10^{-4}$ $m^3$), thus the actual flow rate was less: about $6.1 \cdot 10^{-5}$ $m^3/s$. In the calculations the runner section is not taken into account, so the volume to be filled is $1.00 \cdot 10^{-4}$ $m^3$. The finite element mesh covering the midplane of the cavity is plotted in figure 6.2. Since no details about the exact temperature

(distribution) are known, cooling is assumed to be symmetrical over the thickness direction and a Biot-type of boundary condition is chosen with a heat transfer coefficient of $H = 3000 \ W/(m^2K)$. For that reason, and to save computing time, only one half of the thickness is considered. The half gapwise thickness is discretized using 25 gridpoints with 13 points (including the solid/liquid interface) equally divided over the fluid part and 12 points in the solid layer.
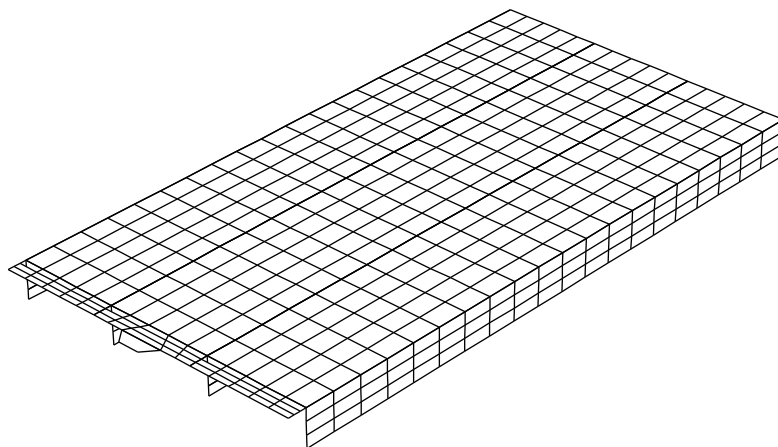
Figure 6.2: Finite element mesh coinjected strip with ribs

The main points of interest in this example are:

- application to relatively complex geometries should be possible, since this is the aim of the simulations.

- the simulation code should be capable to predict the influence of the main processing conditions on the material/colour distribution in the product.

- a proper prediction of break-through of the first injected material by the second injection material, because the occurence of undesired break-through is the most common problem to solve in practice of multi-component moulding.

## 6.2.2 Validation of the numerical simulations

Identical to the test problems dealt with in chapter 5, the colour distribution is used for visual validation of the results. Since the skin material is translucent, the skin/core material distribution can be determined easily without cutting the sample in pieces. The same holds (but to a somewhat less extent)

for the areas where the blue core material breaks through the skin material and ends up at the product surface.
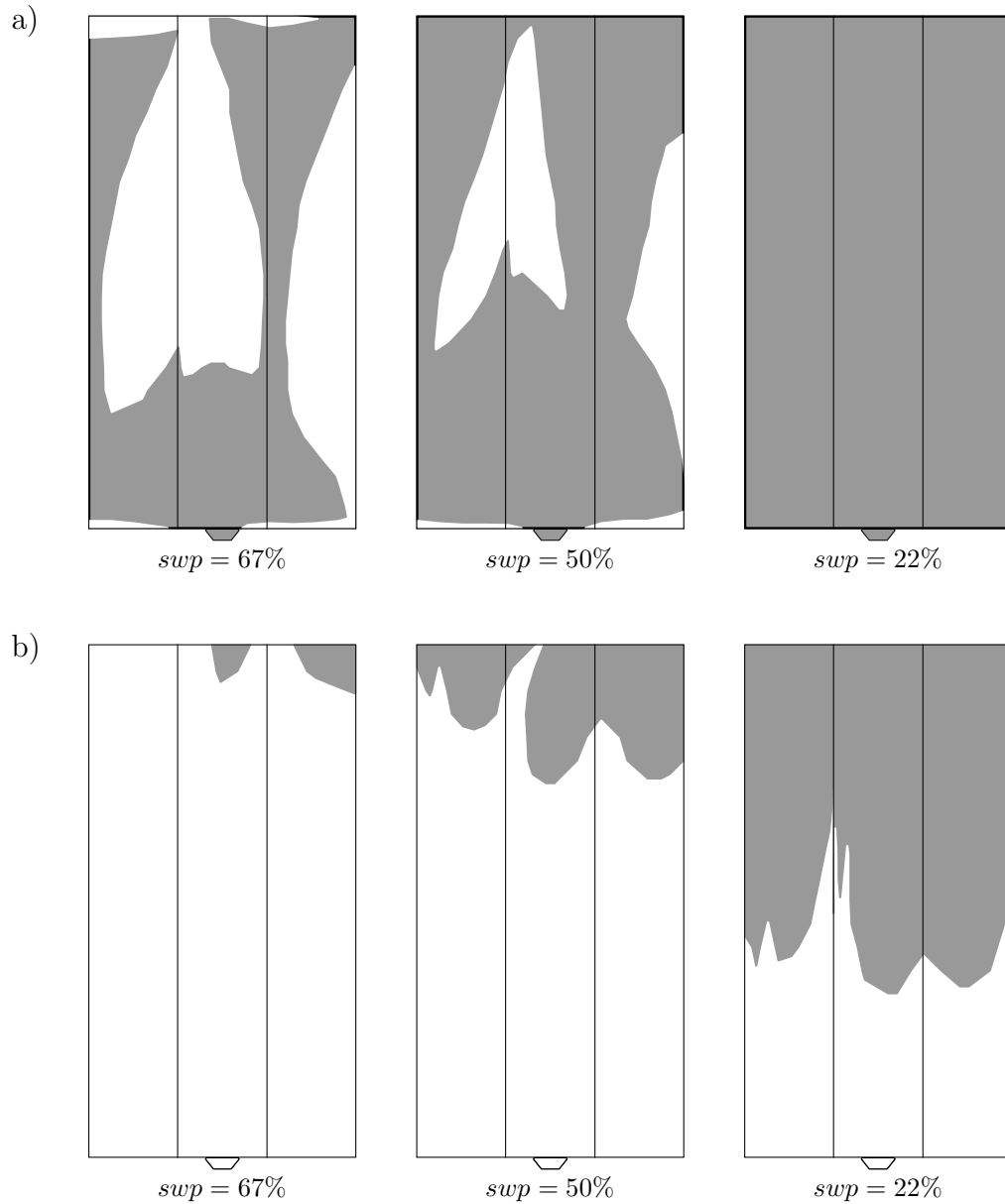


Figure 6.3: Experimental material distribution in the midplane (a) and break-through areas (b). Influence of swith point ($T_{inj1,2} = 571, 556\ K$).
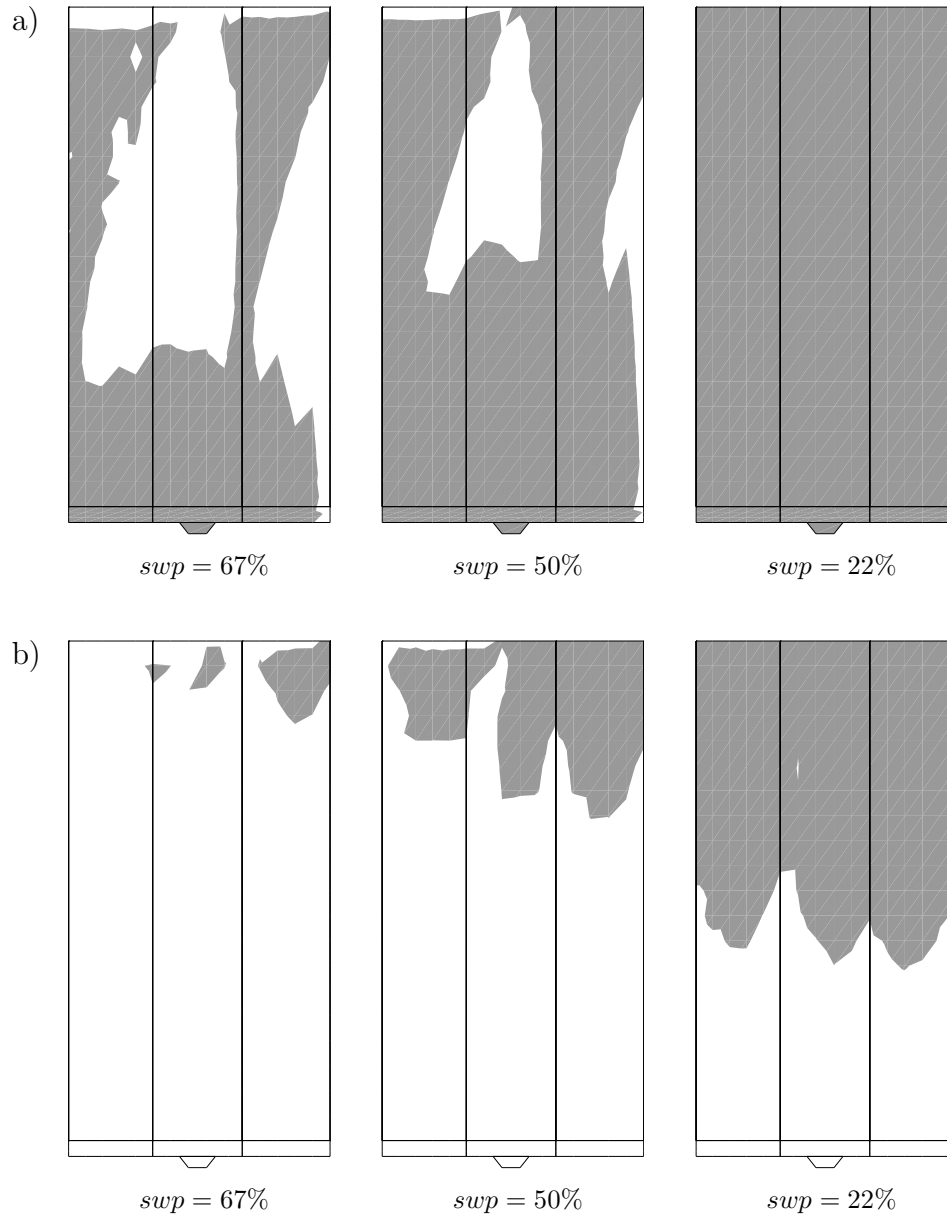
Figure 6.4: Calculated material distribution in the midplane (a) and break-through areas (b). Influence of swith point $(T_{inj1,2} = 571, 556 \ K)$.

a)



$$T_{1,2} = 571, 556\ K \qquad T_{1,2} = 574, 573\ K \qquad T_{1,2} = 556, 568\ K$$

b)



$$T_{1,2} = 571, 556\ K \qquad T_{1,2} = 574, 573\ K \qquad T_{1,2} = 556, 568\ K$$
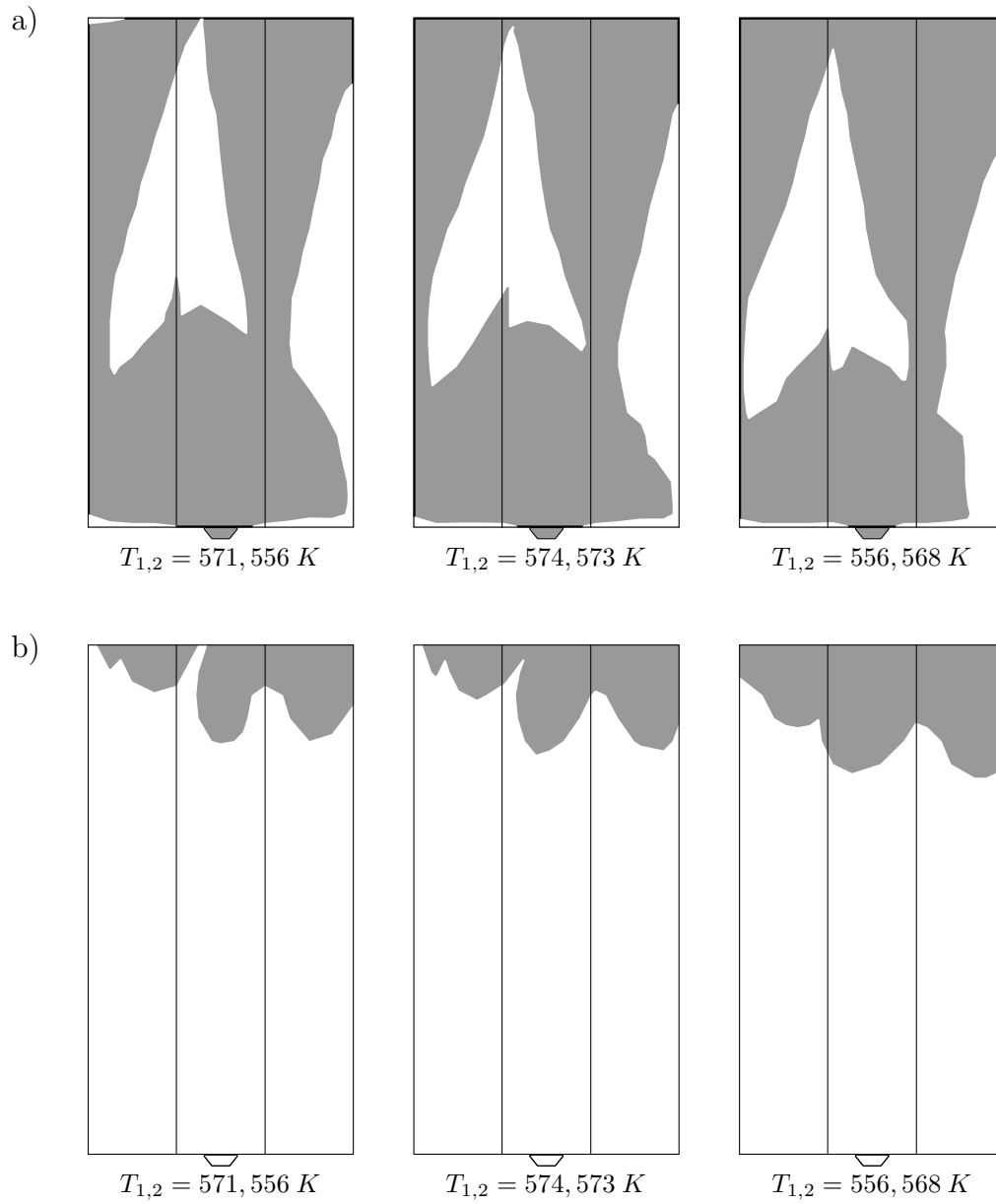
Figure 6.5: Experimental material distribution in the midplane (a) and break-through areas (b). Influence of melt temperature ($swp = 56\%$).

a)



$$T_{1,2} = 571, 556 \ K \qquad T_{1,2} = 574, 573 \ K \qquad T_{1,2} = 556, 568 \ K$$

b)



$$T_{1,2} = 571, 556 \ K \qquad T_{1,2} = 574, 573 \ K \qquad T_{1,2} = 556, 568 \ K$$
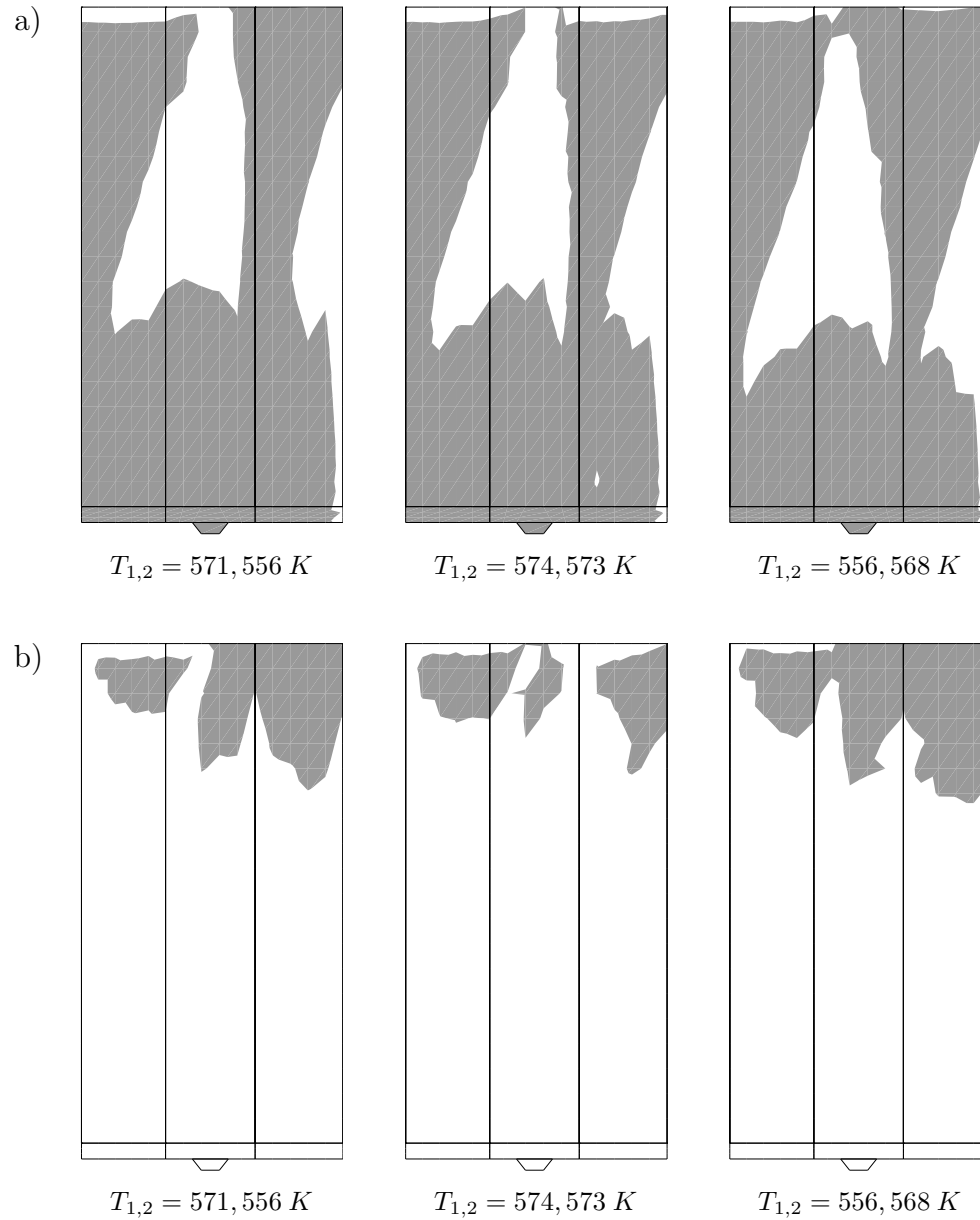
Figure 6.6: Calculated material distribution in the midplane (a) and break-through areas (b). Influence of melt temperature ($swp = 56\%$).

Since with sequential injection the material or its colour only changes in time, the injection time labels provide the necessary information for visualization of the final distribution. In this case, a simple colour contour plot provides sufficient information. Needed are the two contour levels that coincide with the switch time and the total filling time respectively. The

core material distribution is, subsequently, visualized by constructing these contour plots in the midplane of the product, while the break-through areas are easily found by plotting the label field at the surface.

The influence of the switch point on the material distribution is shown in the figures 6.3 and 6.4 for the experimentally and the numerically obtained results respectively. Figure 6.3a and 6.4a clearly shows that the thick ribs act as flow leaders and make the second material penetrating into (or in between) the first material. If the switch-point number is decreased more blue material is injected. This is clearly demonstrated in the midplane but also the break-through area grows (see figure 6.3b and 6.4b). Comparing the predicted colour distributions with the experimental ones for the different processing conditions, One can conclude that a good resemblance is found. Only the presence of some skin material in the flow divider is not found, because no solidified layer is formed at the edges of a product when employing the $2\frac{1}{2}$-D approach. Also the amount of first material that remains in the midplane is slightly underpredicted at the righthand side of the product.

The effect of the initial skin and core temperature is demonstrated in the figures 6.5 and 6.6. Although the variation in temperature is relatively small, a noticeable influence on the distribution is found. The mechanism that is thought to cause this effect, is the growth of the solidified layers during the injection. The lower the melt temperature of the first, white material, the thicker the solidified layer will be. Then, more second, blue material will flow through the thicker ribs which have the lowest flow resistance. As a consequence, the area occupied by the white material in the midplane is shifted towards the gate and the break-through area is somewhat larger. Even for these extreme small changes in processing conditions a remarkably good agreement between the numerical simulations and the experiments is obtained.

# 6.3    Bifurcation of the midsurface

In order to attain meaningful results for multi-component injection moulding, it is important that during simulations the identity of the material particles is preserved. In the case that bifurcations of the midsurfaces are present, like e.g. stiffener ribs that are perpendicular to the flow, the melt flow has to be splitted to fill both the rib and the remaining part. All $2\frac{1}{2}$-D codes have problems in this respect. In the usual, existing codes, the pressure is calculated by satisfying the local conservation of mass at the flow splittings in a weak sense by forcing that the sum of the inflow volume fluxes equals the sum of the outflow fluxes. However, in calculating the history dependent properties like e.g. temperature, density, visco-elastic stresses, orientation, conversion and the identity or colour of particles, copying of the gapwise distribution of properties from an upstream branch to the downstream branches is not allowed since local conservation of identity is not satisfied. To overcome the problem of cloning the material particles, the bifurcations should be treated differently as described in section 3.2.3. When modelling the flow splittings correctly, Couniot *et al.* (1993) showed that e.g. the resulting gapwise temperature profiles in the downstream branches are changed considerably when compared to the results of the existing simulation codes. An initial symmetric profile in an upstream branch results in asymmetric temperature profiles in the downstream branches, which in turn induces warpage of the product.

The most elementary geometry of a bifurcation is found in a T-shaped strip (figure 6.7). The strip consist of three branches (A,B,C) with the di-
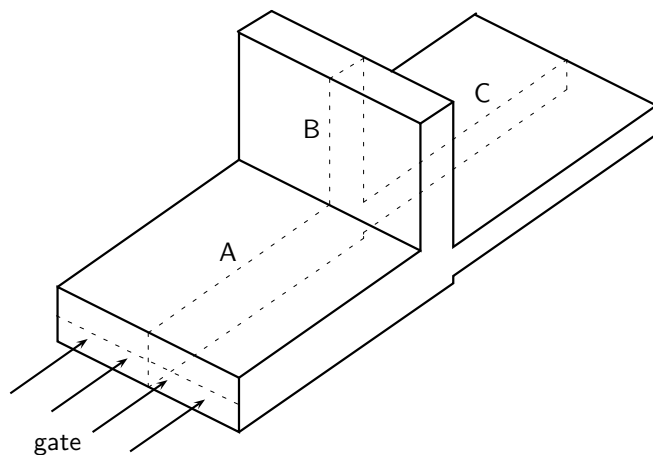


Figure 6.7: Schematic drawing of the T-shaped strip

mensions (length × width × thickness): A: $40 \times 40 \times 2.5$ *mm*, B: $30 \times 40 \times 2.5$ *mm*, and C: $40 \times 40 \times 1.5$ *mm*. The flow can be considered so-called one-

dimensional, since the strip is fed by a line-gate over the full width of the sample and results are considered only in the mid cross-section of the sample, represented by the dashed line in figure 6.7. In the $2\frac{1}{2}$-D approach, the mid-planes of all distinct branches that form the total product are interconnected. Consequently, a small overlap exists in the connections. For clearness, the three branches of the T-shaped strip of figure 6.7 are disconnected.

The material properties are those of polystyrene Styron 678E (see Chapter 4). The main processing conditions are:

- flow rate $Q = 9.4 \cdot 10^{-6} \ m^3/s$ (injection time $t_{inj} = 1.0 \ s$)

- melt temperature $T_{inj} = 503 \ K$

- mould temperature $T_{wall} = 323 \ K$.

Asymmetry of the gapwise temperature profiles is allowed for. The boundary condition chosen for the temperature is again the Biot condition with $H = 3000 \ W/(m^2 K)$. The grid in the gapwise direction consists of 49 points of which respectively 8 and 33 points are evenly distributed over each solid layer and the fluid layer.

The results of the calculations performed using the strategy of existing computer codes can be found in figure 6.8 for the injection time label distribution ($t$-label) and figure 6.9 for the gapwise injection position ($z$-label). The label values are made dimensionless with the injection $t_{inj}$ and the half gap width $h/2 = 1.25 \ mm$ respectively. The injection time labels visualize the distribution of the residence time, which equals $1 - t_{label}$, over the product and, moreover, coincides with the material distribution in sequential moulding. The colour contours in the two downstream branches differ, since the dimensions are chosen such that branch B is filled completely before C. The gapwise entrance position $z$, however, is hardly influenced by this filling behaviour. Figure 6.8 and 6.9 clearly demonstrate the effect of the fountain flow on the label distributions: the colour originally injected in the midplane can be found at the surface. The $z$-label distribution shows clearly that the gapwise distribution of label values in both downstream branches are similar which is in conflict with the conservation of identity principle. The results when using the local mass balance to divide the material particles over the two downstream branches as described in section 3.2.5 are given in figure 6.10 and 6.11. These are the (approximated) correct results which differ essentially with those of figure 6.8 and 6.9. The $z$-label distribution in branch B only contains values originated from the upper half of the feeding branch A whereas branch C contains both label values that stem from the lower part as well as from the upper part. The latter particles have entered branch C after

branch B has been filled completely. The most important difference between both approaches can be found at the surface of branch C where particles that are injected in the lower half of the gap-width end up at the upper surface of this branch when preserving conservation of identity. From these results, it can concluded that for practical applications, where break-through often is undesirable, the correct approach should be employed.

Finally, the effect of the proper splitting technique for history dependent properties is demonstrated in figure 6.12 and 6.13 for the both approaches. In these figures the gapwise temperature profiles at different positions along the flowpath are plotted. Again, a considerable influence of the local mass conservation on the overall distribution can be observed.
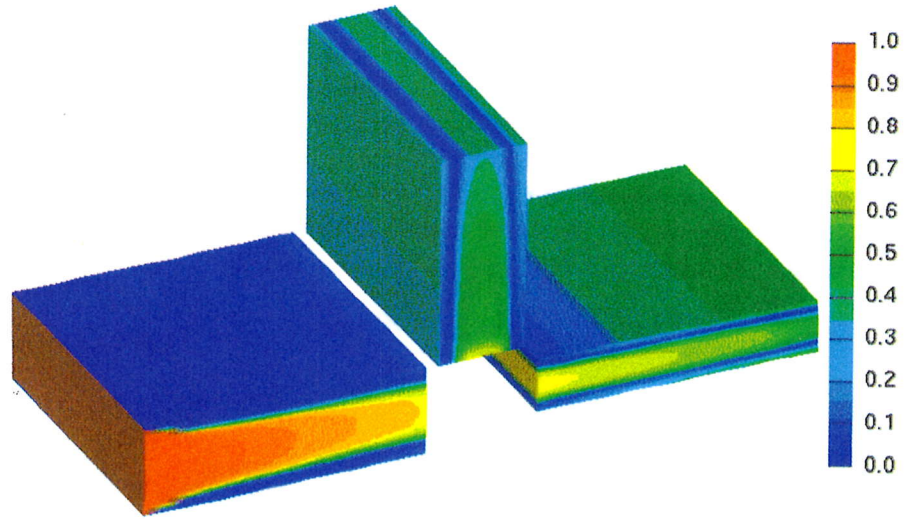
Figure 6.8: (Wrong) injection time label distribution in cross-section T-strip, according to existing computer codes
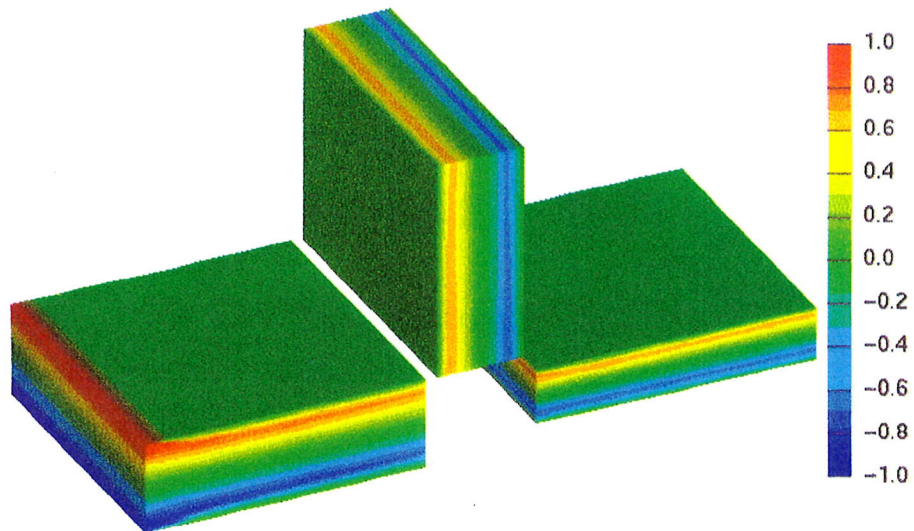


Figure 6.9: (Wrong) gapwise injection position label distribution in cross-section T-strip, according to existing computer codes
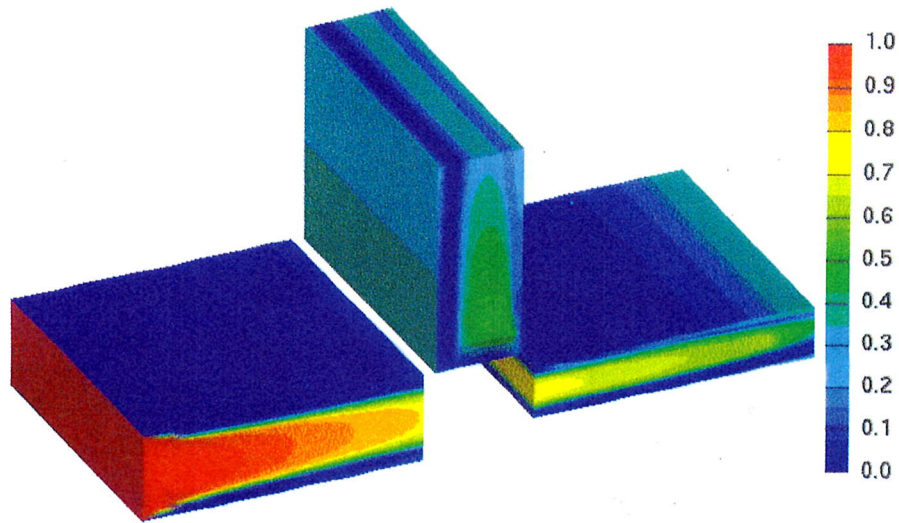
Figure 6.10: Correct injection time label distribution in cross-section T-strip, according present code
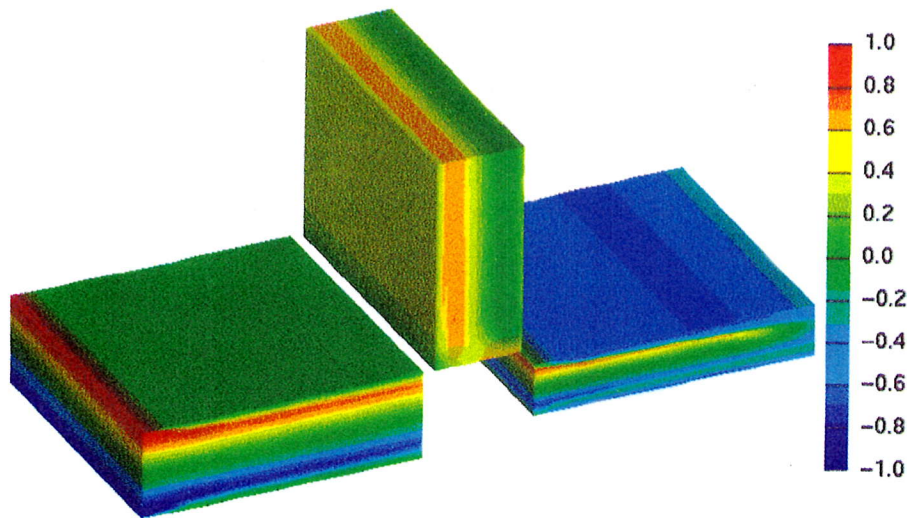


Figure 6.11: Correct gapwise injection position label distribution in cross-section T-strip, according to present code
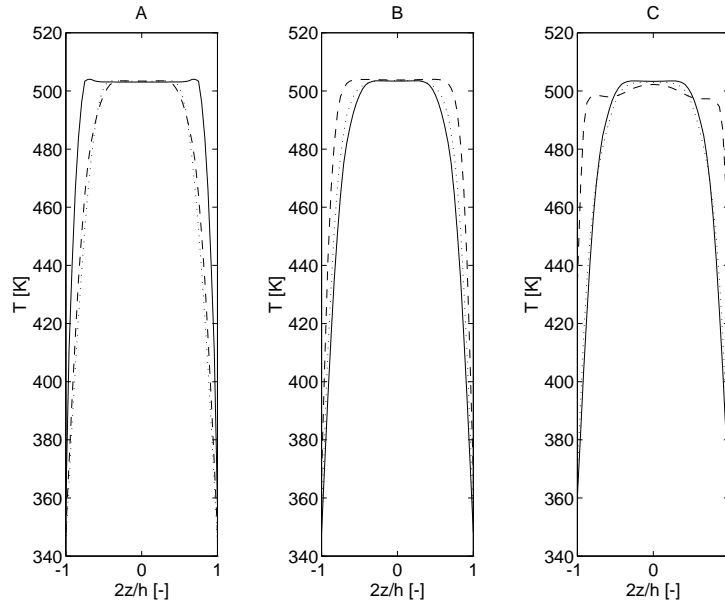
Figure 6.12: (Wrong) gapwise temperature profiles at different positions along flowpath of each separate branch (0%: full line, 50%: dotted line, 100%: dashed)
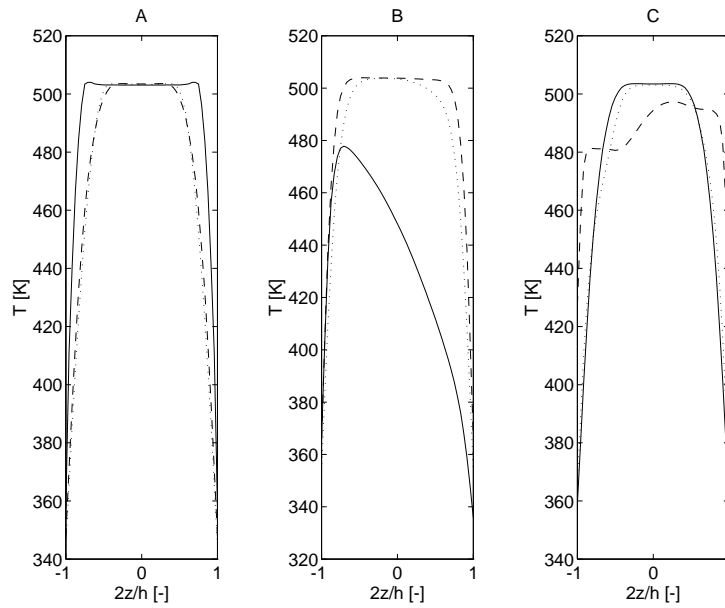


Figure 6.13: Correct gapwise temperature profiles at different positions along of each separate branch flowpath (0%: full line, 50%: dotted line, 100%: dashed line)

# 6.4   Inverse mapping

In this section, two examples are given of the inverted problem which can be formulated as : *determine the configuration that has to be injected to attain the requested material distribution in the product.* In the first example, a relatively complex product is considered for in multi-colour moulding whereas the application of an iterative technique is demonstrated for the filling of a simple rectangular mould with dissimilar materials.

## 6.4.1   Multi-colour moulding

The product considered is drawn schematically in figure 6.14 by the finite element mesh of the midplane (each element has a dimension of $10 \times 10 \ mm$). It consists of a square plate ($80 \times 80 \times 2.5 \ mm$) with an opening ($30 \times 30 \ mm$)
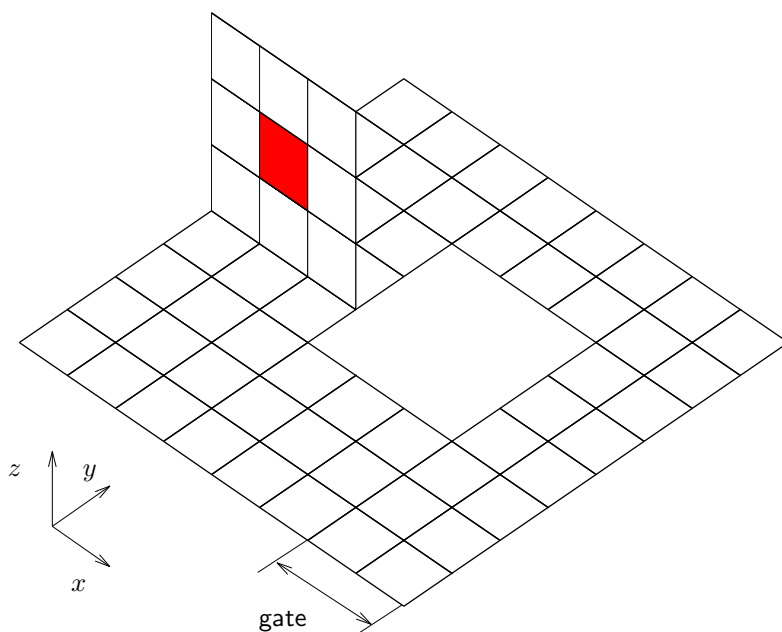


Figure 6.14: Schematic representation of the product (finite element mesh)

and a rib ($30 \times 30 \times 1.5 \ mm$). The plate is filled in $1.0 \ s$ through a line gate of $20 \ mm$ in width. The material used is polystyrene (PS). The processing conditions are the same as used in the previous example.

The melt front advancement is plotted in figure 6.15. It can be observed that the rib is initially filled up to about 30%, then the melt in the rib stops flowing and, only after the remaining of the plate has been filled completely, the melt front in the rib starts to move again. Due to this filling behaviour and the presence of the flow splitting, the label distribution in the rib and
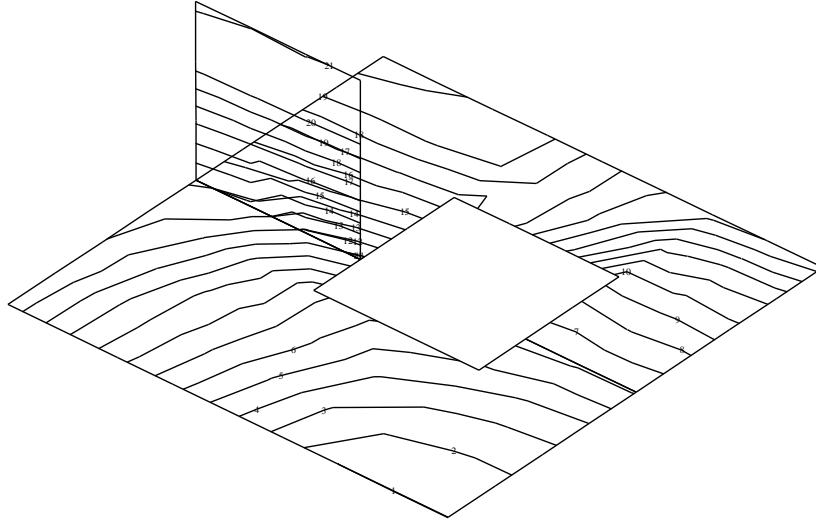
Figure 6.15: Calculated flow front positions (the increment of the adjacent contour
lines is 0.05 *s*)

in the small area behind it will be complicated. The task to accomplish, as
an example, is to make the shaded area in the rib (see figure 6.14) to be of
a different colour over the entire gap-width. The inverse mapping can be
performed easily by looking for the label values in that area and plot them
in the $x, t, z$-plane (see figure 6.16), where $x, z$ denote the entrance position
along the gate and the gapwise position respectively (see figure 6.14), and
$t$ the time of injection. By multiplying the injection time with an average
filling speed, the 3D space plotted in figure 6.16 can be considered to be the
configuration of coloured materials that has to be injected. Thus, to reach
our goal, a box-like volume (of dimensions: $20 \times 2.5 \times \bar{v}\,t\ mm$) containing
the volume rendered in figure 6.16 of differently coloured material has to be
established.

The small elements that define the volume, are the inverse mapping of
the volumes enclosed by two successive gridplanes in the gapwise direction
and the boundaries of the shaded area. The 'starting-points' of the material
volume originates from the gridplanes situated near the surfaces while the
part that is injected last (in the 'bend'), emanates from the midplane. So,
the volume can be regarded as a kind of parabola in 3D which will be inverted
by the velocity profile to end up, after injection, as a straight line. However,
the complexity of the filling pattern results in a somewhat more complicated
structure.

In order to derive the machine settings from the data obtained by the
inverse mapping, a better visualization method should be employed. One
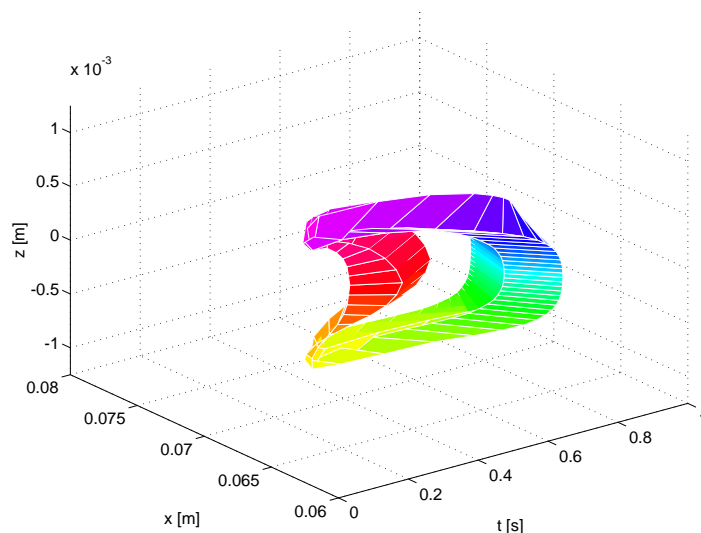
Figure 6.16: Injection configuration obtained by the inverse mapping

possible method is to slice the volume at constant injection times to establish cross-sections of the injection configuration. These data are easier to interpret than the 3-D structure showed before.

## 6.4.2 Multi-component moulding

A rectangular strip of dimensions $200 \times 50 \times 3$ $mm$ is chosen for demonstration of the iterative technique in the inverse mapping procedure. Starting with a simulation with one component, the injection configuration is determined and subsequently injected in a multi-component simulation. This procedure is repeated until the shape of the required distribution has been converged to a sufficient degree. The processing conditions are similar to those used in the previous examples and the material considered as a reference in the first calculation is polystyrene (PS). The material that should occupy the specific location in the product, reffered to as material X, differs only in viscosity with PS. The viscosity of this (artificial) material equals $\eta = \eta_{PS}/3$. The task to fulfil is to establish the material distribution depicted in figure 6.17a. The shape spanned by the points in figure 6.17a is obtained after injection of the configuration that is previously determined (figure 6.17b). Due to numerical errors, some points are outside the region that is considered to be occupied by material X. Nevertheless, this situation is taken as the reference condition. After 3 iterations, the shape of the layer agree satisfying well with the reference situation (see figure 6.18a), so the procedure is stopped. Finally, the configuration that has to be injected to

reach our goal is plotted in figure 6.18b. Concluding, it can be stated that



(a) Required material distribution         (b) Injection configuration
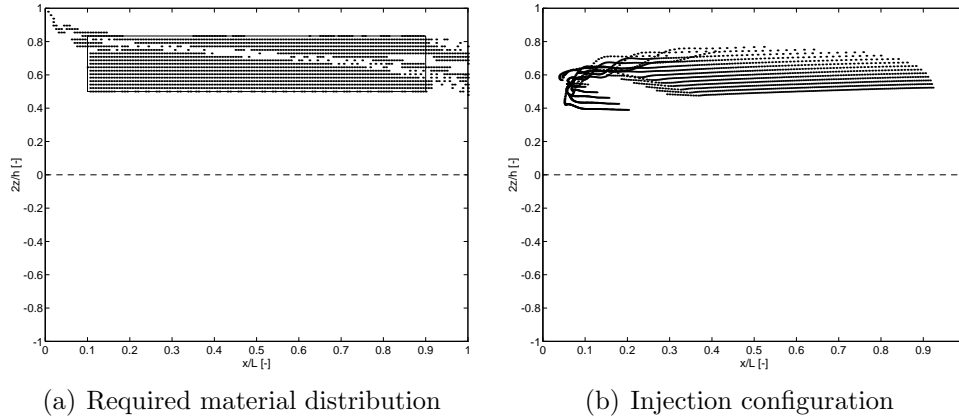
Figure 6.17: Initial condition inverse mapping procedure



(a) Required material distribution         (b) Injection configuration
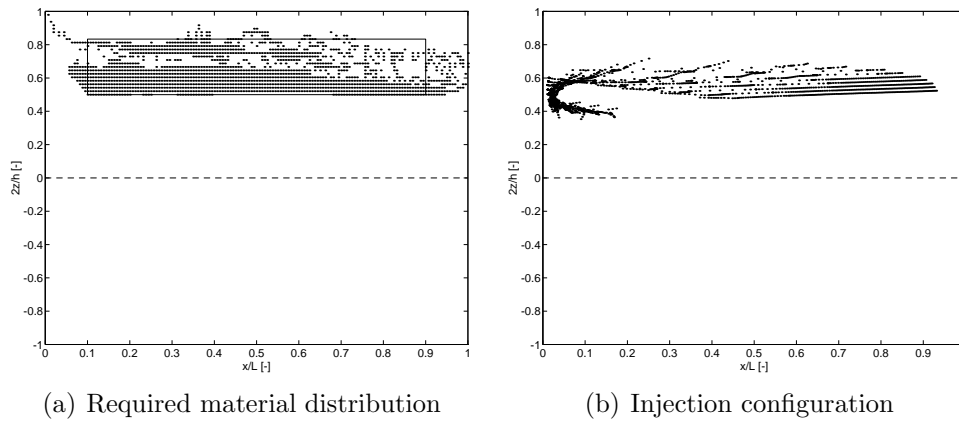
Figure 6.18: Converged results inverse mapping procedure (third iteration)

the inverse mapping technique can be applied iteratively to determine the injection configuration in real multi-component moulding. Application of the procedure to complexly shaped products make high demands on the capabilities of the necessary data processing software. In spite of some irregularities in the injection configuratons caused by numerical deficiences in calculating the label identities, especially for the material elements that has experienced the fountain flow, the method demonstrated its usefulness.

# 6.5    Conclusions

**Co-injected strip with ribs**    By sequential injection of two differently coloured materials, it proved that the material distribution throughout the product is rather complicated, although the geometrical complexity of the mould was not that high.  The colour pattern in the core layer as well as the break-through areas at the surface are predicted satisfactorily well for the processing conditions given, notwithstanding the fact that not all experimental conditions (e.g. the mould temperatures) were known in detail.

**Bifurcation of the midsurface**    To preserve the identity of material particles, a splitting technique at bifurcations of the midsurface has to be employed.  An initially symmetric gapwise profile of a property attached to material particles, like temperature, density, visco-elastic stresses, orientation, conversion and identity, always changes into an asymmetrical profile in the downstream branches.  As a consequence, symmetry can no longer be assumed and the total thickness of the product has to be modelled.

**Inverse mapping**    The inverse mapping in the case of multi-colour moulding can be carried out easily, but the results are hard to interpret and demand for an advanced visualization technique.  Even for relatively simple geometries, the injection configuration proved to be complex.  The very complex and challenging problem of making the injection configurations that correspond with the requested arbitrary material distributions in the product has proven to solved for a simple geometry.

# Chapter 7

# Conclusions and recommendations

Combined with the modelling of the filling stage in the injection moulding process, particle tracking based on the conservation of identity of material particles is employed in the simulation of multi-component moulding. Special attention is paid to the fountian flow and the local conservation of mass at flow splittings in the $2\frac{1}{2}$-D approach. The polymer melts used, polystyrene (PS), acrylonitrile-butadiene-styrene (ABS), and polyamide (PA), are modelled as generalized Newtonian fluids and the appropriate model parameters are determined by rheological characterization. The modelling is tested by comparing numerical and experimental results for two well-defined flow geometries, the flow advancing between two pistons in a tube with or without an restriction using different materials and material combinations. Application of particle tracking to the simulation of multi-component injection moulding yielded the material distributions throughout the products which is compared with experiments. The importance of a correct modelling of flow bifurcations is demonstrated. Finally, two examples are given of the inverse problem: i.e. the determination of the injection configuration for a specified two component product configuration.

## 7.1 Conclusions

The simulation of the filling stage in multi-component injection moulding can be accomplished by adding an extra conservation law – the conservation of identity of material particles – to the existing set of equations that generally defines the $2\frac{1}{2}D$ approach. In that approach the conservation of mass is only

weakly satisfied. Improving this formulation by enforcing a local mass conservation at the front line and at flow splittings, the distribution of material particles in a injection moulded product can be predicted more accurately. As a consequence, a meaningful prediction of the material distribution in multi-component injection moulding, or the final properties of an injection moulded product which are affected by the history dependent variables like temperature, density, visco-elastic flow-induced stresses and the degree of reaction, is only possible if the improved method is employed.

The mathematical formulation of the particle tracking problem results in a hyperbolic (scalar) convection equation which can be solved adequately by the Streamline Upwind Petrov Galerkin (SUPG) finite element method. The same method can be applied to solve the material derivatives when the convective operator is splitted from the remainder of the equations.

The modelling is first tested with two well-defined flow geometries: the piston driven flow with and without a contraction. Using differently coloured slices of the same polymer material, the deformation patterns can be visualized both experimentally and numerically. These deformation patterns have proven to be sensitive to all aspects that may influence the flow kinematics and thus can be considered as good comparative experimental information for verification of the modelling, computer codes or even for selective material testing. Differences in fluid behaviour, e.g. the presence of a yield stress for ABS, can be revealed directly from the results. The deformation field observed for ABS was mainly governed by the presence of the yield stress, the effect of the difference between the yield stress values measured in dynamic or static (constant stress) shear experiments could be observed clearly. For PS, the experimental results did not fully coincide with the numerical results, although all characteristics were revealed. Visco-elastic effects are thought to play an important role for this material. Tests with the different combinations of PS and ABS showed that the conservation of identity method also can be applied succesfully to track the material interfaces.

The fixed domain approach turned out to be applicable for solving the piston driven contraction flow. Instead of an adaptive meshing or local remeshing technique for the time dependent domain, the complete domain is considered in which the pistons are represented by an artificially high viscosity material that slips at the wall. The deformation patterns in the polymer material could be predicted with a sufficient accuracy, taken in consideration that the steel/polymer interface formed the most severe case to be solved when compared to e.g. the interface between PS and ABS in the multi-material experiments.

In multi-component injection moulding the break-through of the second injected material through the first injected material is completely governed

by the fountain effect at the flow front. Even for geometrically simple products, the material (or colour) distribution turned out to be rather complex. Therefore, assistance of computer simulations is indispensable to achieve the desired material distribution in the product. The effect of preserving the local mass balance at flow splittings results in asymmetric gapwise profiles of history dependent properties or identity labels in the downstream branches whereas they were symmetrical in the upstream part.

In order to define the injection sequence and/or configuration that should result in the requested material distribution, an inverse calculation has to be performed. Using the conservation of identity method, this calculation reduces to an inverse mapping. The inverse mapping can be carried out straightforward, provided that the determined injection configuration does not change the flow kinematices. This is e.g. the case in simple multi-colour injection. In the case of real multi-material injection, however, an iterative technique has to adopted in which the multi-colour mapping is taken as the initial configuration. To obtain detailed information in the inverse mapping procedure, the spatial discretization of the geometrical model of the product has to be relatively fine due to the large deformations that are induced by the fountain effect.

To conclude, the modelling of the multi-component flows, in the test problems as well as in injection moulding, proved to be rather complete and thus predictions can be done succesfully regarding all aspects that are important in the daily practice of multi-component injection moulding.

## 7.2   Recommendations

During the investigations presented in this thesis, some limitations of the existing techniques/modelling has been met. Therefore some recommendations for future research can be given:

- For injection moulded products where the ratio of thickness to flowlength is large, more detailed information at flow splittings or at the front region could be obtained by using local 'perpendicular' 2D calculations in those regions. Instead of connecting the midplanes, then the small 2-D regions take care of those connections in the case of flow splittings. The analogous 2D fountain region can be thought to be attached to the flow front.

- For relatively small products with a ratio of thickness to flowlenth close to unity, a complete 3-D analysis is more appropriate. The melt flow

front advancement could be modelled by an polymer/air interface represented by a high (polymer) and low (air) viscosity material applying the fixed domain approach.

- A disadvantage of the existing $2\frac{1}{2}$D approach for the application to multi-component moulding is that no solidified layer can be formed at the edges of the product. This, of course, effects the material distribution. (It is believed that an improvement is possible without completely abandoning the $2\frac{1}{2}$D concept.)

- To simulate the filling of a mould using an accumulator, the piston driven flow problem and the filling simulation have to be coupled. The results of the piston driven flow problem, e.g. the label identity values at the outlet, then provide for the input for the particle tracking problem in the injection moulding simulation code.

- A visco-elastic analysis of the piston driven flow problem is strongly recommended for the polystryrene melt in order to check if visco-elasticity is the reason for the observed deviation between numerical and experimental results. Moreover, the deformations that occur during heating and subsequent cooling should be avoided or controlled and calculated.

- The effect of the correct approach at the flow splittings and abrupt changes of thicknesses should be incorporated in the calculations of the final properties of a product, since history dependent properties like temperature, density, visco-elastic stresses, orientation and conversion, require that the conservation of identity is satisfied.

- Using the label identity method as material markers, gas-assisted injection moulding can be modelled by specifying the second material as a (very) low viscosity material representing the (nitrogen) gas. Incorporation of inertia in the formulation should be desired due to the high gas/polymer interface velocity during filling.

- At present the VI$p$ code fails a correct coupling between runners and the mould cavity with respect to particle tracking.

- Finally, the results of the inverse mapping procedure should be validated with experiments. For that purpose a very flexible valve system for controlling the material flows has to be designed.

# Appendix A

# Fountain flow approximations

The incorporation of the residence time in the fountain flow requires that the velocity field in the front region is known. In this Appendix two different approaches are followed. In the first, the semi-analytical solution of Bhattacharji and Savic (1965) for the flow kinematics in the fountain region is employed. In the second approach, the 2D velocity field is calculated with the aid of the finite element calculations using the FEM package SEPRAN (Segal, 1984). In both approaches, the residence time and the exit position are determined as function of the entrance position in the front domain by tracking particles by integrating the velocity field using a Runga-Kutta integration technique. The results are parameterized by a high order polynomial function for future use in the injection mould filling simulations.

**Bhattacharji and Savic model**

The analytical solution of Bhattacharji and Savic (1965) is derived under assumption that:

- the fluid behaves Newtonian and is incompressible.

- the contact angle at the wall is 90° and the front is flat.

- there is no wall-slip except at the moving contact line.

- inertia terms can be neglected.

- conservation of momentum can be considered quasi-stationary.

The velocity components are given by (see e.g. Castro and Macosko, 1982):

$$v_x(x, z) = -\bar{v} \left( \frac{1}{2} - 6\frac{z^2}{h^2} \right) \left[ 1 - 1.45e^{-5\frac{x}{h}} \sin(0.76 + 2\frac{x}{h}) \right] +$$

$$- 0.53 \left( 1 - 80\frac{z^4}{h^4} \right) \left[ e^{-5\frac{x}{h}} \sin(2\frac{x}{h}) \right], \quad \text{(A.1)}$$

$$v_z(x, z) = \bar{v}\frac{z}{h} \left( 1 - 4\frac{z^2}{h^2} \right) \left[ 3.63e^{-5\frac{x}{h}} \sin(0.76 + 2\frac{x}{h}) \right.$$

$$\left. -1.45e^{-5\frac{x}{h}} \cos(0.76 + 2\frac{x}{h}) \right]$$

$$- 2\frac{z}{h} \left( 1 - 16\frac{z^4}{h^4} \right) \left[ 1.32e^{-5\frac{x}{h}} \sin(2\frac{x}{h}) - 0.53e^{-5\frac{x}{h}} \cos(2\frac{x}{h}) \right], \quad \text{(A.2)}$$

where $\bar{v}$ the average front velocity, $h$ the total gap thickness, and $x, z$ the coordinates in the flow and gapwise direction respectively.

The influence of the fountain flow is limited to region of length $h$ measured from the front line (cf. Mavridis *et al.*, 1986; Shen, 1992). In order to obtain the residence time and the exit position in the front region, the trajectories of those particles are computed which are initially positioned a distance of $h$ away from the front line. Particle paths are constructed until the particle re-enters the main flow. The relation between the exit position $z_o$ and the entrance position $z_i$ and residence time $t_r$ thus obtained are respectively fitted with the high order polynomials:

$$z_i^*(z_o^*) = \sum_{i=0}^{n_z} a_i z_o^{*i}, \qquad t_r^*(z_o) = \sum_{i=0}^{n_t} b_i z_o^{*i} \quad \text{(A.3)}$$

Coordinates are made dimensionless by $z_i^* = z_i/2h$ and $z_o^* = z_o/2h$ and the residence time by $t_r^* = (t_r\bar{v}/h$.

The results are shown in figure A.1 for both the computed data and the fit. The coefficients of the polynomial functions are listed in table A.1.

### Finite element simulations

The classical fountain flow differs from the piston driven flow in that the boundary conditions differ at the boundary $\Gamma_3$ (see figure 3.3). Instead of a no-slip condition, in this case a no-traction condition has to prescribed and a vanishing normal velocity:

$$\begin{aligned}(\sigma \cdot \vec{n}) \cdot \vec{n} &= 0 \quad \text{on } \Gamma_3 \\ (\sigma \cdot \vec{n}) \cdot \vec{t} &= 0 \quad \text{on } \Gamma_3 \end{aligned} \quad \text{(A.4)}$$

Figure A.1: Residence time $t_r$ (a) and inflow position $z_i$ (b) in front region as function of outflow position $z_o$ (Bhattacharji and Savic model)

| Bhattacharji and Savic model | | |
|---|---|---|
| i | a | b |
| 0 | 4.377 | 76324.9 |
| 1 | -25.336 | -576340.5 |
| 2 | 74.619 | 1810274.2 |
| 3 | -118.676 | -3025308.9 |
| 4 | 103.284 | 2836063.3 |
| 5 | -46.599 | -1413695.4 |
| 6 | 8.330 | 292695.3 |

Table A.1: Coefficients of the polynomials of the parameterized front model (Bhattacharji and Savic)

The shape of the free surface $\Gamma_3$ can also be varied between a straight line or a semi-circle to investigate the influence on the residence time in the front model. The FEM calculations are performed with a average (wall) velocity of $v_p = 1.6 \ m/s$ while the gap width $h$ equals 10 $mm$. A typical result of such calculation can be found in figure A.2. Clearly demonstrated is that the folding line shift towards the wall and that the residence time differs considerably from the Newtonian case. However, the flow kinematics for the generalized Newtonian case depends on too much variables, so parametrization is not possible anymore. Since the effect of the residence time on the distribution of the material particles is small (see Zoetelief, 1992) compared to the effect of the non-isothermal generalized Newtonian flow, a possible contribution is neglegted (see e.g. Zoetelief, 1992) in the calculations presented in this thesis.
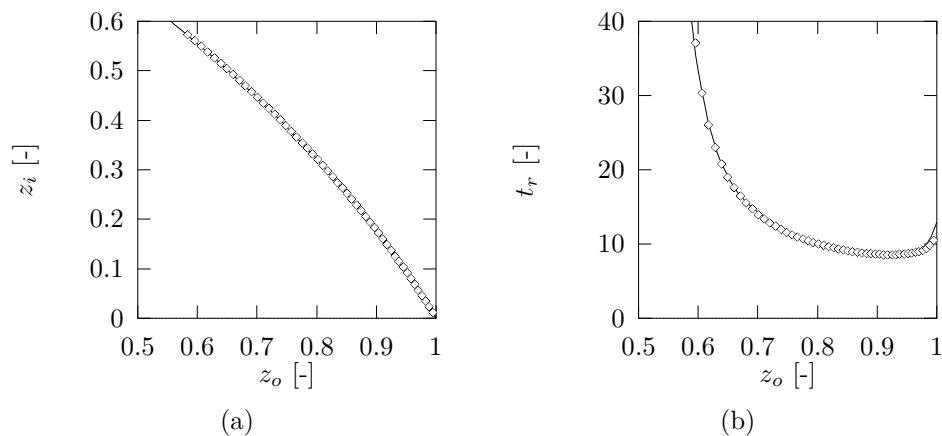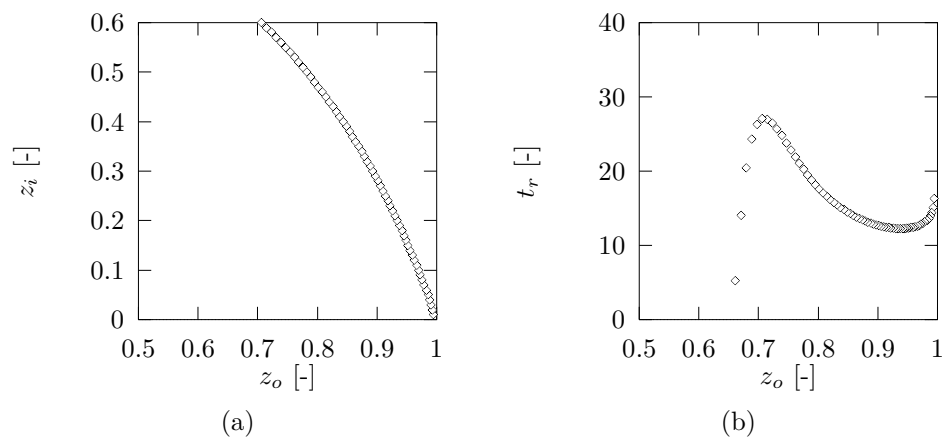
Figure A.2: Residence time $t_r$ (a) and inflow position $z_i$ (b) in front region as function of outflow position $z_o$ (FEM calculation with generalized Newtonian fluid behaviour

# Appendix B

# Solution methods for the convection equation

Both the particle tracking problem and the splitting technique of the convection operator in the determination of the different material derivatives as occuring in the balance equations result in the numerical solution of a hyperbolic scalar convection equation. During the past decade, several finite element methods has been developed for solving this type of equations. Amongst these methods, the Streamline Upwind Petrov Galerkin (SUPG) method is widely used.

The problem to be solved is stated as follows: *Given a velocity field $\vec{v}(\vec{x}, t)$, and initial value $\phi_0(\vec{x})$, find $\phi(\vec{x}, t)$, such that*

$$\frac{\partial \phi}{\partial t} + \vec{v} \cdot \vec{\nabla} \phi = 0, \tag{B.1}$$

$$\phi(\vec{x}, t) = \phi_0 \quad \text{in } \Omega, \tag{B.2}$$

$$\phi = \phi_d \quad \text{on } \Gamma_d \tag{B.3}$$

in which $\phi_d$ denote the Dirichlet boundary conditions. When applying the Galerkin approximation to equation B.1, the weak form of the convection equation reads:

$$\left(w, \frac{\partial \phi}{\partial t} + \vec{v} \cdot \vec{\nabla} \phi\right) = 0 \tag{B.4}$$

where $w$ is a suitable test function and $(.,.)$ the inner product. The standard Galerkin method suffers from spurious oscillations when used for solving the convection equation (Pé $\rightarrow \infty$). Analogous to finite difference methods, upwinding may improve the accuracy of the results. In the SUPG method, the test function $\tilde{w}$ consist of two parts according to

$$\tilde{w} = w + \alpha \vec{v} \cdot \vec{\nabla} w \tag{B.5}$$

in which $\alpha$ is the upwind paramater. With this test function the information upstream is weighted more heavily than downstream. The weak form is giving by

$$\left(w, \frac{\partial \phi}{\partial t} + \vec{v} \cdot \vec{\nabla}\vec{v}\right) + \left(\alpha \vec{v} \cdot \vec{\nabla}w, \frac{\partial \phi}{\partial t} + \vec{v} \cdot \vec{\nabla}\vec{v}\right) = 0, \tag{B.6}$$

where the second term represents the upwind correction.

For a pure convection equation, two possible choices of the upwind parameter $\alpha$ can be made:

The classical upwind scheme: $\quad \alpha = \dfrac{h}{2 \parallel \vec{v} \parallel}$ $\qquad$ (B.7)

A time dependent parameter: $\quad \alpha = \left(\left(\dfrac{2}{\Delta t}\right)^2 + \left(\dfrac{2 \parallel \vec{v} \parallel}{h}\right)^2\right)^{-1/2}$ $\quad$ (B.8)

where $h$ is the element size in the direction of the flow, $\parallel \vec{v} \parallel$ the magnitude of the velocity and $\Delta t$ the time step. The time dependent parameter is originally derived from the Galerkin Least Squares (GLS) method by Shahib for instationary problems (see e.g. Vreugdenhil and Koren, 1993, Chapter 8). Note that for pure convection equations, the GLS method reduces to SUPG in case of a time independent test function and, therefore, can be regarded as a SUPG method with a specific upwind parameter. Both choices are available in the finite element package SEPRAN Segal (1984) and their performance is tested for a model problem: the Molenkamp test.

In the Molenkamp test (Vreugdenhil and Koren, 1993), a 'cloud' of material is advected through the flow domain by a rotating velocity field. After one complete revolution the solution should coincide with the initial (and exact) solution. The velocity field is given by:

$$v_x = -2\pi y, \quad v_y = 2\pi x, \quad [x, y] \in [-1, 1] \times [-1, 1]. \tag{B.9}$$

The initial condition is a Gaussian distribution (see figure B.1a) represented by

$$\phi(x, y, 0) = 0.01^{4r^2}, \quad r = \sqrt{(x + \frac{1}{2})^2 + y^2}. \tag{B.10}$$

Dirichlet boundary conditions are prescribed at the inflow, where the exact solution is imposed:

$$\phi(x, y, t) = 0.01^{4r^2}, \quad r = \sqrt{(x + \frac{1}{2}\cos 2\pi t)^2 + (y + \frac{1}{2}\sin 2\pi t)^2}. \tag{B.11}$$

This problem has been solved on $10 \times 10$, $20 \times 20$ and $40 \times 40$ rectangular grids consisting of bilinear quadrilateral elements. In table B.1 the results of the SUPG method with the parameter $\alpha$ according to the classical scheme (CLAS) and the approximation of Shahib (SHA) can be compared. Also the effect of the time integration scheme chosen, Euler implicit (EU) or Crank Nicholson (CN), is revealed. Table B.1 shows the time steps used, the maximum $\phi_{max}$ and the minimum value $\phi_{min}$ of the solution, the error in the 1-norm and the error in the $\infty$-norm. The errors are defined as:

$$\| \Delta\phi \|_1 = \| \phi - \phi_{exact} \|_1 = \frac{1}{N} \sum_{i=1}^{N} |(\phi - \phi_{exact})_i| \tag{B.12}$$

$$\| \Delta\phi \|_\infty = \| \phi - \phi_{exact} \|_\infty = \max_{1 \leq i \leq N} |(\phi - \phi_{exact})_i| \tag{B.13}$$

Some typical result after one complete revolution are drawn in figure B.1b to d. From the results it can be concluded that the SUPG method with Shahib's approximation of the upwind parameter in combination with the Crank Nicholson time integration gives the best performance on a coarse grid. Therefore, this method is chosen for solving the convection problem in the simulations described in the Chapters 5 and 6.

| Method | grid | $\Delta t$ | $\phi_{max}$ | $\phi_{min}$ | $\| \Delta\phi \|_1$ | $\| \Delta\phi \|_\infty$ |
|---|---|---|---|---|---|---|
| CLAS/ | $10 \times 10$ | 0.01 | 0.394 | $-4.76 \cdot 10^{-2}$ | $2.68 \cdot 10^{-2}$ | $4.75 \cdot 10^{-1}$ |
| CN | $20 \times 20$ | 0.005 | 0.727 | $-1.76 \cdot 10^{-2}$ | $1.03 \cdot 10^{-2}$ | $2.73 \cdot 10^{-1}$ |
| | $40 \times 40$ | 0.002 | 0.934 | $-1.44 \cdot 10^{-3}$ | $2.01 \cdot 10^{-3}$ | $6.59 \cdot 10^{-2}$ |
| SHA/ | $10 \times 10$ | 0.01 | 0.556 | $-6.98 \cdot 10^{-2}$ | $2.30 \cdot 10^{-2}$ | $5.28 \cdot 10^{-2}$ |
| CN | $20 \times 20$ | 0.005 | 0.901 | $-1.13 \cdot 10^{-2}$ | $3.91 \cdot 10^{-3}$ | $9.94 \cdot 10^{-2}$ |
| | $40 \times 40$ | 0.002 | 0.991 | $-1.75 \cdot 10^{-6}$ | $3.78 \cdot 10^{-4}$ | $1.33 \cdot 10^{-2}$ |
| SHA/ | $10 \times 10$ | 0.01 | 0.450 | $-2.73 \cdot 10^{-4}$ | $2.71 \cdot 10^{-2}$ | $5.50 \cdot 10^{-1}$ |
| EU | $20 \times 20$ | 0.005 | 0.580 | $-1.97 \cdot 10^{-4}$ | $1.89 \cdot 10^{-2}$ | $4.20 \cdot 10^{-1}$ |
| | $40 \times 40$ | 0.002 | 0.760 | $-2.02 \cdot 10^{-5}$ | $1.07 \cdot 10^{-2}$ | $2.45 \cdot 10^{-1}$ |

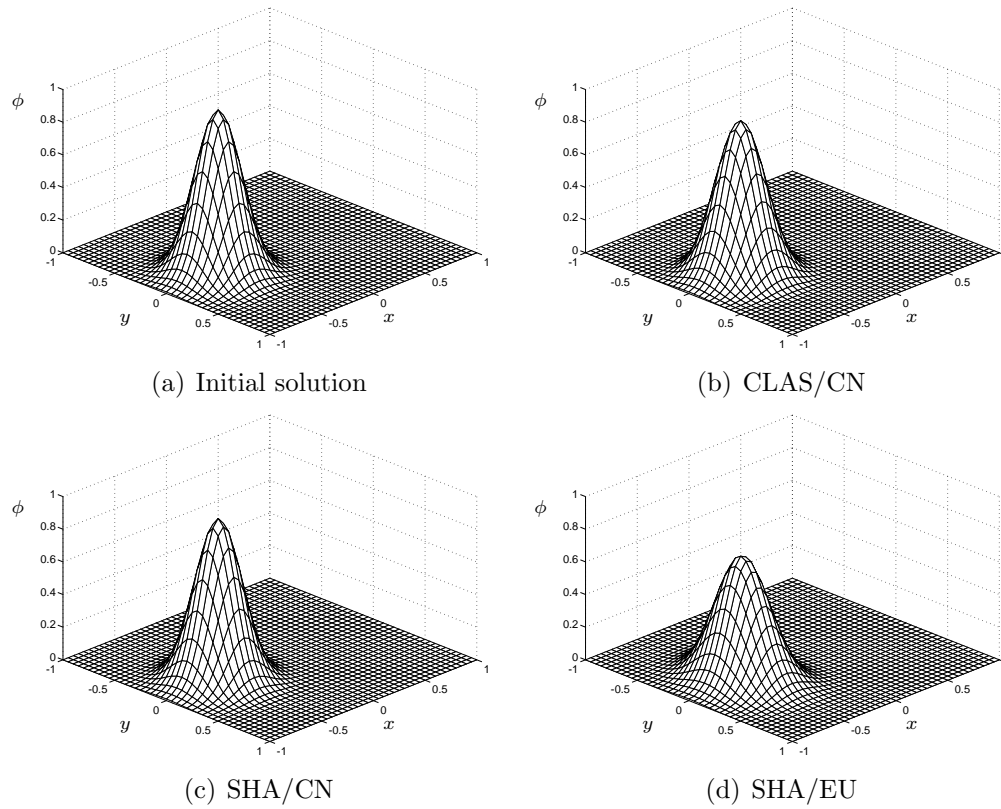Table B.1: Numerical results Molenkamp test for various grids and various methods

(a) Initial solution

(b) CLAS/CN

(c) SHA/CN

(d) SHA/EU

Figure B.1: Initial and final solutions after one complete revolution (Molenkamp test $40 \times 40$ grid)

# Bibliography

Akkerman, R. (1993). *Euler-Lagrange Simulations of Non-isothermal Viscoelastic Flows*. Ph.D. thesis, University of Twente.

Baaijens, F. P. T. (1991). Calculation of residual stresses in injection moulded products. *Rheol. Acta*, **30**, 284–299.

Baaijens, F. P. T. (1992). *Applied Computational Mechanics 2, lecture notes*. Eindhoven University of Technology, The Netherlands.

Behrens, R. A., Crochet, M. J., Denson, C. D., and Metzner, A. B. (1987). Transient free-surface flows: motion of a fluid advancing in a tube. *AIChE. J.*, **33**, 1178–1168.

Beris, A. N. (1987). Fluid elements deformation behind an advancing flow front. *J. Rheol.*, **31**, 121–124.

Bhattacharji, S. and Savic, P. (1965). Real and apparent non-Newtonian behaviour in viscous pipe flow of suspensions driven by a fluid piston. In A. F. Charwat, editor, *Proc. 1965 Heat Transf. Fluid Mech. Inst.*, pages 248–262. Stanford University Press.

Boshouwers, A. H. M. and van der Werf, J. J. (1988). *Inject-3, A Simulation Code for the Filling Stage of the Injection Moulding Process of Thermoplastics*. Ph.D. thesis, Eindhoven University of Technology.

Brooks, A. N. and Hughes, T. J. R. (1982). Streamline upwind/Petrov-Galerkin formulations for convection dominated flows with particular emphasis on the incompressible Navier-Stokes equations. *Comp. Meth. in App. Mech. and Eng.*, **32**, 199–259.

Caspers, L. W. (1991). *Calculation of Trajectories in the Numerical Simulation of the Injection Moulding Process*. Master's thesis, Eindhoven University of Technology. (in Dutch).

Caspers, L. W. (1995). *VI*p*, an integral approach to the simulation of injection moulding: prediction of product properties*. Ph.D. thesis, Eindhoven University of Technology. to appear.

Caspers, L. W., Douven, L. F. A., van de Vosse, F. N., and Zoetelief, W. F. (1994). Vi*p*, manual. Technical report, Eindhoven University of Technology.

Castro, J. M. and Macosko, C. W. (1982). Studies of moldfilling and curing in the reaction injection molding process. *AIChE. J.*, **28**, 250–260.

Chiang, H. H., Hieber, C. A., and Wang, K. K. (1991a). A unified simulation of the filling and postfilling stages in injection molding. part I : Formulation. *Pol. Eng. and Sc.*, **31**, 116–124.

Chiang, H. H., Hieber, C. A., and Wang, K. K. (1991b). A unified simulation of the filling and postfilling stages in injection molding. part II : Experimental verification. *Pol. Eng. and Sc.*, **31**, 125–139.

Couniot, A., Dheur, L., and Dupret, F. (1993). Numerical simulation of injection molding: Non-isothermal filling of complex thin parts, including abrupt changes of thickness or bifurcations of the midsurface. In M. Cross, J. F. T. Pittman, and R. D. Wood, editors, *Proc. of the IMA Conference on Mathematical Modelling for Materials Processing 1991*, pages 381–398. Oxford University Press.

Coyle, D. J., Blake, J. W., and Macosko, C. W. (1987). The kinematics of fountain flow in mold-filling. *AIChE. J.*, **33**, 1168–1177.

Crochet, M. J., Davies, A. R., and Walters, K. (1984). *Numerical Simulation of Non-Newtonian Flow*. Elsevier, Amsterdam.

Cuvelier, C., Segal, A., and van Steenhoven, A. A. (1986). *Finite Element Methods and Navier-Stokes Equations*. D. Reidel Publishing Company, Dordrecht.

Ding, D., Townsend, P., and Webster, M. F. (1990). Numerical simulation of filling problems related to injection moulding. In *Proc. of IUTAM Symposium on Numerical Simulation of Nonisothermal Flow of Viscoelastic Liquids*. in press.

Donea, J. (1991). Generalized galerkin methods for convection dominated transport phenomena. *App. Mech. Rev.*, **44**, 205–214.

Donovan, R. C., Rabe, K. S., Mammel, W. K., and Lord, H. A. (1975). Recycling plastics by two-shot molding. *Pol. Eng. Sci.*, **15**, 774–780.

Douven, L. F. A. (1991). *Towards the Computation of Properties of Injection Moulded Products: Flow- and Thermally Induced Stresses in Amorphous Thermoplastics*. Ph.D. thesis, Eindhoven University of Technology.

Dupret, F. and Vanderschuren, L. (1988). Calculation of the temperature field in injection molding. *AIChE. J.*, **34**, 1959–1972.

Eckardt, H. (1985). Mehrkomponenten-spritzgießen ermöglicht das herstellen abgeschirmter gehäuse mit guter oberfläche in einen arbeitsgang. *Kunststoffe*, **75**, 145–152.

Eckardt, H. (1987). Co-injection charting new territory and opening new markets. *J. of Cellular Plastics*, **23**, 555–592.

Evans, I. A. (1992). Letter to the editor: On the nature of yield stress. *J. Rheol.*, **36**, 1313–1318.

Ferry, J. D. (1980). *Viscoelastic Properties of Polymers*. John Wiley & Sons, New York, third edition.

Flaman, A. A. M. (1990). *Build-up and Relaxation of Molecular Orientation in Injection Moulding*. Ph.D. thesis, Eindhoven University of Technology.

Friedrichs, B. and Güçeri, S. I. (1993). A novel hybrid numerical technique to model 3d fountain flow in injection molding processes. *J. Non-Newtonian Fluid Mech.*, **49**, 141–173.

Garcia, M., Macosko, C., Subbiah, S., and Güçeri, S. (1991). Modeling of reactive filling in complex cavities: Comparison of fountain flow approximations. *Int. Pol. Proc.*, **6**, 73–82.

Garner, P. J. and Oxley, D. F. (1969). British patent No.1, 156, p.217, Assigned to ICI.

Gogos, C. G., Huang, C., and Schmidt, L. R. (1986). The process of cavity filling including the fountain flow in injection molding. *Pol. Eng. Sci.*, **26**, 1457–1466.

Greener, J. (1986a). General consequences of the packing phase in injection molding. *Pol. Eng. and Sc.*, **26**, 886–892.

Greener, J. (1986b). Pressure-induced densification in injection molding. *Pol. Eng. and Sc.*, **26**, 534–542.

Haiqing, G. (1993). A procedure for characterising the fountain effect in the filling of a complex mold. *J. Mat. Proc. Techn.*, **38**, 41–50.

Hannachi, A. and Mitsoulis, E. (1990). Deformation fields and residence time distributions in polymer melt flows. *Int. Pol. Proc.*, **5**, 244–251.

Harry, D. H. and Parrot, R. G. (1970). Numerical simulation of injection mold filling. *Pol. Eng. and Sc.*, **10**, 209–214.

Hendriks, R. D. H. M. (1992). Evaluation of the co-injection moulding simulation program inject-3c (part 2). Technical Report CTB541-92-5035, Philips Centre for Manufacturing Technology, Eindhoven.

Hieber, C. A. (1987). Melt-viscosity characterization and its application to injection molding. In A. I. Isayev, editor, *Injection and Compression Molding Fundamentals*, chapter 1. Marcel Dekker, Inc.

Hieber, C. A. and Shen, S. F. (1980). A finite-element/finite-difference simulation of the injection-molding filling process. *J. Non-Newtonian. Fluid Mech.*, **7**, 1–32.

Hieber, C. A., Socha, L. S., Shen, S. F., Wang, K. K., and Isayev, A. I. (1983). Filling thin cavities of variable gap thickness: A numerical and experimental investigation. *Pol. Eng. and Sc.*, **23**, 20–26.

Hirsch, C. (1990). *Numerical Computation of Internal and External Flows*, volume 1&2. John Wiley and Sons, Chicester.

Isayev, A. I., editor (1987). *Injection and Compression Molding Fundamentals*. Marcel Dekker, Inc.

Isayev, A. I. and Hariharan, T. (1985). Volumetric effects in the injection molding of polymers. *Pol. Eng. and Sc.*, **25**, 271–278.

Isayev, A. I. and Hieber, C. A. (1980). Toward a viscoelastic modelling of the injection molding of polymers. *Rheol. Acta*, **19**, 168–182.

Kamal, M. R. and Lafleur, P. G. (1982). Computer simulation of injection molding. *Pol. Eng. and Sc.*, **22**, 1066–1074.

Kamal, M. R. and Papathanasiou, T. D. (1993). Filling of a complex-shaped mold with a viscoelastic polymer. part ii: Comparison with experimental data. *Pol. Eng. and Sc.*, **33**, 410–417.

Kamal, M. R., Chu, E., Lafleur, P. G., and Ryan, M. (1986). Computer simulation of injection mold filling for viscoelastic melts with fountain flow. *Pol. Eng. and Sc.*, **26**, 190–196.

Lafleur, P. G. and Kamal, M. R. (1986). A structure-oriented computer simulation of the injection molding of viscoelastic crystalline polymers. part I: Model with fountain flow, packing, solidification. *Pol. Eng. and Sc.*, **26**, 92–102.

Lord, H. A. and Williams, G. (1975). Mold-filling studies for the injection molding of thermoplastic materials. part II: The transient flow of plastic materials in the cavities of injection-molding dies. *Pol. Eng. and Sc.*, **17**, 568–582.

Luo, X.-L. and Mitsoulis, E. (1990). An efficient algorithm for strain history tracking in finite element computations of non-Newtonian fluids with integral constitutive equations. *Int. J. Num. Meth. in Fluids*, **11**, 1015–1031.

Luo, X.-L. and Tanner, R. I. (1986). A streamline element scheme for solving viscoelastic flow problems. part ii: Integral constitutive models. *J. Non-Newt. Fluid Mech.*, **22**, 61–89.

Manas-Zloczower, I., Blake, J. W., and Macosko, C. W. (1987). Space-time distribution in filling a mold. *Pol. Eng. Sci.*, **27**, 1229–1235.

Matsuhiro, I. and Shiojima, T. (1990). Numerical analysis of polymer injection moulding process using finite element method with marker particles. *Int. J. Num. Meth. in Eng.*, **30**, 1569–1576.

Mavridis, H., Hrymak, A. N., and Vlachopoulos, J. (1986). Finite element simulation of fountain flow in injection molding. *Pol. Eng. and Sc.*, **26**, 449–454.

Mavridis, H., Hrymak, A. N., and Vlachopoulos, J. (1987). Finite-element simulation of stratified multiphase flows. *AIChE. J.*, **33**, 410–422.

Mavridis, H., Hrymak, A. N., and Vlachopoulos, J. (1988). The effect of fountain flow on molecular orientation in injection molding. *J. of Rheol.*, **32**, 639–663.

Müller, I. (1984). *Thermodynamics*. Pitman, London.

Münstedt, H. (1981). Rheology of rubber-modified polymer melts. *Pol. Eng. Sci.*, **21**, 259–270.

Oosterling, W. J. A. (1994). *Numerical simulation of a viscous flow in a time dependent domain*. Master's thesis, Eindhoven University of Technology, The Netherlands.

Papathanasiou, T. D. and Kamal, M. R. (1993). Filling of a complex-shaped mold with a viscoelastic polymer. part i: The mathematical model. *Pol. Eng. and Sc.*, **33**, 400–409.

Peters, G. W. M. (1989). Modeling of the injection moulding of reactive materials. Technical Report WFW 89050, Eindhoven University of Technology.

Peters, G. W. M., Spoelstra, A. B., Meuwissen, M. H. H., Corbey, R., and Meijer, H. E. H. (1993). Rheology and rheometry for highly filled reactive materials. In J. Dijksman and F. Nieuwstadt, editors, *Topics in Applied Mechanics*, pages 331–338. Kluwer Academic Publishers.

Peters, G. W. M., van der Velden, P. J. L., Meijer, H. E. H., and Schoone, P. (1994). Multilayer injection moulding. part 2: Particle tracking in reactive moulding. *Int. Pol. Proc.*, **9**, 258–265.

Richardson, S. M., Pearson, H. J., and Pearson, J. R. A. (1980). Simulation of injection moulding. *Plast. Rubber Process Appl.*, **5**, 55–65.

Rose, W. (1961). Fluid-fluid interfaces in steady motion. *Nature*, **191**, 242–243.

Schmidt, L. R. (1974). A special mold and tracer technique for studying shear and extensional flows in a mold cavity during injection molding. *Pol. Eng. Sci.*, **14**, 797–800.

Segal, A. (1984). *SEPRAN, user manual, standard problems and programming guide*. Ingenieursbureau SEPRA, Leidschendam, The Netherlands.

Shen, S. F. (1992). Grapplings with the simulation of non-newtonian flows in polymer processing. *Int. J. for Num. Meth. in Eng.*, **34**, 701–723.

Sitters, C. W. M. (1988). *Numerical Simulation of Injection Moulding*. Ph.D. thesis, Eindhoven University of Technology.

St. Jacques, M. (1982). An analysis of thermal warpage in injection molded flat parts due to unbalanced cooling. *Pol. Eng. and Sc.*, **22**, 241–247.

Thompson, E. (1986). Use of pseudo-concentration to follow creeping viscous flows during transient analysis. *Int. J. Num. Meth. in Fluids*, **6**, 749–761.

Titomanlio, G., Ducrato, V., and Kamal, M. R. (1987). Mechanism of cooling stress build-up in injection molding of thermoplastic polymers. *Int. Polymer Processing*, **1**, 55–59.

Tucker III, C. L. (1991). *Fundamentals of Computer Modeling for Polymer Processing*. Hanser Publishers, Munich.

Tung, T. T. and Kudert, F. G. (1990). An injection molding process for producing encapsulated multilayer articles. In *Proceedings Annual Meeting Soc. Plast. Eng. ANTEC '90*, pages 760–762.

Turng, L. S., Wang, V. W., and Wang, K. K. (1993). Numerical simulation of co-injection molding filling process. *J. of Eng. Mat. and Techn.*, **115**, 48–53.

van de Vosse, F. N. (1987). *Numerical Analysis of Carotid Artery Flow*. Ph.D. thesis, Eindhoven University of Technology.

Verheijen, J., Kersemakers, J., and Meijer, H. E. H. (1983). Private communication.

Vos, E., Meijer, H. E. H., and Peters, G. W. M. (1991). Multilayer injection molding. *Int. Pol. Proc.*, **6**, 42–50.

Vreugdenhil, C. B. and Koren, B., editors (1993). *Numerical methods for advection-diffusion problems*, volume 45 of *Notes on numerical fluid mechanics*. Vieweg, Braunschweig, Germany.

White, J. J. and Lee, B. L. (1975). An eperimental study of sandwich injection molding of two polymer melts using simultaneous injection. *Pol. Eng. Sci.*, **15**, 481–485.

Williams, G. and Lord, H. A. (1975). Mold-filling studies for the injection molding of thermoplastic materials. part I: The flow of plastic materials in hot- and cold-walled circular channels. *Pol. Eng. and Sc.*, **17**, 553–568.

Wu, P. C., Huang, C. F., and Gogos, C. G. (1974). Simulation of the mold-filling process. *Pol. Eng. and Sc.*, **14**, 223–230.

Xie, G., Peters, G. W. M., van de Vosse, F. N., and Meijer, H. E. H. (1991). On the analysis of multi-component incompressible newtonian flows. In *Numerical methods in laminar and turbulent flow, Proc. of the 7th Int. Conf., Stanford*, pages 12–21.

Young, S. S., White, J. J., Clark, E. S., and Oyanagi, Y. (1980). A basic eperimental study of sandwich injection molding with sequential injection. *Pol. Eng. Sci.*, **20**, 798–804.

Zoetelief, W. F. (1992). On the numerical simulation of the multilayer injection moulding process. Technical Report WFW 92.100, Institute for Continuing Education, Eindhoven University of Eindhoven.

Zoller, P. (1982). A study of the pressure-volume-temperature relations of four related amorphous polymers: polycarbonate, polyarylate, phenoxy, and polysulfone. *J. Pol. Sci.*, **20**, 1453–1464.

# Samenvatting

In het meer-komponenten-spuitgietproces kunnen twee of drie polymere materialen na elkaar of gelijktijdig in een matrijs worden geïnjekteerd teneinde produkten te maken die bijvoorbeeld een specifieke gelaagde struktuur bevatten. De verdeling van de materialen in het produkt hangt af van de positie van de aanspuiting, de geometrie van de spuitneus en de methode van injekteren (simultaan of sequentieel). Toepassingen van deze techniek kunnen gevonden worden in elektromagnetische afscherming, produkten met een barrière laag, herverwerking van thermoplasten, en in het 'in-mould' lakken van produkten en tenslotte zelfs in produkten die inwendige scharnieren bevatten door twee niet mengbare materialen op de juiste manier te injekteren.

Het grote voordeel van spuitgieten is de grote veelzijdigheid in ontwerp waardoor een hoge mate van integratie bereikt kan worden. Dit kan worden uitgebreid met de mogelijkheid tot het combineren van verschillende materialen, met elk zijn specifieke eigenschappen, in één produkt. Teneinde dat doel te bereiken, zullen eerst enige beperkingen van de huidige stand van techniek moeten worden overwonnen. Ten eerste zal het aantal materialen van twee op drie gebracht moeten worden om de combinatie van polaire met apolaire materialen in een produkt mogelijk te maken. Het derde materiaal fungeert dan als hechtverbeteraar. Ten tweede zou het produktontwerp niet beperkt mogen worden door de gebruikte fabricagemethode. Beide punten vereisen de beschikbaarheid van een model om de materiaal verdeling in een produkt te voorspellen. In dit proefschrift worden numerieke gereedschappen ontwikkeld waarmee de plaats van materiële deeltjes tijdens de stroming in de matrijsholte berekend kan worden. Uitgaande van een vereiste materiaalverdeling in een produkt, zal uiteindelijk het inverse probleem opgelost moeten worden om de bijbehorende injektie configuratie en/of machine programmering te voorspellen.

Uitgaande van de balansvergelijkingen voor massa, impuls, impulmoment en energie kunnen de basisvergelijkingen afgeleid worden die het uitgangspunt vormen voor de verdere afleidingen. Deze set vergelijkingen zijn sterk vereenvoudigd door gebruik te maken van het feit dat een matrijsholte bestaat

uit dunne, zwak gekromde kanalen. Aldus ontstaat de smeerfilm of $2\frac{1}{2}$D benadering. Om dit stelsel te kunnen oplossen zijn constitutieve relaties nodig. Gekozen is voor een egeneraliseerd Newton's model voor het vloeige-drag en de Tait-vergelijking voor de druk- en temperatuurafhankelijkheid van de dichtheid. Voor het volgen van materiele deeltjes is een methode, gebaseerd op het behoud van identiteit van die deeltjes, aan de set vergelijkingen toegevoegd. De identiteit van een deeltje is uniek en wordt gedefinieerd door zijn intree positie en injektietijd. Tijdens de stroming in de matrijs verandert die identiteit niet. Verder is in de modellering de aandacht gericht op het voldoen van (lokaal) massabehoud in het frontgebied en in die gebieden waar de stroming zich splitst.

De modellering is getest door het vergelijken van numerieke en experimentele resultaten voor twee goed gedefinieerde stromingsproblemen: de stroming tussen twee synchroon bewegende zuigers in een cilinder met en zonder de aanwezigheid van een restrictie. Door gebruik te maken van ge-kleurde schijfjes van gelijke of verschillende materialen gecombineerd in één proefstuk, kunnen de deformatiepatronen zichtbaar gemaakt worden. De op deze wijze ontstane patronen blijken gevoelig te zijn voor alle aspekten die de kinematica van de stroming kunnen beïnvloeden. Verschillen in het vloeigedrag tussen polystyreen (PS) en acrylonitryl-butadieen-styreen (ABS) worden bijvoorbeeld duidelijk zichtbaar. De stroming door de restrictie is gemodelleerd met behulp van een 'fixed domain' benadering. De zuigers worden daarin voorgesteld door een materiaal met een kunstmatig hoge vis-cositeit dat slipt aan de wand. Dit speciale geval van een meerkomponenten-stroming geeft een goede benadering van een stroming in een tijdsafhankelijk domein.

Verschillende toepassingen van het meer-komponenten-spuitgietproces worden toegelicht. De kleurverdeling in een strip, die door middel van co-injektie is gemaakt, is berekend en vergeleken met experimentele resultaten. Het kleurenpatroon in het middenvlak en aan het oppervlak, veroorzaakt door doorbraak van het als tweede geïnjekteerde materiaal door het eerste, laat zien dat alle aspecten aanwezig in de experimenten terug te vinden zijn in de berekende resultaten. Het effect van een splitsing van de stroming is onderzocht door middel van een numeriek experiment. Tenslotte zijn er twee voorbeelden gegeven van de inverse transformatie. In het eerste voor-beeld wordt een relatief complex produkt gevuld met twee componenten van hetzelfde materiaal maar van een andere kleur. Een iteratieve techniek is toegepast in het geval het een echte meer-komponenten-stroming van ver-schillende materialen betreft.

Concluderend kan gesteld worden dat computersimulaties onontbeerlijk zijn teneinde de vereiste materiaalverdeling in het produkt te bewerkstelligen.

Bovendien blijkt dat de modellering van de meer-komponenten-stroming, zowel in de testproblemen als in het spuitgieten, redelijk compleet is zodat met succes voorspellingen gedaan kunnen worden betreffende alle aspecten die van belang zijn in de dagelijkse praktijk.

# Curriculum Vitae

Wim Zoetelief

- 1-5-1966: Born in Baarn, The Netherlands.

- 1978-1984: R.S.G. Jan Hendrik Tromp Meesters Scholengemeenschap, Steenwijk (grammar school).

- 1984-1990: University of Twente, Masters degree at the Department of Mechanical Engineering.

- 1990-1995: Eindhoven University of Technology, Research assistant at the Department of Mechanical Engineering, section Engineering Fundamentals.

# Acknowledgements

I like to thank everyone who support me during the research and writing of this thesis. The co-members of the VI$p$-team, Frans van de Vosse, Lucien Douven and Leo Caspers, I owe special thanks, since without them this thesis was never accomplished. Furthermore, I thank Sjef Garenfeld and Alfred ter Stege (Arburg Nederland) for their part of the work involved in building the three-component injection moulding machine. The assistance of Jo Palmen (DSM Research) and Paul Tas during measuring the rheological properties is gratefully acknowledged. Remains the (former) graduate students, Marcel Schouenberg, Hans de Jonge, Lucien Kleintjens and Wim Oosterling, who participated in parts of the project.

# Stellingen

# Multi-component Injection Moulding

1. Indien het behoud van identiteit van materiële deeltjes geen wezenlijk onderdeel is van de modellering van het spuitgietproces, dan mag worden verondersteld dat voorspellingen van produkteigenschappen niet erg betrouwbaar zullen zijn. De invloed van asymmetrische temperatuurverdelingen, ontstaan door splitsing van materiaalstromen bij vertakkingen, op krimp en kromtrekken is hiervan een goed voorbeeld.

   - Dit proefschrift, Hoofdstukken 2 en 6.

2. Identificatie van materiaalmodellen voor de beschrijving van het deformatiegedrag van visco-elastische materialen kan worden uitgevoerd met behulp van complexe stromingen waarvan de begincondities en randvoorwaarden goed bekend zijn. De stroming tussen twee synchroon bewegende plunjers voldoet aan deze eisen.

   - J.P.W. Baaijens, *Evaluation of Constitutive Equations for Polymer Melts and Solutions in Complex Flows*, PhD thesis, Eindhoven University of Technology, The Netherlands (1994).
   - Dit proefschrift, Hoofdstuk 5.

3. Voor het verkrijgen van inzicht in het complexe stromingsgedrag in bijvoorbeeld een spuitgietproces is het gebruik in de modellering van gepulseerde injectie van een zich door een andere kleur onderscheidend materiaal te verkiezen boven de standaard continue regenboogkleuren die 'postprocessors' normaal leveren bijvoorbeeld voor de verblijftijdsverdeling. Het inzicht kan verder worden verhoogd door via een interactief proces de invloed van een wijziging in de injectieconfiguratie te bestuderen.

4. In het co-injectie proces wordt de doorbraak van het als tweede geïnjecteerde materiaal door het als eerste geïnjecteerde materiaal niet alleen bepaald door lokale effecten die optreden aan het vloeifront – de zogenaamde fonteinstroming – maar tevens door de gehele afkoelgeschiedenis tijdens de injectiefase van het produkt.

   - Dit proefschrift, Hoofdstukken 2 en 6.

5. Ondanks de twijfel aan het bestaan van een zwichtspanning in polymere materialen, blijkt dat de deformaties in de plunjerstroming voor acrylonitryl-butadieen-styreen (ABS) een zodanig patroon laten zien dat dit alleen door incorporatie van zo'n zwichtspanning in de modellering berekend kan worden.

   - I.D. Evans, On the nature of the yield stress, *J. Rheol.*, **36**, p. 1313-1321 (1992).
   - Dit proefschrift, Hoofdstukken 4 en 5.

6. Het uit commercieel oogpunt niet vermelden van essentiële details in een publikatie in een wetenschappelijk tijdschrift, getuigt niet van een wetenschappelijke attidude.

   - M. Baumgärtel and H.H. Winter, Determination of discrete relaxation and retardation time spectra from dynamic mechanical data, *Rheol. Acta*, **28**, p. 511-519 (1989).

7. De wegbeheerders in Nederland hebben een uitstekend gevoel voor de ideale lijn. Zij zorgen ervoor dat juist dáár de wegmarkeringen en putdeksels een plaats krijgen, hetgeen de risico's van het motorrijden tijdens slecht weer aanzienlijk doet stijgen.

8. Het Nederlandse belastingstelsel wordt continu zodanig vereenvoudigd dat het aantal belastingadviseurs alleen maar toeneemt.

9. Het bestaan van 'haute cuisine' katte- en hondevoer staat in schril contrast met het gebrek aan voedsel in de Derde Wereld landen.

10. Echte motorfietsen zijn rood.

Eindhoven, maart 1995                                          Wim Zoetelief